

Cascaded H-Bridge Multilevel Converter Topology for Hybrid Photovoltaic-Wind Turbine Systems

An der Naturwissenschaftlich-Technischen Fakultät
der Universität Siegen

zur Erlangung des akademischen Grades

Doktor der Ingenieurwissenschaften

(Dr.-Ing.)

genehmigte Dissertation

von

M.Sc. Eng. Othman Abdulhadi Taha

aus Mosul – Irak

Referent: Prof. Dr. –Ing. Mario Pacas

Korreferent: Prof. Dr. –Ing. Mustafa Kizilcay

Tag der mündlichen Prüfung: **14.12.2016**

Acknowledgment

This work has been carried out thanks to the financial support of the German Academic Exchange Service (Deutsche Akademische Austauschdienst - DAAD) and the Iraqi scholarship and cultural relations directorate.

I wish to express my deep gratitude to my advisor Prof. Dr. -Ing. Mario Pacas for his extraordinary support, knowledgeable advice and encouragement throughout the development of this difficult project. In addition I would like to thank the co-examiner Prof. Dr.-Ing. Mustafa Kizilcay for his valuable remarks and remarkable comments, which helped me improve the direction of this thesis dramatically.

I would also like to thank Prof. Dr.-Ing. Hubert Roth and Prof. Dr. rer. nat. Frank Gronwald for assuming guidance of the doctoral procedure.

I would like to thank the technical staff Dipl.-Ing. Erhard Oerter and Dipl.-Ing. Hans Walter Bruch for their technical support in the laboratory work and also special thanks to Mrs. Sabine Leukel for her administrative assistance.

This project would have been impossible without the support of my colleagues and friends Dr.-Ing. Simon Feuersänger and Dr.-Ing. The Minh Phan. I would also like to thank to all my other colleagues for their wisdom, support in the development of this project and for their friendship.

I would like to thank my family especially my great Father and my affectionate Mother who always encouraged me to go through the path of science and knowledge.

Finally, I am particularly thankful to my wife Seemaa who stood with me like a towering mountain throughout the march during the doctoral studies.

Abstract

In recent years, the energy generation with regenerative sources such as wind energy, photovoltaic, etc. has increased rapidly. The connection of such energy sources to the grid requires power electronics conversion systems. In the present work a new approach for the hybrid connection of solar panels and wind turbines is proposed. The system examined in the research work utilizes a 5-Level Cascaded H-bridge Voltage Source Inverter (5L-CHB-VSI) for this purpose and features advantages regarding the cost, the maintenance, and, especially, the availability of energy generation under changing weather conditions. The flexibility of the hybrid system allows different modes of operation depending on the available PV or wind power, which are considered in all details in the frame of the work. It is expected to be a good solution for the grid integration of small generation systems in rural or remote areas in developing countries.

Each phase of the 5L-CHB-VSI consists of two single-phase H-bridges, fed by separate DC-links. Therefore, a hybrid operation is possible by feeding the DC-links out of different energy sources. In the examined case the bridges are connected either to a photovoltaic (PV) string or to a rectifier, fed by an electrical generator that is driven by a wind turbine (WT). The grid connection was performed by using a voltage oriented control scheme with additional feedforward modulation index compensation (FFMIC). The proposed scheme controls the active and reactive power in the point of connection.

Two types of the feedforward compensation methods are presented, aiming at two targets. The first one, which is based on the injection of a zero-sequence signal, leads to balanced transfer of the power to the grid in case of unsymmetrical energy production among phases, due to fault degradation, model mismatch, partial shading at the PV string or weather conditions. The second one deals with the maximum power point tracking for each connected energy source without using the additional DC-DC converters that are necessary in conventional approaches.

The proposed control scheme - including feedforward modulation index compensation - was realized by using a single DSP. Furthermore, phase-shifted Pulse Width Modulation (PS-PWM) as well as Space Phasor Modulation (SPM) techniques were implemented to control the inverter. Experimental results on a laboratory setup confirm the theoretical considerations. The PV panels were emulated in the laboratory by using programmable DC supplies, while the wind turbines were emulated using permanent magnet synchronous generators. The results show the flexible operation of the system due to the individual MPPT operation for each H-bridge cell and the balanced injection of the power, even under unsymmetrical generation conditions. The possibility to switch between star- and delta-configuration of the inverter topology was proposed and analyzed in order to enhance the performance of the grid integration and the efficiency of conversion.

Zusammenfassung

Die Energieerzeugung aus regenerativen Quellen wie Windenergie, Photovoltaik usw. hat in den letzten Jahren eine enorme Bedeutung gewonnen. Der Anschluss von dezentralen Energieerzeugungssystemen aus regenerativen Energiequellen an das öffentliche Netz ist jedoch nicht möglich ohne geeignete, leistungselektronische Umwandlungssysteme. In der vorliegenden Arbeit wird dieses Thema in Angriff genommen und ein neuer Ansatz für den hybriden Anschluss von Photovoltaik- und Windenergieanlagen über einen einzelnen Umrichter vorgeschlagen. Das in den Forschungsarbeiten untersuchte System nutzt dazu einen Mehrstufen-Wechselrichter mit in Reihe geschalteten H-Brücken (5L-CHB-VSI) und bietet Vorteile bei Kosten, Wartung und insbesondere bei der Verfügbarkeit der Energieerzeugung unter wechselnden Witterungsbedingungen. Die Flexibilität des Hybridsystems ermöglicht, je nach Verfügbarkeit der PV- oder Windenergie, verschiedene Betriebsarten, die im Rahmen der Arbeit in allen Details berücksichtigt werden. Das vorgeschlagene und untersuchte System stellt eine gute Lösung für die Netzintegration von kleinen Erzeugungssystemen, in ländlichen oder abgelegenen Gebieten in Entwicklungsländern, dar.

Jede Phase des 5L-CHB-VSI besteht aus zwei in Reihe geschalteten einphasigen H-Brücken, die über getrennte DC-Zwischenkreise gespeist werden. Daher ist ein Hybridbetrieb möglich, indem die Gleichspannungseingänge aus verschiedenen Energiequellen gespeist werden. Im betrachteten Fall sind die H-Brücken entweder mit einem PV-String oder einem Gleichrichter verbunden, der von einem an einer Windturbine gekoppelten Generator gespeist wird. Die Netzanbindung wurde unter Verwendung einer spannungsorientierten Regelung mit einer zusätzlichen Vorsteuerung durchgeführt. Das vorgeschlagene Verfahren kann die Wirk- und die Blindleistung am Anschlusspunkt getrennt regeln.

Es werden zwei Arten der Vorsteuerungen mit unterschiedlichen Zielen vorgestellt. Die erste basiert auf der Addition eines Nullspannungssystems und symmetriert die eingespeisten Ströme im Fall einer unsymmetrischen Spannungserzeugung, die z. B.

durch Modellfehlpassung, partielle Verschattung an der PV, wechselnde Wetterbedingungen entstehen kann. Die zweite befasst sich mit der Umverteilung der generierten Leistung zwischen den einzelnen Zellen einer Phase. Diese Vorsteuerung wird durch die Einstellung des Betriebspunktes mit der maximalen Leistungsabgabe (MPP) für jede der angeschlossenen Energiequelle beeinflusst, welche hier ohne Verwendung von zusätzlichen DC-DC-Wandlern, die in herkömmlichen Ansätzen notwendig sind, ausgeführt ist.

Das vorgeschlagene Regelverfahren - einschließlich einer der Vorsteuerung vom Modulationsindex - wurde unter Verwendung eines einzelnen DSP realisiert. Darüber hinaus wurden im selben DSP die verwendeten Arten der Pulsweitenmodulation (PS-PWM) sowie (SPM) implementiert. Experimentelle Ergebnisse gewonnen an einem Laboraufbau bestätigen die theoretischen Überlegungen. Die PV-Module wurden im Labor mit Hilfe von programmierbaren Gleichstromquellen und die Windturbinen mit Permanentmagnet-Synchrongeneratoren emuliert. Die Ergebnisse zeigen den flexiblen Betrieb des Systems durch den einzelnen MPPT-Betrieb für jede H-Brückenzelle und die symmetrische Injektion der Leistung auch unter unsymmetrischen Bedingungen. Die Möglichkeit, zwischen Stern- und Delta- Konfiguration der Wechselrichtertopologie umzuschalten, wurde vorgeschlagen und analysiert, um die Leistungsfähigkeit der Netzintegration und die Effizienz der Umwandlung zu erhöhen.

Nomenclature

Notation

x	Small letter symbol stands for an instantaneous value
X	Capital letter symbol stands for a DC quantity or RMS. value
$\underline{x} = Re(\underline{x}) + j \cdot Im(\underline{x})$ $= \underline{x} \cdot e^{j \cdot \varphi_x}$	Space vector representation in the complex plane
\hat{x}	Peak value of a signal
$ \underline{x} $	Magnitude of space vector \underline{x}
\tilde{x}	Peak-to-peak value of a signal
\bar{x}	Average value of a signal

Space vector quantities

\underline{i}_s	Stator-current space phasor
$\underline{u}_1, \underline{u}_2$ and \underline{u}_3	Three nearest-voltage space phasors
\underline{u}_s	Stator-voltage space phasor
\underline{u}_i	($i = 1, 2$ or 3) Three nearest-voltage space phasors in α - β coordinate system
\underline{u}'_i	($i = 1, 2$ or 3) Three nearest-voltage space phasors in oblique α' - β' coordinate system
\underline{u}_{ref}	Reference voltage space phasor in α - β coordinate system
\underline{u}'_{ref}	Reference voltage space phasor in oblique α' - β' coordinate system

Symbols

A	Swept area of the turbine rotor
C_p	Power coefficient of the turbine blade
I	Solar cell current

$I_{CHB,(Y-\Delta)}$	Inverter output phase current in the case of $Y-\Delta$ configuration
$I_{CHB,(Y-Y)}$	Inverter output phase current in the case of $Y-Y$ configuration
$I_{CHB,(\Delta-Y)}$	Inverter output phase current in the case of $\Delta-Y$ configuration
$I_{DC,HB\ ij}$	Input DC current of the H-bridge cell, ($i = U, V$ and W), ($j = 1, 2$)
I_{diode}	Diode current
I_m	Solar cell current at the maximum power point
I_0	Reverse saturation current of the diode
I_{photo}	Photo current of the solar cell
I_{PV}	Current of the photovoltaic generator
I_{SC}	Solar cell short circuit current
I_S	Phase current injected to the grid at the secondary side of the transformer
$I_{S,(rated)}$	Rated phase current injected to the grid at the secondary side of the transformer
I_{WT}	Current of the wind turbine generator
K_R	Proportional gain of the PI controller of QPLL
K_V	Temperature coefficient
L_d and L_q	d -axis and q -axis self-inductances
L_f	Inductance of the filter
M	Neutral point of the inverter
N	Neutral point of the secondary side of the transformer
$P_{DC,HB\ ij}$	Power produced and delivered to the grid by the H-bridge cell, ($i = U, V$ and W), ($j = 1, 2$)
P_{PV}	Power produced by photovoltaic generator
$P_{PV,(min)}$	Minimum power produced by photovoltaic generator
$P_{PV,(rated)}$	Rated power produced by photovoltaic generator
$P_{S,(rated)}$	Rated power injected to the grid
$P_{Turbine}$	Mechanical power captured by the turbine blades

P_{Wind}	Actual power of the wind passing through the swept area of the turbine rotor
P_{WT}	Power produced by wind turbine generator
$P_{WT,(min)}$	Minimum power produced by wind turbine generator
$P_{WT,(rated)}$	Rated power produced by wind turbine generator
R_f	Winding resistance of the filter
R_s	Stator winding resistance
$S_{11}, S_{12}, S_{21}, S_{22}$	Switch state combinations
S_{IR}	Sun irradiance
$S_{IR,(min)}$	Minimum sun irradiance
$S_{IR,(rated)}$	Rated sun irradiance
S_U, S_V, S_W	Connection states of phases U, V and W of inverter
$S_{i,U}, S_{i,V}, S_{i,W}$	Connection states of phases U, V and W of inverter using voltage space vector \underline{u}_i
T	Solar cell operation temperature
T_e	Electromagnetic torque
T_n	Period of the grid voltage
T_N	Time constant of the <i>PI</i> controller of QPLL
T_s	Modulation period (interval)
$T_{turbine}$	Mechanical torque produced at the turbine shaft
$U_{A,1}$ and $U_{B,1}$	Fundamental output cell voltage for the upper and the lower H-bridge cell respectively (RMS value)
$U_{CHB,1}$	Fundamental component of the inverter output phase voltage
$U_{CHB,(Y-\Delta)}$	Inverter output phase voltage in the case of <i>Y-Δ</i> configuration
$U_{CHB,(Y-Y)}$	Inverter output phase voltage in the case of <i>Y-Y</i> configuration
$U_{CHB,(\Delta-Y)}$	Inverter output phase voltage in the case of <i>Δ-Y</i> configuration
U_{DC}	DC-link voltage of each H-bridge of the inverter
$U_{DC,HB ij}$	DC-link voltage of the H-bridge cell, ($i = U, V$ and W), ($j = 1, 2$)
U_m	Solar cell voltage at the maximum power point

U_{OC}	Solar cell open circuit voltage
$U_{OC,STC}$	Open circuit voltage of the solar cell at standard test conditions
U_P	Grid line-to-line voltage at the primary side of the transformer
U_{PV}	DC-link voltage of the photovoltaic generator bus
$U_{PV,(min)}$	Minimum DC-link voltage of the photovoltaic generator bus
$U_{PV,(rated)}$	Rated DC-link voltage of the photovoltaic generator bus
U_S	Grid phase voltage at the secondary side of the transformer
U_{WT}	DC-link voltage of the wind turbine generator bus
$U_{WT,(min)}$	Minimum DC-link voltage of the wind turbine generator bus
$U_{WT,(rated)}$	Rated DC-link voltage of the wind turbine generator bus
$\Delta U_{\square PPT}$	Perturbation voltage
ϕ_y	Phase shift between the carrier signals of the H-bridge cells in the same phase
ϕ_x	Phase shift between the carrier signals of the H-bridge cells in the different phases
Ψ_0	Flux produced by the rotor-mounted permanent magnets
c_i	Common-mode component of a switching state of voltage space vector \underline{u}_i ($i = 1, 2, 3$)
d_1, d_2 and d_3	Duty cycles of three nearest-voltage space vectors $\underline{u}_1, \underline{u}_2$ and \underline{u}_3
e_{DC}	Reference voltage error
e_t	Control error for the voltage loop
f_s	Modulation frequency
i_α and i_β	α - and β -components of the inverter current injected to the grid in α - β coordinates
i_d and i_q	d - and q -components of the inverter current injected to the grid in d - q coordinates
i_d^* and i_q^*	d - and q -components of the reference current in d - q coordinates

$i_{DC,HB\ ij}$	Instantaneous value of the input DC current of the H-bridge cell, ($i = U, V$ and W), ($j = 1, 2$)
i_U, i_V, i_W	Instantaneous values of inverter current injected to the grid of phase U, V and W , respectively
$i_{S\alpha}$ and $i_{S\beta}$	α - and β -components of stator current in α - β coordinates
i_{Sd} and i_{Sq}	d - and q -components of stator current in d - q coordinates
i_{SU}, i_{SV}, i_{SW}	Instantaneous values of stator currents of phase U, V and W , respectively
k	Boltzmann constant
k_{PV}	Ratio between the minimum DC-link voltage $U_{PV,(min)}$ of the PV generator bus and the rated voltage $U_{PV,(rated)}$
k_{WT}	Ratio between the minimum DC-link voltage $U_{WT,(min)}$ of the WT generator bus and the rated voltage $U_{WT,(rated)}$
m	Modulation index
m_{PV}	Modulation index for the H-bridge cell connected to the photovoltaic generator
$m_{PV,(max)}$	Maximum modulation index for the H-bridge cell connected to the photovoltaic generator
m_{WT}	Modulation index for the H-bridge cell connected to the wind turbine generator
$m_{WT,(max)}$	Maximum modulation index for the H-bridge cell connected to the wind turbine generator
n_{cell}	Number of cells of one phase of the inverter
n_{DC}	Number of DC sources
n_L	Number of the inverter output voltage level
n_N	Nominal speed of the rotor
n_r	Rotational speed of the rotor
p	Number of pole pairs of machine
p_{av}	Average of the power produced by PV and WT generators
$p_{DC,HB\ ij}$	Instantaneous value of the power produced and delivered to

	the grid by the H-bridge cell, ($i = U, V$ and W), ($j = 1, 2$)
p_d	Instantaneous active power injected to the grid
p_U, p_V, p_W	Sum of the power produced by PV and WT generators of phase U, V and W
q	Electric charge
q_q	Instantaneous reactive (non-active) power injected to the grid
r_U, r_V, r_W	Power imbalance ratio of phase U, V and W respectively
r_T	Radius of the turbine rotor (blade length)
u_α and u_β	α - and β -components of the grid voltages in α - β coordinates
$\hat{u}_{A,1}$ and $\hat{u}_{B,1}$	Peak amplitude of the fundamental output cell voltage for the upper and the lower H-bridge cell respectively
u_{CMV}	Common-mode voltage or common-mode signals
u_{DC}	Measured DC-link voltage
u_{DC}^*	Reference DC-link voltage
$u_{DC-HB\ ij}$	Instantaneous value of the DC-link voltage of the H-bridge cell, ($i = U, V$ and W), ($j = 1, 2$)
$u_{error-HB\ ij}$	DC-link voltage error for the H-bridge cell, ($i = U, V$ and W), ($j = 1, 2$)
$u'_{i,\alpha'}$ and $u'_{i,\beta'}$	α' - and β' -components of voltage space phasor \underline{u}_i ($i = 1, 2, 3$) in 60° oblique α' - β' coordinates system
$u_{L1N}, u_{L2N}, u_{L3N}$	Grid phase voltages for phase $L1, L2$ and $L3$, respectively, in relation to neutral point N of the transformer
$u_{min-max}$	Zero sequence voltage (or minimum-maximum voltage)
u_{MN}	Common mode voltage between the inverter (M) and grid (N) neutral points
$u_{MPPT,HB\ ij}$	Reference voltage for the certain DC-Link obtained by the maximum power point tracking unit, ($i = U, V$ and W), ($j = 1, 2$)
$u_{ref\ d}$ and $u_{ref\ q}$	d - and q -components of the reference voltages in d - q coordinates

$u_{ref\ \alpha}$ and $u_{ref\ \beta}$	α - and β -components of the reference voltages space phasor in α - β coordinates
$u'_{ref,\alpha'}$ and $u'_{ref,\beta'}$	α' - and β' -components of reference-voltage space phasor in 60° oblique α' - β' coordinates system
$u_{ref\ U}$, $u_{ref\ V}$, $u_{ref\ W}$	Reference voltage of phase U , V and W , respectively
$u'_{ref\ U}$, $u'_{ref\ V}$, $u'_{ref\ W}$	Reference voltage of phase U , V and W after <i>per-phase compensation</i> , respectively
$u^z_{ref\ U}$, $u^z_{ref\ V}$, $u^z_{ref\ W}$	Reference voltage of phase U , V and W after injection of the zero sequence voltage, respectively
$u''_{ref\ ij}$	Reference voltage of the individual H-bridge cell after <i>per-cell compensation</i> , ($i = U, V$ and W), ($j = 1, 2$)
u_{UM} , u_{VM} , u_{WM}	Inverter phase voltages for phase U , V and W , respectively, in relation to neutral point M of the inverter
$u_{UM,1}$, $u_{VM,1}$, $u_{WM,1}$	Fundamental component of the inverter phase voltages for phase U , V and W , respectively, in relation to neutral point M of the inverter
u_{UV} , u_{VW} , u_{WU}	Inverter line-to-line voltages
$u_{UV,1}$, $u_{VW,1}$, $u_{WU,1}$	Fundamental component of the inverter line-to-line voltages
u_{U1} and u_{U2}	Cell output voltage of the upper and the lower H-bridge cell of the inverter respectively
u_{sd} and u_{sq}	d - and q -components of stator voltage in d - q coordinates
u_{zero}	Zero sequence signal (or min-max sequence signal)
v_D	Control error of the angle of the grid voltage vector
v_w	Wind speed
$v_{w,(cut-in)}$	Cut-in wind speed
$v_{w,(rated)}$	Rated wind speed
α	Angle of attack
$\alpha_{optimal}$	Optimal angle of attack
θ	Displacement angle between the α - axis and d - axis
θ_D	Phase error between the real and identified angle of the grid

	voltage vector
θ_i and θ_o	Real and identified angle of the grid voltage vector respectively
λ	Tip-speed ratio
$\lambda_{optimal}$	Optimal tip-speed ratio
ξ	Damping coefficient of the modified QPLL
ρ	Air density
ψ_d and ψ_q	d -axis and q -axis flux linkages in the d - q coordinate system
ω	Frequency of the grid voltage
ω_e	Electrical angular speed of the rotor
ω_m	Angular velocity of the turbine shaft
ω_n	Natural frequency of the modified QPLL

Acronyms

3L-NPC VSI	Three-level neutral-point-clamped voltage source inverter
5L-CHB VSI	Five-level Cascaded H-Bridge voltage source inverter
AC	Alternating Current
ADC	Analog to Digital converter
CHB	Cascaded H-Bridge
C-PWM	Continuous pulse width modulation
DAC	Digital to Analog converter
DC	Direct current
DCC	Diode-clamped converter
DC-PWM	Discontinuous pulse width modulation
DSP	Digital Signal Processor
DPC	Direct Power Control
FC	Flying capacitor
FF	Fill Factor
FFMIC	Feedforward modulation index compensation
HB	H-Bridge
HRES	Hybrid renewable energy systems
IGBT	Insulated gate bipolar transistor
IM	Induction Machine
LPF	Low pass filter
MPC	Model predictive control
MPP	Maximum power point

MPPT	Maximum power point tracking
NPC	Neutral-point-clamped
PF	Power Factor
PHD	Phase detector
PI	Proportional-Integral controller
PMSG	Permanent magnet synchronous generator
PLL	Phase locked loop
PS-PWM	Phase-shifted pulse width modulation
PV	Photo voltaic
PWM	Pulse width modulation
QPLL	Quadrature phase locked loop
SCIG	Squirrel cage induction generator
SPM	Space phasor modulation
STATCOM	Static compensator
STC	Standard test conditions
THD	Total harmonic distortion
TNP	Three nearest phasor to the reference voltage
VOC	Voltage Oriented Control
VSI	Voltage source inverter
WT	Wind turbine

Contents

Acknowledgment	I
Abstract	I
Zusammenfassung.....	III
Nomenclature	V
Contents	I
1 Introduction.....	1
1.1 Cascaded H-Bridge multilevel converter	1
2 Fundamentals.....	7
2.1 Multilevel converters topologies.....	7
2.1.1 Neutral Point Clamped Converter (NPC).....	7
2.1.2 Flying Capacitor Converter (FC).....	9
2.1.3 Cascaded H-Bridge Converter (CHB).....	9
2.2 Solar energy.....	10
2.3 Wind turbine generator.....	16
2.3.1 Wind turbine aerodynamics.....	17
2.4 The Space Phasor	23
2.5 Permanent magnet synchronous generator model.....	27
2.6 Modulation Methods for CHB	29
2.6.1 Space Phasor Modulation (SPM)	29
2.6.2 Phase-shifted sinusoidal pulse width modulation (PS-PWM)	40
2.6.3 Phase-shifted sinusoidal pulse width modulation with zero sequence signal injection	45
3 Cascaded H-Bridge converter for the grid connection of hybrid systems	48
3.1 System Topology.....	48
3.2 Operation modes of the hybrid generation system.....	49
3.2.1 Operation of the wind generation sub-system.....	50
3.2.2 Operation of the solar generation sub-system	52
3.2.3 Hybrid operation of wind turbine and PV cells.....	53
3.3 Proposal for reducing the oversizing of the inverter	60

3.4	Control scheme for the grid connection of the Hybrid PV-Wind system.....	65
3.4.1	Voltage oriented control (VOC).....	66
3.4.2	Phase Locked Loop (PLL).....	72
3.5	Feedforward compensation of the modulation index.....	75
3.5.1	Compensation of the reference signals (per-phase compensation)	76
3.5.2	Compensation of the individual reference signals (per-cell compensation).....	81
3.6	Maximum power point tracking (MPPT).....	84
4	Simulation and Experimental Results.....	88
4.1	Introduction	88
4.2	Laboratory setup.....	88
4.2.1	Grid connection system	88
4.2.2	Photovoltaic and Wind turbine emulator.....	90
4.3	Experimental results of the modulation methods.....	95
4.3.1	Space phasor modulation (SPM)	95
4.3.2	Phase-shifted pulse width modulation (PS-PWM).....	96
4.4	Steady state operation of the hybrid system.....	99
4.4.1	Performance of the QPLL	99
4.4.2	Performance of the per-phase and the per-cell compensation.....	100
4.4.3	Simulation and experimental results in balanced operation.....	104
4.4.4	Simulation and experimental results in single cell unbalanced operation.....	109
4.4.5	Simulation and experimental results for two cell unbalanced operation.....	116
4.4.6	Experimental results at minimum PV-power and rated WT-power.....	121
4.4.7	Experimental results for rated PV-power and minimum WT-power.....	125
5	Summary and Conclusions	129
6	Appendix.....	131
6.1	Parameters of lab grid connection hybrid system	131
	References.....	132

1 Introduction

Multilevel converters have become the enabling power conversion technology for high-voltage, high-power applications. In order to reach high voltage and high power with the available switching devices and to improve output waveforms, multilevel inverters were developed and continuously improved in the last three decades and can be found in many industrial applications [1]. In the range of medium-voltage systems, the majority of manufacturers offer, in addition to the conventional two level inverters, multilevel inverters with different topologies and for a variety of applications. The most common topologies used in industrial drives are the three-level Neutral Point Clamped (NPC) inverter, the four-level Flying Capacitor (FC) topology and the Cascaded H-Bridge (CHB) inverter. Multilevel inverter with five, seven and nine levels also find a niche in the market [2]. Inverters with higher number of levels are still under development and many new contributions and new commercial topologies have been reported in the last few years [3]-[9].

1.1 Cascaded H-Bridge multilevel converter

The three-phase cascaded H-Bridge (CHB) multilevel converter topology has been widely proposed for photovoltaic (PV) conversion applications [10]-[20] and for wind turbine (WT) energy conversion applications [22]-[26]. It offers a modular solution by collecting large numbers of isolated DC sources that allows the generation of a large number of voltage levels in the output. Additionally this topology allows an individual maximum power point tracking (MPPT) for each H-Bridge power cell obviating in this way the use of extra DC-DC converters, which improves the conversion efficiency of the system and reduces the total cost [12]. The CHB offers an inherent isolation between the PV arrays that are feeding the different H-bridges and prevents in this way high voltages that can occur in series connected PV in other topologies. Thus a cascaded inverter is one of the best choices for high voltage grid-connected photovoltaic systems [10][14].

Diverse methods have been reported in literature to interface PV sources to the grid by using a CHB topology and were verified by means of simulation and recently also by laboratory measurements [10]-[20]. A crucial aspect in the connection to the grid by using a CHB topology is the power imbalance caused by the fluctuations of the irradiance in the PV panels that yields different power on each H-bridge and consequently to unsymmetrical power in each phase. In the literature several solutions to this problem have been proposed. In the following, some important works that deal with this complex, that are closely related to the present investigation and are discussed.

A three phase CHB system for connecting PV sources is considered in [10]. The traditional voltage oriented control (VOC) scheme is extended with two additional control blocks. One of them is used to perform a maximum power point tracking for each power cell without using an additional DC-DC-converter unit and the other one is introduced to control the DC-link voltages, in this way the effect of unequal power production among the HB cells in the same phase of the inverter can be mitigated. In the proposed a feedforward control loop is used for enhancing the dynamic behavior and acts directly into the modulator. The performance of the proposed methods was evaluated by means of simulation.

A model predictive control (MPC) was proposed in [11] to control the DC-link voltages achieving the optimal value to meet MPPT requirement without using extra DC-DC converters. Simulation and measurements on an experimental setup confirm the proposed approach.

A multilevel-multistring configuration was introduced in [12]. It is based on a three-phase 7-level CHB converter with multiple string and with DC-DC converters for obtaining a MPPT in each module. The researched system is able to handle the inherent power imbalances that occur not only among the cells of one phase but also appear among the three phases. Only simulation results validate the proposed topology and the control method.

The same configuration used in [12] was adopted in [13] with the difference that each HB cell was connected to a DC-DC converter in order to perform MPPT individually. Furthermore, a space phasor modulation technique (SPM) is used instead of the phase shift modulation. A balanced current injection is achieved with maximum efficiency. The proposed control scheme was also validated only by means of simulation.

Two types of feedforward power compensation methods were investigated in [14] on a system similar to [12] in order to achieve two targets: on the one hand the compensation of imbalance among the cells of the same phase and on the other hand the power imbalance among the phases. The improvement of this approach compared to [12] is that the MPPT algorithm was carried out by the feedforward compensation in the modulation stage and no extra DC-DC converters were necessary. For the confirmation of the scheme, only simulation results have been shown.

The results of simulation presented in [15] show that both types of power imbalance (among cells and among phases) in the CHB topology can be eliminated by connecting the whole PV generated power to a single DC-bus bar. A conventional voltage oriented control was used for the grid tie CHB inverter to control the grid currents and DC-bus bar voltage without the need of any balancing algorithm.

The present investigation departs from the ideas and structures proposed in [12]-[15]. Since at the beginning of this work most of the research results in the area were validated only by simulations, the first step in this doctoral project was to create an experimental environment for analyzing and extending the known ideas [21]. In the meanwhile, the other research group [16]-[20] has also obtained and published important experimental results that in contrast to one of the main ideas in this dissertation do not address the topic of hybrid systems. In [18] and [19] several zero-sequence injection methods have been proposed for solving this as an expansion of the conventional zero-sequence injection that handles only the phase power imbalance. Here, an isolated DC-DC converter was used to perform the MPPT for each PV generator. The effectiveness of the proposed methods was verified by means of simulation and experimentally on a three-phase, seven-level CHB prototype.

Regarding hybrid generation, solar and wind energy are, among other renewable sources, easily available and distributed all over the world. Thus, the generation with photovoltaic panels (PV) and wind turbines (WT) has been significantly increasing. Thanks to the continuous developments of the necessary power electronics converters. In general, the use of PV- and WT-power generation in a complementary manner is of advantage in order to reduce the fluctuation of energy production. The wind in sunny days is usually weak while strong wind often appears on cloudy days or in the night. This approach would also yield a better utilization of the power conversion system and a reduction of its complexity and of its cost [27]. However the grid connection of such hybrid renewable energy systems (HRES) is still under development and face many challenges in terms of efficiency, cost and complexity [28].

In the literature different topologies and control schemes for the HRES comprising solar- and wind energy can be found, which are useful for island operation or micro-grid system. Some researchers focus on the investigation of the grid integration of HRES as reported in [27]-[33]. The usual way to perform the grid integration of such mixed system e.g. in a micro-grid is realized by converting the energy of the different sources (wind, hydro, solar, fuel-cells, batteries and other storage systems) in a single DC-link, then the energy is converted into AC and injected to the grid using a conventional two-level inverter [27][29]-[32]. A new scheme of grid connection of photovoltaic source in conjunction with a doubly fed induction generator for wind energy that reduces the complexity of the system has been presented in [33]. There both the grid as well as the rotor-side power converter of the doubly fed induction generator inject PV power into the grid.

After a review of the literature it can be concluded, that there is still a potential for the research on the direct grid connection of hybrid sources consisting of PV and wind energy that has motivated this work.

In the following, a three-phase cascaded H-bridge multilevel inverter topology is proposed to perform the grid integration of PV panels and variable speed wind turbines in a modular hybrid generation system. This configuration aims, in addition to

fault redundancy and modularity, at a lower fluctuation of the power injection to the grid, since the availability of each energy source is differently distributed over 24 hours of a day. Due to the use of different type of energy sources, the DC-link voltages and consequently the deliverable power of the H-bridge cells in the same phase of the inverter are typically not equal. Moreover, partial shading, model mismatches and dust accumulation on the PV arrays cause unsymmetrical power generation among the phases of the inverter. Furthermore, the difference in wind speed yields unbalanced power production among wind turbines in the same field. These lead consequently to an unbalanced current injection to the grid that has to be actively compensated.

Regarding the control, the present research work uses a voltage-oriented control (VOC) together with a feedforward compensation strategy as described in [14]. The adopted structure is suitable for handling the unsymmetrical power generation of the mixed energy sources in the same phase as well as the unbalance power production among the phases of the inverter.

One main contribution of this research work is the study of the grid connection of hybrid energy sources consisting of solar panels and wind turbines by employing a 5-Level cascaded H-bridge inverter (5L-CHB-VSI) under the different operating conditions, in which the inherently unbalanced power production in the sources is taken into account. The system was realized on an experimental laboratory set-up that was used for examining its behavior and for the validation of the theoretical ideas. Moreover, in the practical implementation the solar arrays as well as wind turbines were also properly emulated. The investigation was comprehensive and included the development of the control strategy to interface the hybrid energy sources under adverse conditions, the achievement of the MPPT of each energy source without using extra DC-DC converters, providing in this way a low-cost solution and an enhancement of the reliability of the system.

A second important contribution is the analysis of a reconfiguration of the topology of the structure featuring a Star-Delta switching that can enhance the properties of the generation system.

This dissertation is structured as follows: Chapter 2 describe the fundamentals, it includes the description of the most common multilevel inverters topologies, the mathematical model of solar panels and wind turbine generators were given as well as the mathematical model of the permanent magnet synchronous generator PMSG. Moreover, SPM and PS-PWM techniques are presented. In chapter 3, the operation modes of the hybrid generation system, VOC, feedforward modulation index compensation, phase locked loop and MPPT technique are discussed, the star-delta reconfiguration is considered and analyzed in this section as well. In chapter 4, simulation and experimental results of a 5-level H-bridge inverter prototype are shown and discussed, in order to validate the feasibility of the proposed methods for different operating conditions. Finally, the conclusions are stated in chapter 5.

2 Fundamentals

In the following the basic principles the power electronic inverters as well as the dynamic models that describe the behavior of PV panels and of wind turbine generators are presented as they are needed for the understanding of the idea proposed in this research. Besides, the well-known techniques: Space Phasor and Phase Shifted Pulse Width Modulation (SPM and SP-PWM respectively) are discussed as central elements of the realization.

2.1 Multilevel converters topologies

The multilevel converter technology started with the introduction of the multilevel stepped waveform concept by using series-connected H-bridge, which is also known as cascaded H-Bridge converter, in the late sixties. The Flying Capacitor (FC) topology was developed immediately afterward, for low-power application. In the late seventies, the diode-clamped converter (DCC) was introduced. The DCC concept had evolved into the three-level NPC (3L-NPC) converter, which can be considered as the first market-ready multilevel power converter for medium-voltage applications. Later, the CHB was reintroduced in the late eighties, and found its way to the market in the mid- nineties. In the same way, the early concept of the FC- inverter that had been initially constructed for low power applications was further developed into the medium-voltage multilevel converter in the early nineties [3].

2.1.1 Neutral Point Clamped Converter (NPC)

The Neutral Point Clamped Converter (NPC) inverter topology is simply considered as an expansion of the two-level inverter by splitting the DC-link voltage in the middle point to acquire an additional zero voltage level. Two series connected capacitors are now required to stabilize the split DC-links. In this structure and due to the additional voltage level, each power semiconductor switch has to withstand at most the half of the DC-link voltage, and the 3L-NPC inverter can achieve the double rated DC-link voltage as compared with the conventional two-level inverter by using the same

semiconductor power devices. The basic structure of one leg of a neutral point clamped converter is depicted in Figure 1 (a). The 3L-NPC has become an industry standard inverter and is produced by different manufactures. The NPC structure can be extended to higher number of levels, nevertheless these are less attractive because of the higher losses, uneven distribution of losses among the outer and inner switching devices, etc. In particular, the clamping diodes having to be connected in series to block the higher voltages introduce larger conduction losses and reverse recovery losses during commutation. All these issues reduce the efficiency and increase the complexity of a higher number of levels in the NPC. Furthermore, the control for balancing the different DC-link voltages by using conventional modulation becomes unattainable in case of higher level, especially if a passive front end inverter is used. Here, the typical staircase waveform of the output voltage cannot be ensured, since multilevel transition in each output phase is necessary to balance the capacitors for certain modulation indexes, this causes higher switching losses and induces higher $\frac{du}{dt}$.

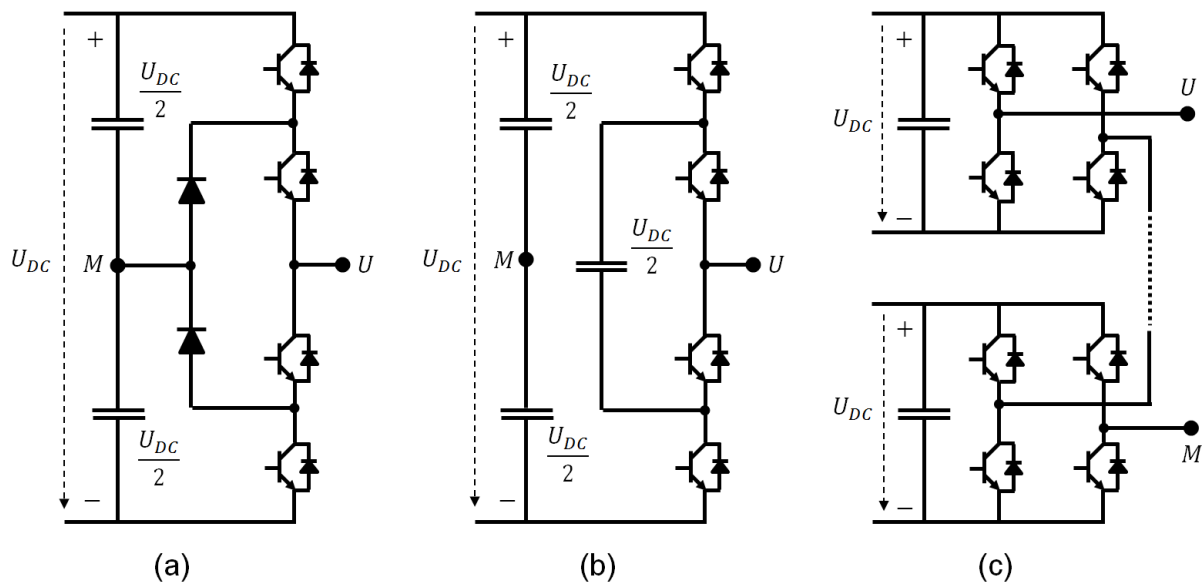


Figure 1 One leg of common multilevel converter topologies (a) 3L-NPC, (b) Three-level FC, (c) Five-level CHB.

2.1.2 Flying Capacitor Converter (FC)

The basic structure of one leg of the Flying Capacitor Converter (FC) is depicted in Figure 1 (b). Although the Flying Capacitor Converter features a modular structure, its relevance in industrial applications seems to be less if compared to the NPC and CHB. One of the reasons for its low acceptance is the fact that higher switching frequencies are necessary to keep the capacitors properly balanced, regardless if a self-balancing or a control-assisted balancing modulation method is used (e.g., greater than 1200 Hz). Until now this switching frequency range was not feasible for high-power applications. In order to keep the switching losses within acceptable limits the frequency is often limited to a range of 500 - 700 Hz in medium-voltage inverters. As an additional disadvantage this topology requires the initialization of the FC voltages.

2.1.3 Cascaded H-Bridge Converter (CHB)

The basic structure of one leg of a Cascaded H-Bridge Converter (CHB) is shown in Figure 1 (c). Each H-bridge cell in the phases of the inverter has an own DC-link and generate a modulated voltage at its output terminals. The total output voltage in each of the phases is obtained by the sum of the individual output voltages in each H-bridge that is able to produce three output voltage levels, namely, $+U_{DC}$, $-U_{DC}$ and 0. Each DC voltage has to be isolated, which is usually attained by using an arrangement of rectifiers and transformer with a multi-winding secondary to provide the electrical isolation. In some applications, these DC-link voltages can be obtained directly by isolated DC energy sources, e.g. DC-DC isolated converters or photovoltaic arrays. In other applications which do not require the injection of active power like static compensator (STATCOM), the DC voltages can be floating and the control strategy forces the DC-link voltage following to the reference. The number n_L of possible output levels of each phase is $n_L = 2n_{DC} + 1$, where n_{DC} refers to the number of DC sources. Due to its modularity the CHB topology is suitable for high-power applications. An operation at higher voltage levels is feasible even if using power semiconductors with lower rated voltages. Like in all other multi-level topologies the spectrum and consequently the THD of the output voltage becomes better for the

same switching frequency with all the associated advantages i.e. the same quality of the voltage can be obtained at a lower level of losses with the disadvantage of a higher number of power and signal electronic components [3].

CHB topology has some other advantages such as the modular, flexible design, the easy installation and it requires a minimum number of components when compared to other multilevel inverter topologies with the same number of levels. However, as already mentioned, it requires a large number of isolated DC sources. In case of drive applications they have to be fed via isolation transformers, which are more expensive and bulky, compared with the standard transformer used for the NPC that in addition can be effectively used to improve the input power factor of the converter and to reduce the current harmonics if properly connected in a high pulse rectifier

Conversely in applications in which multiple separate DC sources are already available such as the solar energy PV panels or hybrid systems with multiple isolated sources the topology CHB becomes very attractive.

2.2 Solar energy

Solar energy is one of the biggest renewable energy sources in the world. The power density of the solar irradiance reaches up to $1,373 \text{ kW/m}^2$ outside the atmosphere. A part of this energy is dissipated in the atmosphere, reducing the solar irradiance at the ground to about $1,0 \text{ kW/m}^2$ in the tropics at noon. This energy can be utilized by converting it to other energy forms like the remote energy, electric energy, etc. The conversion of solar energy to electrical energy can be either indirect or direct. In the first case, the energy is initially transferred to thermal energy to heat up a medium, then, in a second step transferred to mechanical energy using a turbine and finally converted to electrical energy using a generator. An example of indirect energy conversion is for instance a solar thermal power plant, which is based on the accumulation of the solar power using controlled mirrors focusing at the boiler installed in the top of a tower in order to generate steam. The latter is used to drive the electrical generator connected to the steam turbine. However, the direct approach to

convert solar energy to electrical energy is performed through the so called “photovoltaic effect” which represents the basic principle of the solar cell to generate electrical energy.

The electrical power produced by a solar cell can thus be utilized in home services like refrigerators, lighting, TV, etc. This is especially interesting in remote regions, which have no access to the classical electrical power grid, these kinds of PV power system applications are called stand-alone PV systems. However, additional storage units like battery bank are required in such cases. Furthermore, the PV energy may also be used to support other, nonrenewable stand-alone power generation systems like Diesel generators, in order to enhance the operation performance of those generation units and increase the generation availability. Such systems are called hybrid energy generation systems.

The other way to utilize the PV energy is to connect the solar cells to the utility grid across a power electronics converter without the need to install additional storage units. This kind of utilization of the solar energy can be performed by means of two scenarios: First, the injection of the PV power with a low voltage inverter to the low voltage grid. This configuration is used when only a few PV panels in the power range of several kW are used, which can frequently be seen on the roof of private houses. However, this configuration can also be used in the medium power range up to several hundreds of kilowatts. The second scenario is the injection of the PV power with a medium voltage inverter (i.e. multilevel converter) to the medium voltage grid. This configuration is used in large scale solar parks in the range of several megawatts [34].

The solar cell is the smallest element in the PV generator and represents the basic element responsible to convert the solar energy to the useful electric energy. The structure of a solar cell is very similar to the one of a diode. It is built by two layers of semiconductor material (generally silicon) having different electrical properties resulting from a doping processes. The P-Type semiconductor material contains charge carriers which are of a positive polarity and are known as holes. In the N-Type material the charge carriers are electrons which are negative in polarity. The positively

doped material can be obtained by inserting e.g. a low concentration of boron atoms while the other layer is negatively doped by using e.g. phosphor atoms in the Si-Cristal. Due to the different doping of the layers, an electrical field will appear at the junction between the different layers.

When light reaches the solar cell, the energy stored in the photons of the incoming light creates free charge carriers. Those carriers are separated by the electric field at the junction between the two layers. At this moment an electric voltage is generated at the external terminal and a current will flow if a load is connected between the terminals. The current which is internally generated in the solar cell is called “photo current” I_{photo} and is directly proportional to the light intensity. Figure 2 shows the simplified equivalent circuit of the solar cell which consist of a current source which produce the photo current I_{photo} connected in parallel with a Diode [34].

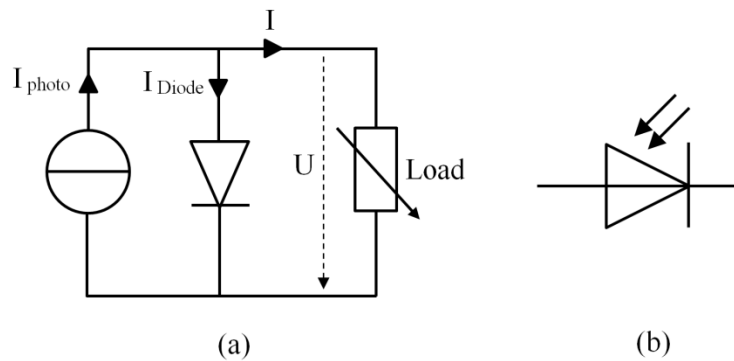


Figure 2 Solar cell (a) equivalent circuit (b) circuit symbol

If a variable resistor is supposed as load and connected to the terminal of the solar cell, the terminal voltage of the cell will behave as follows: if the resistance is reduced to zero (short circuit) the terminal voltage which is also the voltage across the diode, voltage will be approximately zero. The photo current generated by the solar irradiance will flow completely in the output load. This current is called short circuit current I_{SC} , which is the maximum current produced by the solar cell, when it is short circuited. If the resistance is increased to infinity (open circuit), the load current I will be zero. Thus, the photo current will flow in the diode while generating a voltage at the

terminal of the solar cell. This voltage is called the open circuit voltage U_{OC} , which is defined as the maximum voltage which can be generated between the terminals of the solar cell at a load current equal to zero. If the resistance is varied in the range between zero and infinity, the photo current will be distributed between the diode and the load, producing a certain voltage at the terminal of cell. The current flowing in the solar cell can be written depending on the diode characteristic curve as:

$$I = I_{photo} - I_{diode} \quad (1)$$

$$I = I_{photo} - I_0 \left(e^{\frac{qU}{kT}} - 1 \right) \quad (2)$$

where I_{diode} is the diode current, I_0 is the reverse saturation current, q is the electric charge, k is the Boltzmann constant and T is the absolute operating temperature [34]. Figure 3 represents the typical relationship between the output current and voltage of a solar cell (blue curve) where the solar cell is able to work at any point along the characteristic curve.

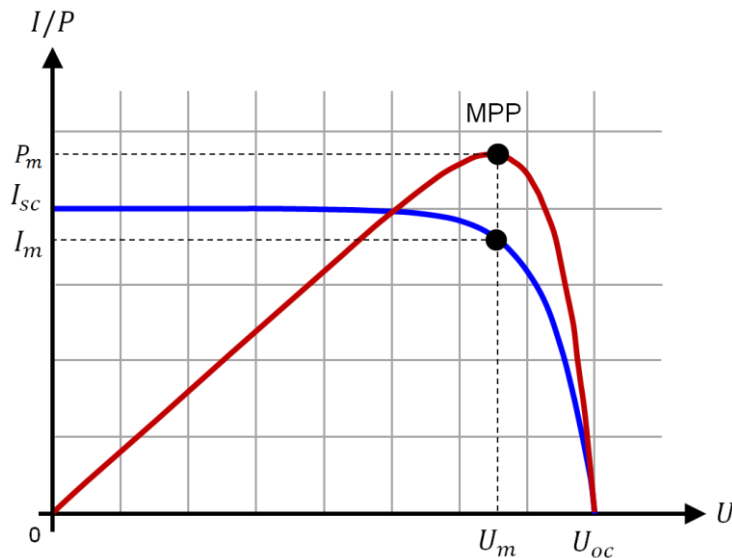


Figure 3 Current and power versus voltage characteristic for a typical solar cell

It is possible to say that the short circuit current I_{SC} is proportional to the sun irradiance level, while the open circuit voltage U_{OC} has a nonlinear dependency to the

sun irradiance. The power characteristic curve can be obtained directly from the (U - I) curve of the solar cell by multiplying the voltage and current like depicted in Figure 3, where the red curve represents the typical power characteristic of a power cell. From the power curve it can be recognized that there is a unique point at the curve where the solar cell produces its maximum power, this point is known as the maximum power point (MPP). The corresponding cell voltage and current at the MPP are given as (U_m, I_m), respectively. The solar cell manufacturers intent to maximize the power produced by the solar cell through maximizing the open circuit voltage U_{OC} and short circuit current I_{SC} as well as the fill factor FF . The fill factor is the expression used to measure the quality of the solar cell which represents the ratio between the actual maximum power ($U_m \cdot I_m$) and the theoretical one ($U_{OC} \cdot I_{SC}$) and expressed by [35]:

$$FF = \frac{U_m I_m}{U_{OC} I_{SC}} \quad (3)$$

Thus, the more approaches of the FF to the unity means the higher quality of the PV cell. For solar cells based on silicon, the typical FF is in the range of 0,6 – 0,8.

The silicon solar cell typically produces open circuit voltage U_{OC} of 0,5 volt only, therefore a number of cells are connected in series in order to produce a higher voltage. This configuration is called “PV-module”. Additionally, a number of PV modules are connected in parallel to produce a higher current. The resulting connection is supported by a frame, which also includes robust terminals and an additional layer made of glass to protect the solar cells. This configuration is called “PV panel”. Normally more than one panel is connected in series and parallel in order to reach the user requirements of voltage and power. This arrangement is called “PV array”, Figure 4 illustrates the different terms of the PV generator.

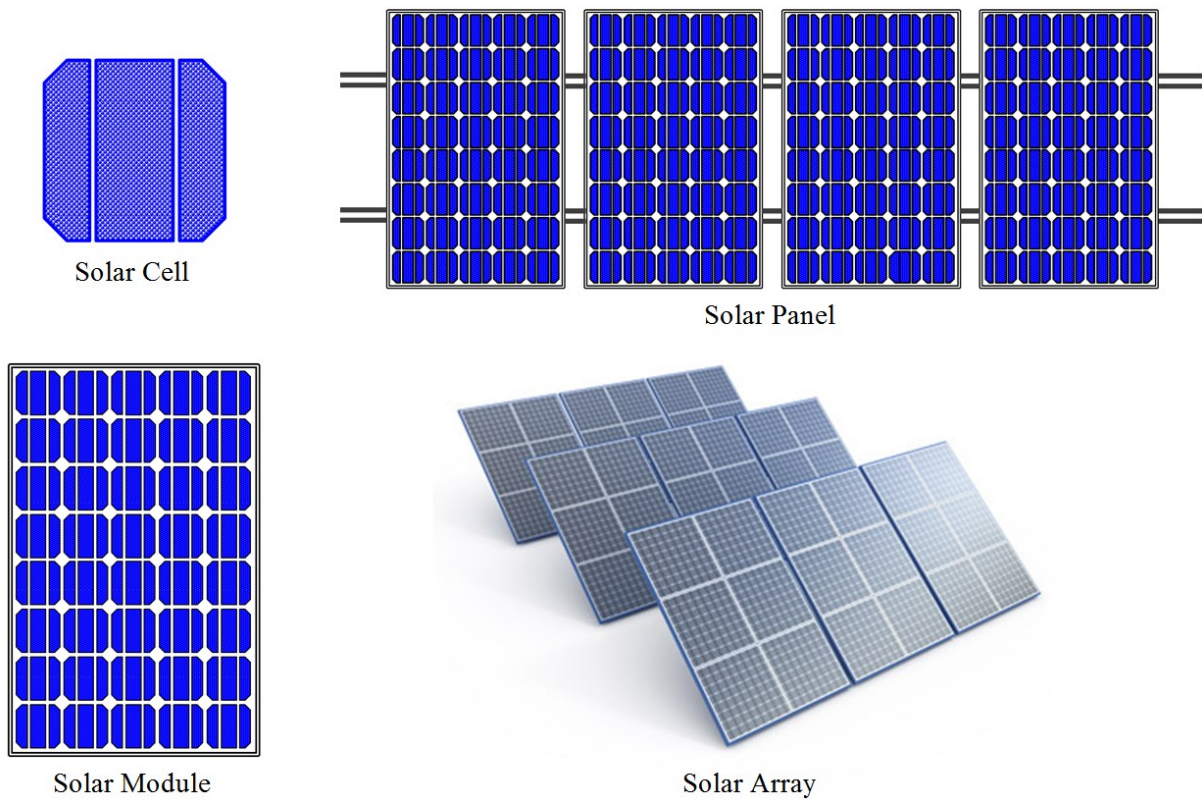


Figure 4 Different PV generator terms

The performance of the solar cell is strongly affected by two factors: the sun irradiance and the ambient temperature. As it was mentioned before the photo current is directly proportional to the sun irradiance, thus the reduction in the sun irradiance at a given operating temperature leads to a reduction in the short circuit current I_{SC} and therefore to a reduction of the MPP as shown in Figure 5 (a).

The temperature slightly affects the short circuit current I_{SC} while it has a strong affect to the open circuit voltage U_{OC} according to the following expression [36]:

$$U_{OC}(T) = U_{OC,STC} + (K_V \cdot T) \quad (4)$$

where $U_{OC,STC}$ is the open circuit voltage of the solar cell at standard test condition (STC) (i.e. ambient temperature is 25° C and 1000W/m² solar irradiance). K_V is the temperature coefficient of the solar cell, T is the absolute operating temperature. The temperature coefficient K_V for the silicon based solar cells is negative. Thus, according to (4) the increment in the operating temperature leads to a reduction of the open

circuit voltage U_{OC} and the maximum power produced by the cell is also reduced. Figure 5 (b) shows the effect of the operating temperature to the characteristic curves of the solar panel at given sun irradiance.

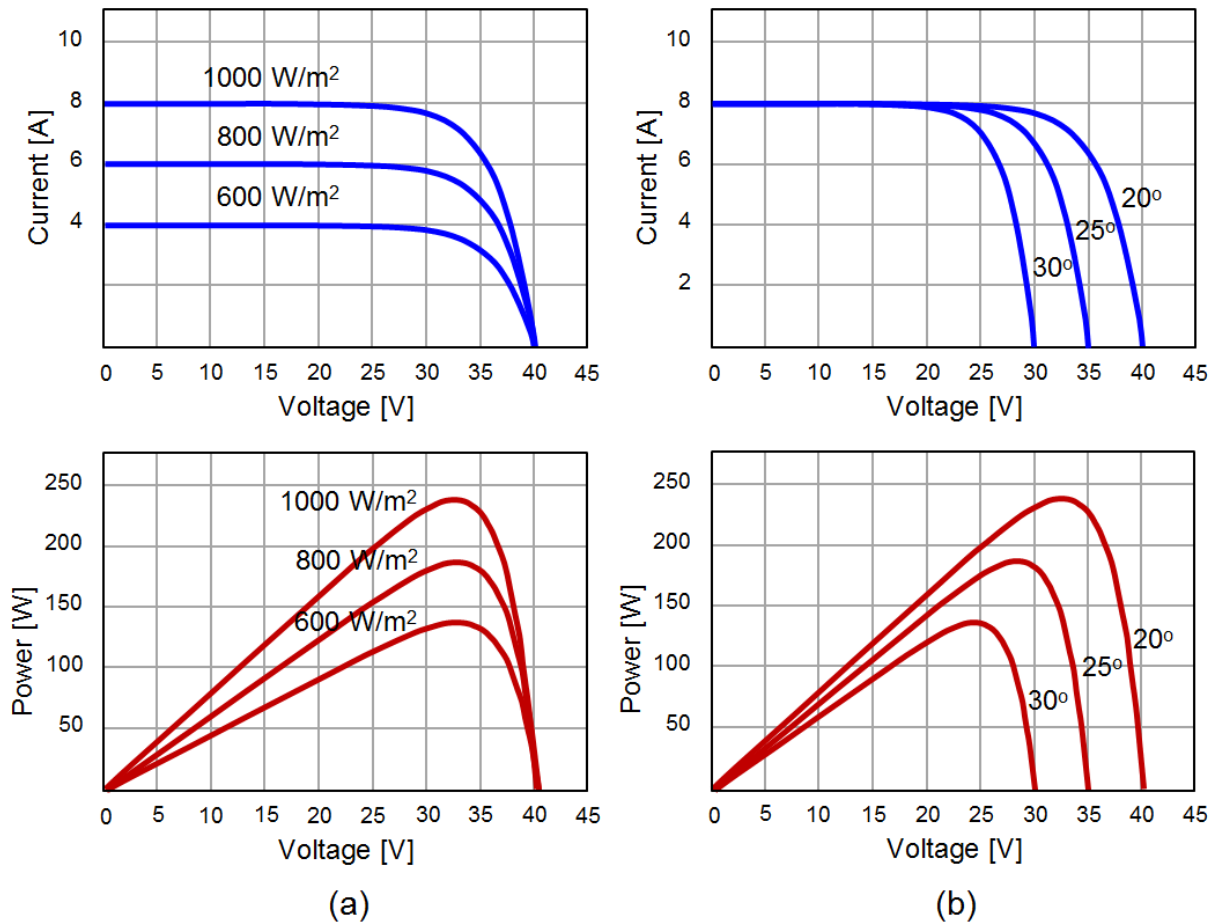


Figure 5 Current and power versus voltage for a typical solar panel, showing the different maximum power points due to (a) different sun irradiation levels (b) different temperature levels

2.3 Wind turbine generator

The wind turbine generator consists of two main parts: the wind turbine and the generator. The task of the turbine is to convert the wind kinetic energy to rotational mechanical energy while the generator converts this energy to the electrical energy. There is a wide range of wind turbine capacities starting from less than 5kW to more than 5MW for the large-scale units. There are two main types of wind turbines: the

direct drive wind turbine where the turbine shaft is directly connected to the generator. In this type of turbine a low speed generator is used (for example 120 poles, permanent magnet synchronous generator PMSG). The other type of turbine uses a gearbox to perform the mechanical connection between the turbine and the generator. The gearbox is used to transfer the mechanical power from the low speed at the turbine side to the high speed at the generation side. For this type of turbine, a so called high speed generator is used (for example a standard 4 pole, 1500 *rpm*, 50Hz squirrel cage induction generator SCIG) [37].

2.3.1 Wind turbine aerodynamics

2.3.1.1 Angle of Attack

The turbine rotor consists of several blades (usually three blades) which are mounted on the rotor hub. In the large scale wind turbine each blade has the possibility to change its direction to attack the wind within a certain angle. This angle is called “angle of attack α ”. It can be defined as the angle between the cord line of the blade and the direction of the wind speed. Figure 6 shows the cross section of the wind turbine blade with the certain angle of attack α . The possibility to change the blade angle is called “pitch mechanism”. If the wind speed is in the range between the low speed and the rated speed, the angle of attack is kept at the value called “optimal attack angle $\alpha_{optimal}$ ” in which the turbine can capture the maximum available power from the wind. In the case that the wind speed is higher than the rated speed the angle of attack is adjusted by some degrees (usually 20° to 25°) in order to keep the produced turbine power within the designed capacity. In the case that the wind speed increases further and reaches the turbine limitation, the blades will pitched out of the wind. In this case no power is produced by the turbine and the turbine shaft is blocked by a mechanical break to protect the overall system [37].

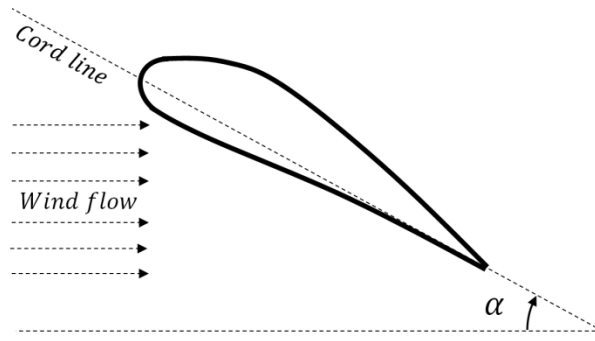


Figure 6 wind turbine blade and angle of attack

2.3.1.2 Wind power

The actual wind power of an air mass flowing at a speed v_w through an area A can be expressed by [38]:

$$P_{wind} = \frac{1}{2} \rho A v_w^3 \quad (5)$$

ρ is the air density, A is the swept area of the turbine rotor, v_w is the wind speed.

2.3.1.3 Mechanical power of the turbine

The wind power captured by the blade and converted to mechanical power can be expressed by:

$$P_{Turbine} = \frac{1}{2} \rho A v_w^3 C_p(\lambda, \alpha) \quad (6)$$

where λ is the tip-speed ratio, C_p is the power coefficient of the turbine blade, which represents the relationship between the mechanical power captured by the turbine blades and the actual power of the wind passing through the same swept area of the turbine rotor.

$$C_p = \frac{P_{Turbine}}{P_{Wind}} \quad (7)$$

The power coefficient is the function of the rotational speed and the angle of attack α , so that each turbine has a certain range of the C_p . According to the Betz limitation; the power coefficient has theoretical maximum value of 0,59 [37].

2.3.1.4 Tip-Speed Ratio

The tip speed ratio λ is one of the important parameter of the wind turbine, it represents the relationship between the blades tip-speed and the wind speed expressed by:

$$\lambda = \frac{\omega_m r_T}{v_w} \quad (8)$$

where ω_m is the angular velocity of the turbine shaft, r_T is the radius of the turbine rotor (blade length) and v_w is the wind speed. Figure 7 shows the power coefficient versus the tip-speed ratio for the different angle of attack [37]. The maximum power coefficient is obtained at the optimal tip-speed ratio $\lambda_{optimal}$ and optimal angle of attack $\alpha_{optimal}$. For a certain turbine the optimal tip-speed ratio is constant so that the speed of the turbine that produces maximum power by the turbine can be expressed by:

$$\omega_m = \lambda_{optimal} \frac{v_w}{r_T} \quad (9)$$

Depending on the previous expression (9) the turbine speed ω_m must be continually adjusted depending on the wind speed v_w in order to track the maximum power.

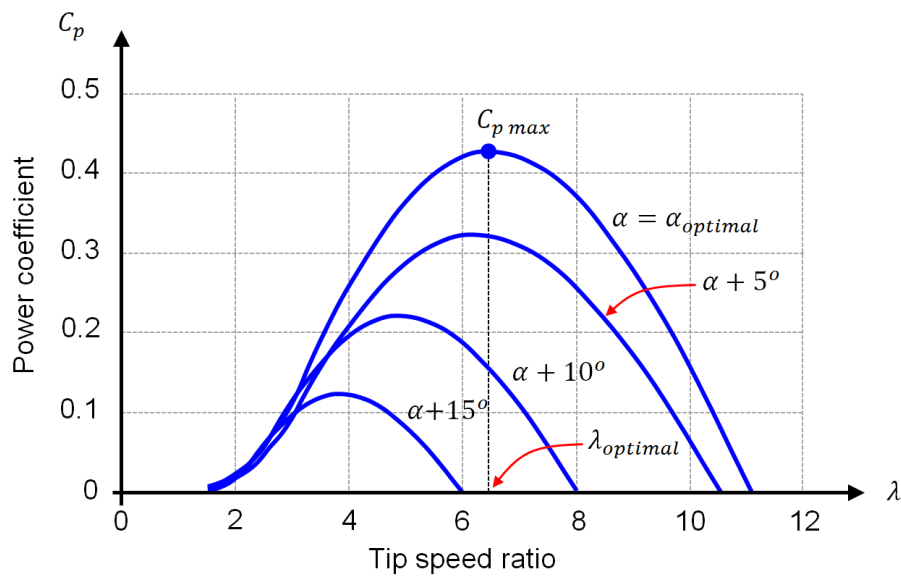


Figure 7 Power coefficient characteristics

2.3.1.5 Power characteristic curve

The power curve of the wind turbine represents the relationship between the mechanical power of the turbine $P_{Turbine}$ and the wind speed v_w . It is one of the main important facts of a turbine and often given by the manufacturer. Figure 8 shows the turbine mechanical power $P_{Turbine}$ at different wind speeds. Three different modes of operation can be recognized from the figure: parking mode, maximum power point mode (MPP-Mode) and constant power mode or rated mode.

The parking mode is the mode of operation where the wind speed v_w is in the range between zero and the cut-in wind speed at which the turbine starts the rotation and produce power. In this mode if the turbine system operates, it produces a power less than the power consumed by the internal turbine system so that the blades are pitched out of the wind and the turbine shaft is blocked to standstill by a mechanical brake. The parking mode is also applied when the wind speed exceeds the cut-out speed. In this case, the blades are pitched out as well and the turbine shaft is blocked to zero.

The maximum power point mode is applied when the wind speed v_w lies in the range between the cut-in and the rated speed. In this mode, the power captured by the turbine

is lower than the rated value of the generator. Thus, the blades of the turbine are pitched to the optimal angle of attack $\alpha_{optimal}$ and the turbine speed ω_m will be set according to the wind speed like expressed in (9) in order to track the maximum power point. The tracking process is performed through the proper control of the generator.

The constant power mode (rated power mode) is applied when the wind speed v_w is in the range between the rated speed and the cut-out speed. In this case, the power generated by the turbine is larger than the rated power of the generator, so that the mechanical power $P_{Turbine}$ captured by the blades is kept constant by controlling the angle of attack (pitch control).

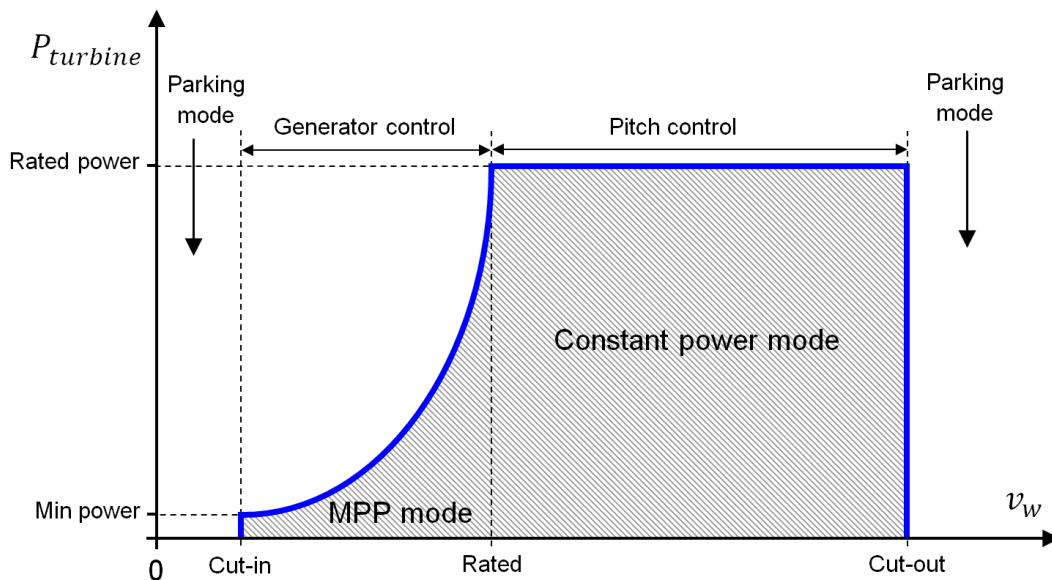


Figure 8 Wind turbine mechanical power versus wind speed characteristic curve

Figure 9 shows the typical wind turbine power-speed characteristics operating at different wind speeds in the MPPT mode. The power speed curves are obtained with the optimal angle of attack $\alpha_{optimal}$ of the blades.

For a given wind speed, the power curve reaches the maximum power point (MPP) at the optimal tip-speed ratio $\lambda_{optimal}$ with a corresponding rotor speed ω_m of the turbine. Therefore, under the different wind speeds, the rotor speed of the turbine has

to be controlled in order to keep the turbine producing the maximum power along the MPP curve.

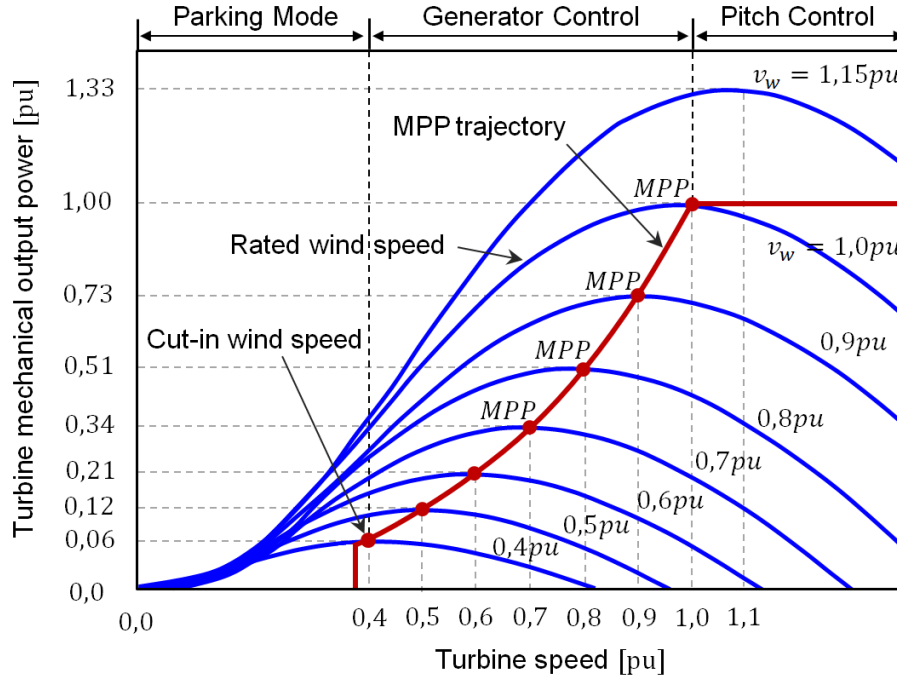


Figure 9 Wind turbine power-speed characteristics with maximum power point trajectory

As stated above, in the MPP-Mode the tip-speed-ratio as well as the angle of attack ($\lambda_{optimal}$ and $\alpha_{optimal}$) are held constant to their optimal values. Therefore, the power coefficient C_p also remains constant and finally the following expression can be derived from (6):

$$P_{turbine} \sim \omega_m^3 \quad (10)$$

$P_{turbine}$ can be expressed in terms of torque as:

$$P_{turbine} = T_{turbine} \omega_m \quad (11)$$

where $T_{turbine}$ is the mechanical torque produced at the turbine shaft. So that the relationship between the mechanical torque and the rotational speed of the turbine is:

$$T_{turbine} \sim \omega_m^2 \quad (12)$$

The red line depicted in Figure 9, represents the maximum power curve based on the previous expressions. Thus, the optimal speed or torque reference of the turbine can be determined and used to control the generator to achieve the MPP operation.

2.4 The Space Phasor

The space phasor theory presented by Kovacs [39] provides a powerful tool for the description of the dynamic behavior of three phase machines. Although this theory was originally used to describe rotating machines, it also can be applied to describe three phase systems in general. However, as the origin of this idea was to describe machines, the principle idea is also described here for the use with machines.

The space phasor theory is based on the idea that the revolving field generated by currents in symmetrically spatially distributed windings can be represented by a space phasor pointing to the maximum magnetic flux wave density. Due to the relationship existing between fluxes, currents and voltages, this concept can be extended to other quantities in the machine [40]. Thus, if i_{SU} , i_{SV} and i_{SW} are the instantaneous current values in stator phases U, V and W respectively, the stator current space phasor, \underline{i}_S is defined by:

$$\underline{i}_S = \frac{2}{3} \cdot [i_{SU} + \underline{a} \cdot i_{SV} + \underline{a}^2 \cdot i_{SW}] \quad , \quad (13)$$

where

$$\underline{a} = e^{j \cdot 2\pi/3} = -\frac{1}{2} + j \cdot \frac{\sqrt{3}}{2} \quad . \quad (14)$$

The coefficient $2/3$ is a scaling factor, which reflects the fact that the total current density distribution of the three windings is equivalent to that of only two orthogonal phase windings. As seen from (13) and (14), the complex numbers \underline{a} and \underline{a}^2 are used solely to define the spatial directions of i_{SU} , i_{SV} and i_{SW} . These complex quantities always remain orientated in the same fixed position with respect to the stator of the

machine. The orientation corresponds to the axis of the respective coils while their magnitudes change with time [41].

A construction of the space phasor of the stator current \underline{i}_S is shown in Figure 10 for assumed values of $i_{SU}, i_{SV} > 0$ and $i_{SW} < 0$.

Magnitude and angle of the space phasor vary with time according to:

$$\underline{i}_S(t) = i_S(t) \cdot e^{j\varepsilon(t)} \quad (15)$$

The stator current space phasor determines the instantaneous magnitude and angular position of the peak of the current density wave produced by the three spatially displaced stator windings.

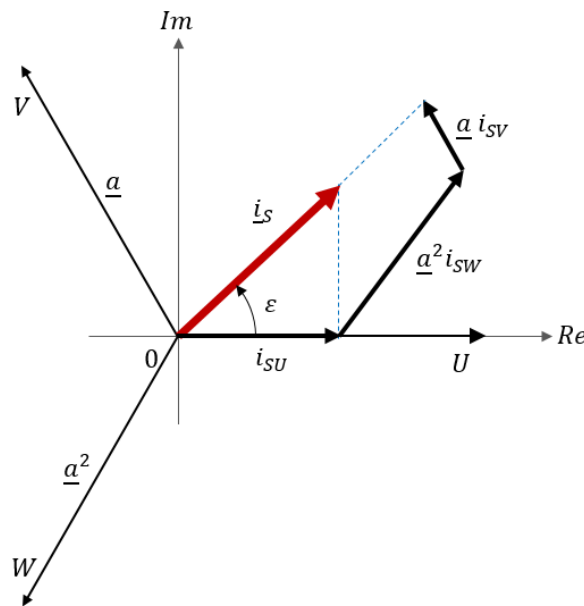


Figure 10 Graphic representation of the stator current space phasor

For balanced sinusoidal three-phase currents, the stator current space phasor has constant amplitude and its trajectory rotates with constant angular velocity in the complex plain; the resulting space phasor of the magnetic field density corresponds to

the uniformly rotating field for a normal three phase operation on a balanced sine wave supply.

However, space phasors are not restricted to sinusoidal variation in time nor to constant frequency and (13) is a general equation that defines the stator current space phasor at any instant and is valid for any stator currents, provided:

$$i_{SU} + i_{SV} + i_{SW} = 0 \quad (16)$$

As usually imposed by the connection of the windings i.e. delta or star with isolated neutral point. The current space phasor can be substituted by a superposition of the spatial distributions $i_{S\alpha}$ and $i_{S\beta}$ in a two orthogonal phase windings, thus with (13) and (16) it is possible to obtain the current components along the real and imaginary axis as:

$$i_{S\alpha} = i_{SU} \quad (17)$$

$$i_{S\beta} = \frac{1}{\sqrt{3}} \cdot (i_{SV} - i_{SW}) \quad (18)$$

In this equation $i_{S\alpha}$ and $i_{S\beta}$ can be regarded as the instantaneous currents in an equivalent two orthogonal phase windings that establish the same resultant wave as the three phase windings. From this point of view, (17) and (18) implies a three-phase to two-phase transformation of variables with the α phase of the equivalent two-phase machine coincident with the U phase of the three-phase machine.

Conversely, the instantaneous values of the phase quantities associated with the stator current space phasor are obtained from the spatial projection of \underline{i}_S on the three-phase axes.

$$i_{SU} = \text{Re}\{\underline{i}_S\} = i_{S\alpha} \quad (19)$$

$$i_{SV} = \text{Re}\{\underline{i}_S \cdot a^{-1}\} = -\frac{1}{2} \cdot i_{S\alpha} + \frac{\sqrt{3}}{2} \cdot i_{S\beta} \quad (20)$$

$$i_{SW} = \text{Re}\{\underline{i}_S \cdot a^{-2}\} = -\frac{1}{2} \cdot i_{S\alpha} - \frac{\sqrt{3}}{2} \cdot i_{S\beta} \quad (21)$$

Space phasors can be represented in an arbitrary frame of coordinates. The stator current space phasor (13) that is referred to a stator-fixed system of coordinates (α - β), can be transformed into a new reference frame (d - q), where θ is the angle between the real axis α of the fixed system and the real axis of the new system of coordinates and can vary with the time $\theta(t)$, see Figure 11.

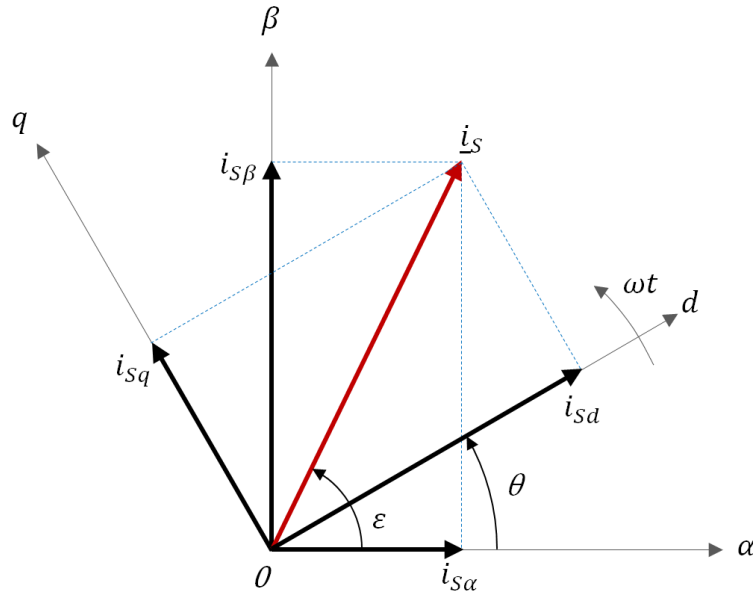


Figure 11 Transformation of a stator current space phasor from fixed α - β reference frame to d - q reference frame.

In such case, taking into account the rotation of the system, the following relations hold: $i_{S\alpha} + j \cdot i_{S\beta} = i_S \cdot e^{j\varepsilon}$ and $i_{Sd} + j \cdot i_{Sq} = i_S \cdot e^{j(\varepsilon-\theta)}$ so that, the transformation from the two-phase (α - β) reference frame to the two-phase (d - q) reference frame is as follows:

$$(i_{S\alpha} + j \cdot i_{S\beta}) = (i_{Sd} + j \cdot i_{Sq}) \cdot e^{j\theta} \quad (22)$$

and inversely

$$(i_{sd} + j \cdot i_{sq}) = (i_{s\alpha} + j \cdot i_{s\beta}) \cdot e^{-j\theta} \quad (23)$$

Comparing the real and imaginary terms in (22) and (23) the following matrix equations are obtained:

$$\begin{bmatrix} i_{s\alpha} \\ i_{s\beta} \end{bmatrix} = \begin{bmatrix} \cos(\theta) & -\sin(\theta) \\ \sin(\theta) & \cos(\theta) \end{bmatrix} \cdot \begin{bmatrix} i_{sd} \\ i_{sq} \end{bmatrix} \quad (24)$$

And the inverse transformation of (24) is calculated as:

$$\begin{bmatrix} i_{sd} \\ i_{sq} \end{bmatrix} = \begin{bmatrix} \cos(\theta) & \sin(\theta) \\ -\sin(\theta) & \cos(\theta) \end{bmatrix} \cdot \begin{bmatrix} i_{s\alpha} \\ i_{s\beta} \end{bmatrix} \quad (25)$$

As stated above, the space phasor theory is not limited to the description of three phases machines but also provides a powerful tool when applied to three phase systems in general. In the latter case, the space phasor representation is used as mathematical tool to simplify the system description and is also utilized in this work.

2.5 Permanent magnet synchronous generator model

The voltage expressions for the three-phase permanent magnet synchronous generator (PMSM) in the d - q coordinate system are well known and can be expressed as follows [42]:

$$u_{sd} = R_S i_{sd} + \frac{d\psi_d}{dt} - \omega_e \psi_q \quad (26)$$

$$u_{sq} = R_S i_{sq} + \frac{d\psi_q}{dt} + \omega_e \psi_d \quad (27)$$

where, u_{sd} and u_{sq} are the real and the imaginary component of the stator voltage space phasor in the d - q coordinate system respectively, ω_e is the electrical angular speed of the rotor and ψ_d and ψ_q are the components of the flux linkage space

phasor in the d - q coordinate system. R_S is the stator winding resistance and i_{sd} and i_{sq} are the components of the stator current space phasor in the d - q coordinate system. The flux linkages can be expressed by:

$$\psi_d = \Psi_0 + L_d i_{sd} \quad (28)$$

$$\psi_q = L_q i_{sq} \quad (29)$$

where, L_d and L_q are the d -axis and q -axis self-inductances respectively, Ψ_0 is the permanent flux produced due to the rotor-mounted permanent magnets. Thus, the stator voltages can be expressed by:

$$u_{sd} = R_S i_{sd} + L_d \frac{di_{sd}}{dt} - \omega_e L_q i_{sq} \quad (30)$$

$$u_{sq} = R_S i_{sq} + L_q \frac{di_{sq}}{dt} + \omega_e (L_d i_{sd} + \Psi_0) \quad (31)$$

The amplitude value of the stator voltage space phasor can be expressed by:

$$|u_s| = \sqrt{u_{sd}^2 + u_{sq}^2} \quad (32)$$

By substituting (30) and (31) in (32), for amplitude of the stator voltage space phasor follows:

$$|u_s| = \sqrt{\left(R_S i_{sd} + L_d \frac{di_{sd}}{dt} - \omega_e L_q i_{sq}\right)^2 + \left(R_S i_{sq} + L_q \frac{di_{sq}}{dt} + \omega_e L_d i_{sd} + \omega_e \Psi_0\right)^2} \quad (33)$$

If only the higher speed region of operation is considered, in which n_r , the rotational speed of the rotor is larger than a minimum speed (e.g. 10% of the nominal speed n_N), i.e. $n_r > 0,01 n_N$, the stator resistance voltage drop can be neglected. Moreover, $\Psi_0 \gg L_d i_{sd}$ and $\Psi_0 \gg L_q i_{sq}$ so that the stator voltage can be approximated as:

$$|u_s| \approx |\omega_e \Psi_0| \quad (34)$$

The electromagnetic torque T_e of the PMSM can be expressed by:

$$T_e = \frac{3}{2} p (\psi_0 i_{sq} + (L_d - L_q) i_{sq} i_{sd}) \quad (35)$$

where, p is the number of poles in the machine. If a magnetic isotropic rotor of the PMSG is assumed, then L_d and L_q are equal, i.e. $L_d = L_q$, then:

$$T_e = \frac{3}{2} p \Psi_0 i_{sq} \quad (36)$$

2.6 Modulation Methods for CHB

The description of the topology and the operation principle as well as the general advantage and disadvantage of the CHB were discussed in previous sections. In the following the Space Phasor Modulation (SPM) for the generation of the gate signals of the inverter is explained. In addition, the optimization of the switching sequences and the use of proper counters to reduce the switching actions are discussed. The phase shifted (PS) pulse-width modulation (PWM) technique is also presented in detail. Experimental results for both modulation techniques are presented in chapter 4 to verify both methods

2.6.1 Space Phasor Modulation (SPM)

The Space-Phasor Modulation (SPM) is a standard method for synthesizing voltages with a power inverter and has several attractive features: it is suitable for digital implementation and it offers great flexibility in the design of the switching patterns. However, the high number of possible switching states in multi-level inverters with more than three levels makes the implementation of a space vector modulation algorithm difficult. As an example: a five-level CHB converter has 6 H-bridge cells. Each cell has two legs of power switches that are controlled by two switching signals. Thus, a total of 12 PWM signals are required to generate the 125 different switching

combinations on the converter output. Hence, the SPM algorithm is associated with very high computational effort due to high number of voltage levels and of redundant switching states. Various research works [40],[44]-[50] have developed a wide range of PWM algorithms in order to reduce the computational effort. A simple realization of the SPM is performed based on the procedure presented in [40],[50].

The reference-voltage space phasor \underline{u}_{ref} delivered by the current controller is synthesized by using the three nearest-voltage space phasors \underline{u}_1 , \underline{u}_2 and \underline{u}_3 that can be delivered by the inverter and those form the vertices of the triangle in the complex $\alpha - \beta$ frame of coordinates, in which the reference-voltage space phasor is located at the moment of sampling as shown in Figure 12.

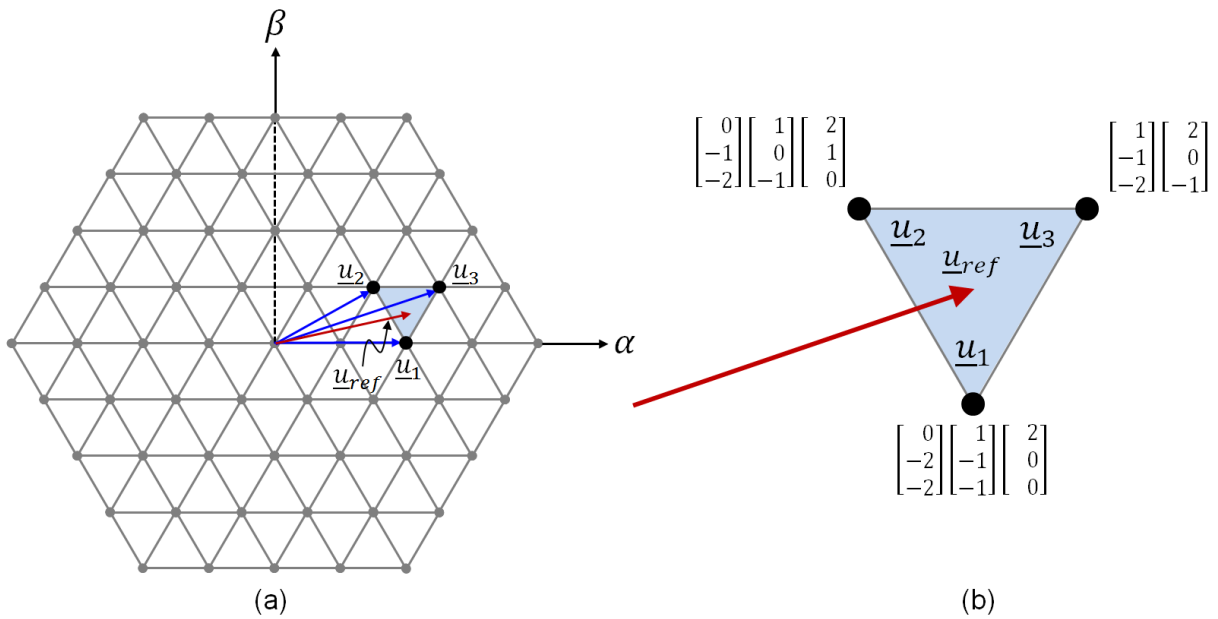


Figure 12: (a) Space phasor diagram of 5-level inverter (b) Synthesizing of the reference-voltage space phasor \underline{u}_{ref} by means of the three nearest-voltage space phasors \underline{u}_1 , \underline{u}_2 and \underline{u}_3 constitute the vertices of the shaded triangle

By assuming that for a modulation period T_s (where $T_s = 1/f_s$) and f_s is the modulation frequency), the voltage-time integral of the desired output-voltage space phasor is equal to the sum of the voltage-time integrals of the adjacent space phasors follows:

$$\underline{u}_{ref} \cdot T_s = (d_1 \cdot \underline{u}_1 + d_2 \cdot \underline{u}_2 + d_3 \cdot \underline{u}_3) \cdot T_s \quad (37)$$

being d_1 , d_2 and d_3 the duty cycles of \underline{u}_1 , \underline{u}_2 and \underline{u}_3 , respectively, must yield:

$$d_1 + d_2 + d_3 = 1. \quad (38)$$

In fact, the average value of the voltage generated by the three nearest phasors has to be equal to the average value of the reference-voltage space phasor over the sample period T_s as seen in (37). This is the basic principle for the well-known modulation techniques. In the following, the SPM algorithm for a 5-level inverter will be presented. This algorithm was optimized to ease the implementation and the computational effort.

The general algorithm of SVM for a multilevel inverter comprises four stages:

1. Identification of the three nearest-voltage space phasors (TNP) \underline{u}_1 , \underline{u}_2 and \underline{u}_3 and computation of the corresponding duty cycles d_1 , d_2 and d_3 .
2. Determination of the switching states of the TNP.
3. Generation of the switching pattern.
4. Generation of the PWM signals.

For the development of the PWM algorithm it is assumed that each phase of a 5-level inverter generates 5 discrete output voltages referred to the neutral point M of the inverter as shown in Figure 13: $-2U_{DC}$, $-U_{DC}$, 0 , $+U_{DC}$, $+2U_{DC}$.

Furthermore, a switching state $[S_U \ S_V \ S_W]$ is defined that describes the output voltage in each of the three phases as a function of the voltage U_{DC} in an easy way i.e.: $u_{UM} = S_U \cdot U_{DC}$, $u_{VM} = S_V \cdot U_{DC}$ and $u_{WM} = S_W \cdot U_{DC}$. Here S_U , S_V and S_W are integer values, which fulfill the conditions: $-2 \leq S_U, S_V \text{ and } S_W \leq 2$.

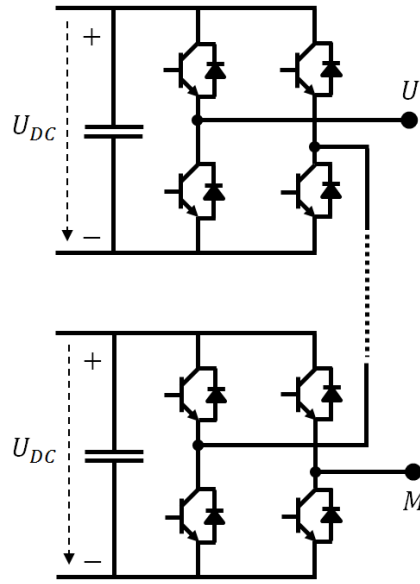


Figure 13 One phase of the 5-level CHB inverter

2.6.1.1 Identification of three nearest phasors

The three phase reference voltages $u_{ref,U}$, $u_{ref,V}$ and $u_{ref,W}$ for the three phases U, V and W are transformed to the orthogonal $\alpha - \beta$ complex plane or the stator-oriented coordinate system by using the well-known transformation:

$$\begin{bmatrix} u_{ref,\alpha} \\ u_{ref,\beta} \end{bmatrix} = \begin{bmatrix} 1 & 0 & 0 \\ 0 & \frac{\sqrt{3}}{3} & \frac{\sqrt{3}}{3} \end{bmatrix} \begin{bmatrix} u_{ref,U} \\ u_{ref,V} \\ u_{ref,W} \end{bmatrix}. \quad (39)$$

To simplify the identification of the three nearest phasors, the reference voltages $u_{ref,\alpha}$ and $u_{ref,\beta}$ are normalized with the voltage U_{DC} as a base quantity and are further transformed to an 60° oblique $\alpha' - \beta'$ coordinate system[40][50]:

$$\begin{bmatrix} u'_{ref,\alpha'} \\ u'_{ref,\beta'} \end{bmatrix} = \frac{1}{U_{DC}} \begin{bmatrix} 3/2 & -\sqrt{3}/2 \\ 0 & \sqrt{3} \end{bmatrix} \begin{bmatrix} u_{ref,\alpha} \\ u_{ref,\beta} \end{bmatrix}. \quad (40)$$

The reference-voltage space phasor \underline{u}'_{ref} in the $\alpha' - \beta'$ coordinate system is expressed as $\underline{u}'_{ref} = u'_{ref,\alpha'} + j \cdot u'_{ref,\beta'}$. Figure 14 shows the space phasors and the reference voltage in the $\alpha' - \beta'$ coordinate system. The functions *Ceil* and *Floor* are referred to

the *Nearest Integers Greater Than* and the *Nearest Integer Less Than*, e.g. $Ceil(2.4) = 3$ and $Floor(2.4) = 2$.

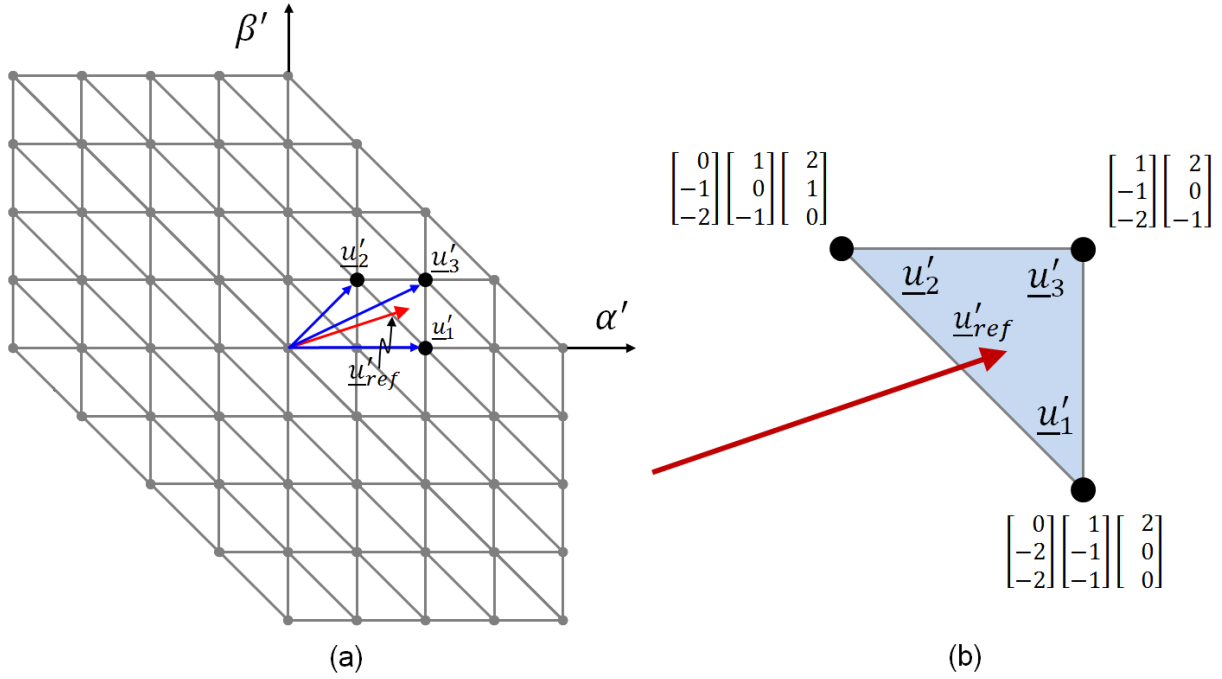


Figure 14: Linear transformation of the reference-voltage space phasor \underline{u}'_{ref} and the three nearest-voltage space phasors \underline{u}'_1 , \underline{u}'_2 and \underline{u}'_3 (a) space phasor diagram (b) zoom for the three nearest-voltage space phasors \underline{u}'_1 , \underline{u}'_2 and \underline{u}'_3 to the given reference \underline{u}'_{ref} .

Now, the three nearest phasors $\underline{u}'_1 = u'_{1,\alpha'} + j \cdot u'_{1,\beta'}$, $\underline{u}'_2 = u'_{2,\alpha'} + j \cdot u'_{2,\beta'}$ and $\underline{u}'_3 = u'_{3,\alpha'} + j \cdot u'_{3,\beta'}$ in the oblique $\alpha' - \beta'$ coordinate system can be easily identified as:

$$\begin{aligned}
 & \text{if } (u'_{ref,\alpha'} + u'_{ref,\beta'} - (Ceil(u'_{ref,\alpha'}) + Floor(u'_{ref,\beta'}))) > 0 \\
 & \quad \underline{u}'_3 = Ceil(u'_{ref,\alpha'}) + j \cdot Ceil(u'_{ref,\beta'}) \\
 & \quad \underline{u}'_2 = \underline{u}'_3 - j \\
 & \quad \underline{u}'_1 = \underline{u}'_3 - 1 \\
 & \text{else} \\
 & \quad \underline{u}'_3 = Floor(u'_{ref,\alpha'}) + j \cdot Ceil(u'_{ref,\beta'}) \\
 & \quad \underline{u}'_2 = \underline{u}'_3 + j \\
 & \quad \underline{u}'_1 = \underline{u}'_3 + 1 \\
 & \text{end}
 \end{aligned} \tag{41}$$

The advantage of these transformations is that the real and the imaginary parts of the three resulting voltage space phasors are represented as integer numbers and in this way the computation effort can be reduced.

The corresponding duty cycles of the three nearest phasors obtained from (41) can be computed as:

$$\begin{aligned}
 & \text{if } (u'_{ref,\alpha'} + u'_{ref,\beta'} - (\text{Ceil}(u'_{ref,\alpha'}) + \text{Floor}(u'_{ref,\beta'}))) > 0 \\
 & \quad d_1 = |\text{Im}(\underline{u}'_3 - \underline{u}'_{ref})| \\
 & \quad d_2 = |\text{Re}(\underline{u}'_3 - \underline{u}'_{ref})| \\
 & \quad d_3 = 1 - d_1 - d_2 \\
 & \text{else} \\
 & \quad d_1 = |\text{Re}(\underline{u}'_3 - \underline{u}'_{ref})| \\
 & \quad d_2 = |\text{Im}(\underline{u}'_3 - \underline{u}'_{ref})| \\
 & \quad d_3 = 1 - d_1 - d_2 \\
 & \text{end}
 \end{aligned} \tag{42}$$

The general expression for the nearest-voltage space phasors \underline{u}'_1 , \underline{u}'_2 and \underline{u}'_3 is given as $\underline{u}'_i = u'_{i,\alpha'} + j \cdot u'_{i,\beta'}$ ($i = 1, 2, 3$) and their components $u'_{i,\alpha'}$ and $u'_{i,\beta'}$ are integer numbers and dimensionless.

2.6.1.2 Determination of switching states of three nearest phasors

The switching states $[S_{i,U} \ S_{i,V} \ S_{i,W}]$ of a particular voltage space phasor \underline{u}'_i ($i = 1, 2, 3$) of the three nearest phasors yield following relationship:

$$\begin{aligned}
 S_{i,U} &= u'_{i,\alpha'} + u'_{i,\beta'} + c_i \\
 S_{i,V} &= \quad \quad \quad u'_{i,\beta'} + c_i \\
 S_{i,W} &= \quad \quad \quad \quad \quad c_i
 \end{aligned} \tag{43}$$

In fact the difference between the redundant switching states of a given voltage space phasor is the common-mode voltage, thus the integer c_i in (43) is needed that represents the common mode part of a particular switching state $[S_{i,U} \ S_{i,V} \ S_{i,W}]$ and offers a degree of freedom. Consider the TNP in the Figure 12 (b) as an example. The

redundant space phasors are determined. The space phasors \underline{u}_1 , \underline{u}_2 have three redundant states while \underline{u}_3 has two redundant states. The common-mode voltage for each space phasor is calculated as shown in the switching matrix in Figure 15 by adding all the voltages of the corresponding state.

$$\begin{array}{r}
 \begin{array}{c} \underline{u}_1 \qquad \qquad \qquad \underline{u}_2 \qquad \qquad \qquad \underline{u}_3 \\
 u_U \rightarrow \left[\begin{array}{c} 0 \\ -2 \\ -2 \end{array} \right] \left[\begin{array}{c} 1 \\ -1 \\ -1 \end{array} \right] \left[\begin{array}{c} 2 \\ 0 \\ 0 \end{array} \right] \left[\begin{array}{c} 0 \\ -1 \\ -2 \end{array} \right] \left[\begin{array}{c} 1 \\ 0 \\ -1 \end{array} \right] \left[\begin{array}{c} 2 \\ 1 \\ 0 \end{array} \right] \left[\begin{array}{c} 1 \\ -1 \\ -2 \end{array} \right] \left[\begin{array}{c} 2 \\ 0 \\ -1 \end{array} \right] \\
 u_V \rightarrow \left[\begin{array}{c} 0 \\ -2 \\ -2 \end{array} \right] \left[\begin{array}{c} 1 \\ -1 \\ -1 \end{array} \right] \left[\begin{array}{c} 2 \\ 0 \\ 0 \end{array} \right] \left[\begin{array}{c} 0 \\ -1 \\ -2 \end{array} \right] \left[\begin{array}{c} 1 \\ 0 \\ -1 \end{array} \right] \left[\begin{array}{c} 2 \\ 1 \\ 0 \end{array} \right] \left[\begin{array}{c} 1 \\ -1 \\ -2 \end{array} \right] \left[\begin{array}{c} 2 \\ 0 \\ -1 \end{array} \right] \\
 u_W \rightarrow \left[\begin{array}{c} 0 \\ -2 \\ -2 \end{array} \right] \left[\begin{array}{c} 1 \\ -1 \\ -1 \end{array} \right] \left[\begin{array}{c} 2 \\ 0 \\ 0 \end{array} \right] \left[\begin{array}{c} 0 \\ -1 \\ -2 \end{array} \right] \left[\begin{array}{c} 1 \\ 0 \\ -1 \end{array} \right] \left[\begin{array}{c} 2 \\ 1 \\ 0 \end{array} \right] \left[\begin{array}{c} 1 \\ -1 \\ -2 \end{array} \right] \left[\begin{array}{c} 2 \\ 0 \\ -1 \end{array} \right] \\
 \text{common - mode voltage} \rightarrow -4 \quad -1 \quad 2 \quad -3 \quad 0 \quad 3 \quad -2 \quad 1
 \end{array}
 \end{array}$$

Figure 15: Switching Matrix of the TNP to the reference-voltage space phasor \underline{u}_{ref}

2.6.1.3 Choice of the proper switching sequence

Once the determination of the three nearest-phasors (TNP), of the corresponding duty cycles and of the switching states has been accomplished as explained in the previous section, the next step for the realization of the SPM is the generation of the switching sequence (switching pattern), which is required prior to the generation of the PWM signals at hardware level.

The placement of switching states has to be examined carefully in order to achieve minimal switching losses. For this purpose, the switching states found according to the procedure explained above are arranged in a switching matrix in such way that each switching state $[S_{i,U} \ S_{i,V} \ S_{i,W}]$ of the voltage space phasor $\underline{u}_{i,\alpha'\beta'}$ ($i = 1, 2$ or 3) builds a column of a matrix. The columns are ordered from left to right for an increasing value of the common-mode voltage of each state $u_{CMV} = \frac{1}{3}(S_{i,U} + S_{i,V} + S_{i,W})$. In such an arrangement the transit between two adjacent switching states demands only one switching action. Figure 16 (a) shows the arrangement of the switching states $[S_{i,U} \ S_{i,V} \ S_{i,W}]$ of the TNP in a switching matrix according to the minimum common – mode voltage.

$$\begin{array}{r}
 \begin{array}{cccccccc}
 \underline{u}_1 & \underline{u}_2 & \underline{u}_3 & \underline{u}_1 & \underline{u}_2 & \underline{u}_3 & \underline{u}_1 & \underline{u}_2 \\
 u_U \rightarrow & \begin{bmatrix} 0 \\ -2 \\ -2 \end{bmatrix} & \begin{bmatrix} 0 \\ -1 \\ -2 \end{bmatrix} & \begin{bmatrix} 1 \\ -1 \\ -2 \end{bmatrix} & \begin{bmatrix} 1 \\ -1 \\ -1 \end{bmatrix} & \begin{bmatrix} 1 \\ 0 \\ -1 \end{bmatrix} & \begin{bmatrix} 2 \\ 0 \\ -1 \end{bmatrix} & \begin{bmatrix} 2 \\ 0 \\ 0 \end{bmatrix} \\
 u_V \rightarrow & & & & & & & \\
 u_W \rightarrow & & & & & & & \\
 \text{common - mode voltage} \rightarrow & -4 & -3 & -2 & -1 & 0 & 1 & 2 & 3
 \end{array}
 \end{array}$$

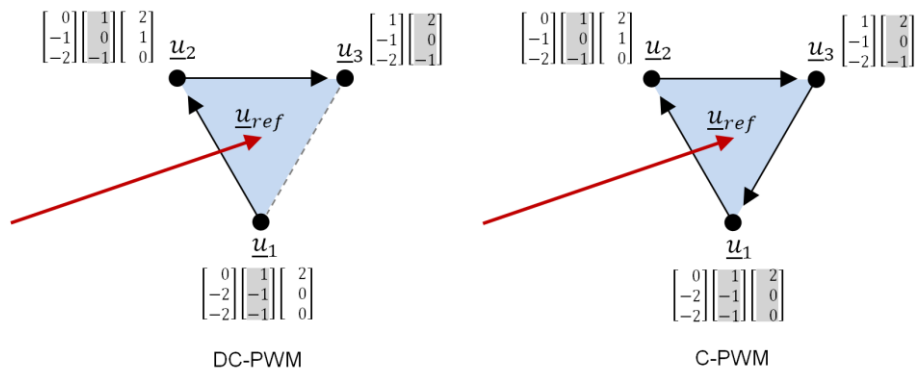
(a) Arrangement of the switching states $[S_{i,U} S_{i,V} S_{i,W}]$ of the TNP in a switching matrix according to the minimum common – mode voltage

$$\begin{array}{r}
 \begin{array}{cccccccc}
 \underline{u}_1 & \underline{u}_2 & \underline{u}_3 & \underline{u}_1 & \underline{u}_2 & \underline{u}_3 & \underline{u}_1 & \underline{u}_2 \\
 u_U \rightarrow & \begin{bmatrix} 0 \\ -2 \\ -2 \end{bmatrix} & \begin{bmatrix} 0 \\ -1 \\ -2 \end{bmatrix} & \begin{bmatrix} 1 \\ -1 \\ -2 \end{bmatrix} & \begin{bmatrix} 1 \\ -1 \\ -1 \end{bmatrix} & \begin{bmatrix} 1 \\ 0 \\ -1 \end{bmatrix} & \begin{bmatrix} 2 \\ 0 \\ -1 \end{bmatrix} & \begin{bmatrix} 2 \\ 0 \\ 0 \end{bmatrix} \\
 u_V \rightarrow & & & & & & & \\
 u_W \rightarrow & & & & & & & \\
 \text{common - mode voltage} \rightarrow & -4 & -3 & -2 & \underline{-1} & \underline{0} & \underline{1} & 2 & 3
 \end{array}
 \end{array}$$

(b) Three adjacent switching states in DC-PWM

$$\begin{array}{r}
 \begin{array}{cccccccc}
 \underline{u}_1 & \underline{u}_2 & \underline{u}_3 & \underline{u}_1 & \underline{u}_2 & \underline{u}_3 & \underline{u}_1 & \underline{u}_2 \\
 u_U \rightarrow & \begin{bmatrix} 0 \\ -2 \\ -2 \end{bmatrix} & \begin{bmatrix} 0 \\ -1 \\ -2 \end{bmatrix} & \begin{bmatrix} 1 \\ -1 \\ -2 \end{bmatrix} & \begin{bmatrix} 1 \\ -1 \\ -1 \end{bmatrix} & \begin{bmatrix} 1 \\ 0 \\ -1 \end{bmatrix} & \begin{bmatrix} 2 \\ 0 \\ -1 \end{bmatrix} & \begin{bmatrix} 2 \\ 0 \\ 0 \end{bmatrix} \\
 u_V \rightarrow & & & & & & & \\
 u_W \rightarrow & & & & & & & \\
 \text{common - mode voltage} \rightarrow & -4 & -3 & -2 & \underline{-1} & \underline{0} & \underline{1} & \underline{2} & 3
 \end{array}
 \end{array}$$

(c) Four adjacent switching states in C-PWM



(d) Switching sequence in space phasor representation for both C-PWM and DC-PWM

Figure 16: Arrangement of the switching states of the TNP in a switching matrix and space

phasor representation of the switching sequence

In general, two types of sequences are normally used differing in the number of states used in each modulation period: the so called *discontinuous* PWM (DC-PWM) and the *continuous* PWM (C-PWM) [40]. In case of DC-PWM, switching sequence is a set of three consecutive switching states of the TNP that together with their corresponding duty cycles are used for the generation of the switching signals or commands for the inverter. Within the selected three TNP, two of the phases exhibit a switching action per modulation period, while the remaining phase exhibits no switching actions and therefore its output voltage is kept constant. Figure 16 (b) shows the selected three switching states with minimum common-mode voltage in the case of DC-PWM (the adjacent shaded phasors), the sequence $[0 \ -1 \ -1]^T$, $[1 \ 0 \ -1]^T$, $[2 \ 0 \ -1]^T$ exhibits only one switching action per state transition whereas the voltage in the last phase is kept constant during the modulation period. In the case of C-PWM, each phase exhibits a switching action per modulation period. This can be achieved by using a fourth voltage state which must be redundant to the first one of the sequence as depicted in Figure 16 (c), where the adjacent shaded phasor is the selected phasor with minimum common-mode voltage. The sequence $[0 \ -1 \ -1]^T$, $[1 \ 0 \ -1]^T$, $[2 \ 0 \ -1]^T$, $[2 \ 0 \ 0]^T$ exhibits only one switching action per state transition. Figure 16 (d) shows the switching sequence in space phasor representation for both C-PWM and DC-PWM.

2.6.1.4 Generation of PWM signals

The redundancy of the voltage space phasors provides different possibilities to build the same line-to-line voltage. The redundancy can be used for diverse control purposes: redistribution of losses among the phases, reduction of common-mode voltage, operation under fault conditions (fault tolerant control) etc. After the proper selection of the states in the previous step was carried out, the realization of the voltage space phasors by the inverter follows. Figure 17 (a) shows the possible switching combinations to connect e.g. phase U of the 5L-CHB inverter to a certain potential and the terms S_{11} , S_{12} , S_{21} and S_{22} of this table refer to the gate signals of phase U that are depicted in Figure 17 (b). There is only one possibility to generate

the phase output $u_{UM} = +2U_{DC}$ or $u_{UM} = -2U_{DC}$ but there are four possibilities to connect the phase U to the potential $+1U_{DC}$, four possibilities to connect it to the $-1U_{DC}$ and four possibilities to connect it to the $0U_{DC}$. These possibilities can be referred to redundancy of phase connection, which affects the losses of the switches within a phase.

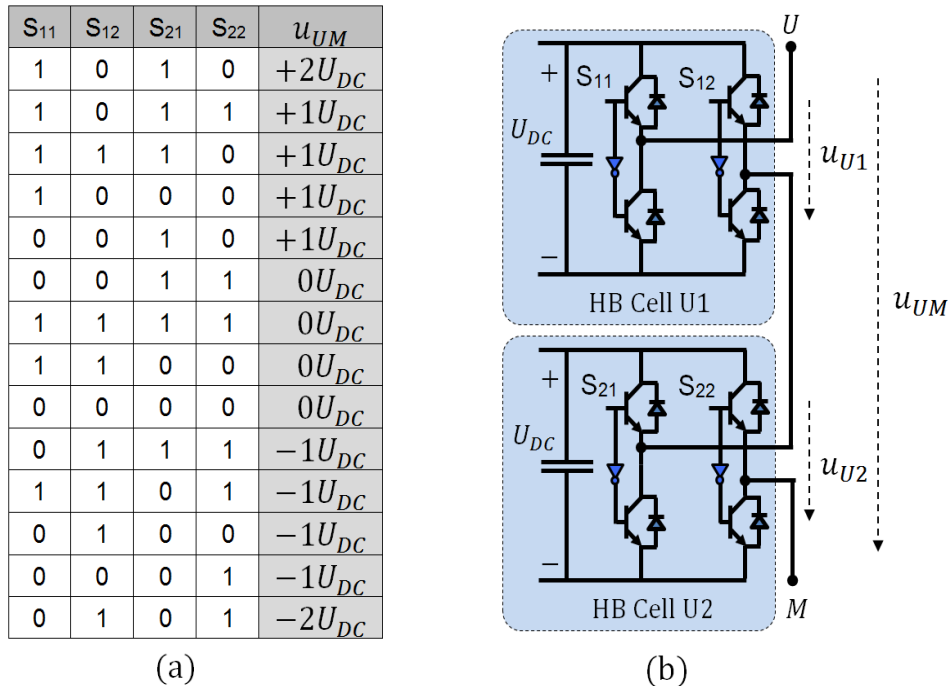


Figure 17 (a) Possible switching state combinations of one phase (b) Phase U of a 5-level CHB inverter

In the current work, a state machine as shown in Figure 18 is employed to choose the proper phase redundancy and to ensure the even distribution of losses among the switches of the inverter, so that the design of the cooling system is simplified. Furthermore, the life time and the reliability of the system are consequently increased. Each state of the state machine corresponds to one of the states described in Figure 17 (a). By following the path in Figure 18 (a) it is clear that the transition among the different voltage levels does not lead to repeat the same switching combination in the next period of the modulation and it is obtained by only one switching action. For example, the shaded part of the output phase voltage depicted in Figure 18 (b) started at level $+2U_{DC}$ and ended at level $-2U_{DC}$, Figure 18 (c) show the switching transition

sequence path depending on the criteria depicted in Figure 18 (a). The outputs of the state machine are sent the counter to generate the gate signals.

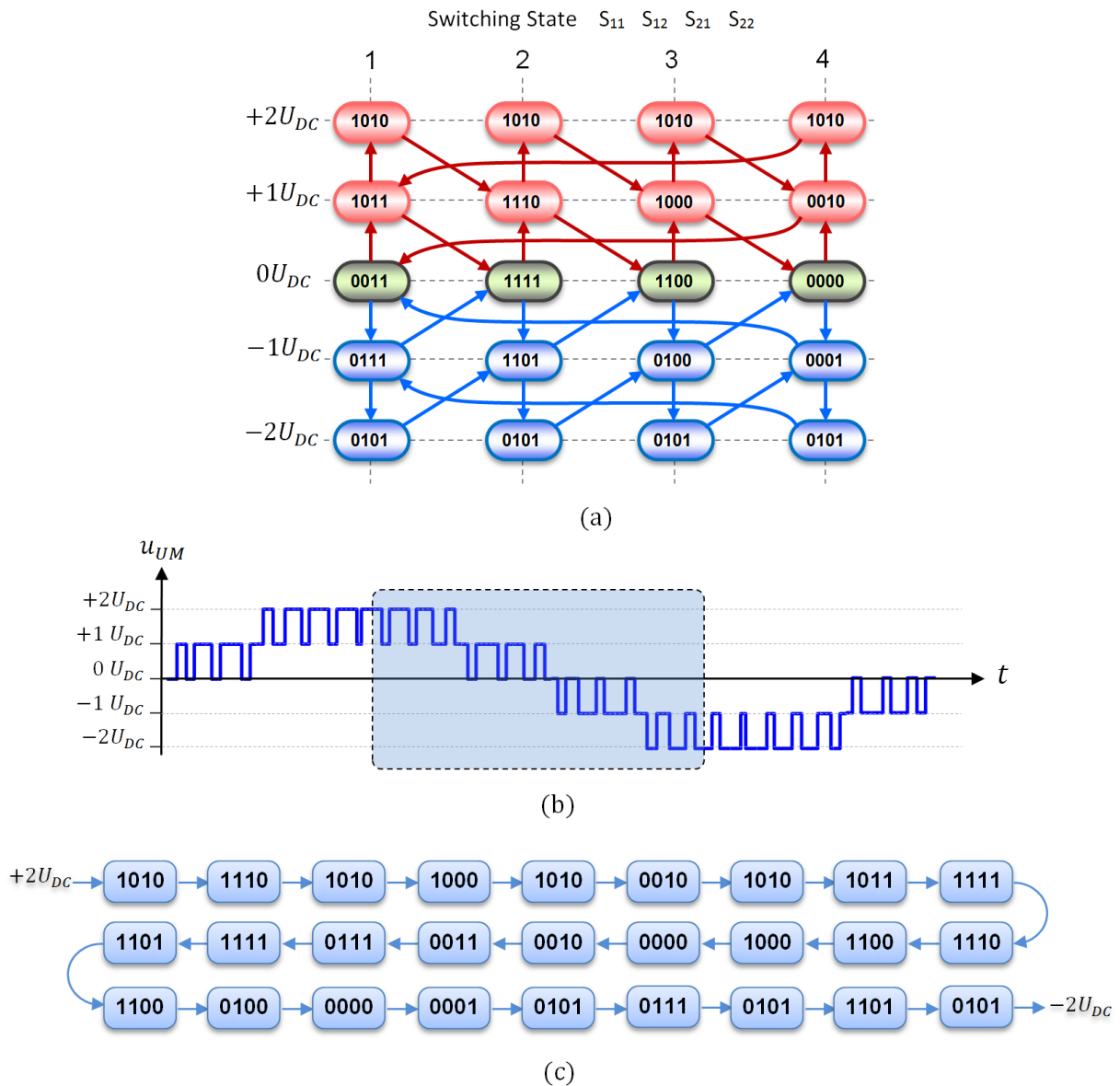
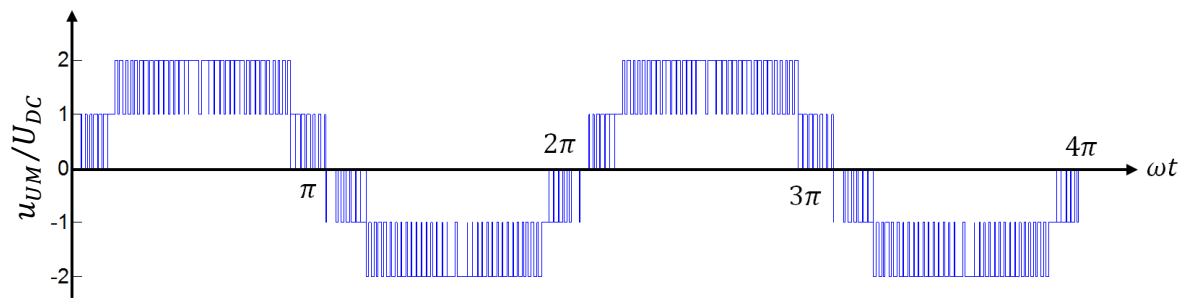
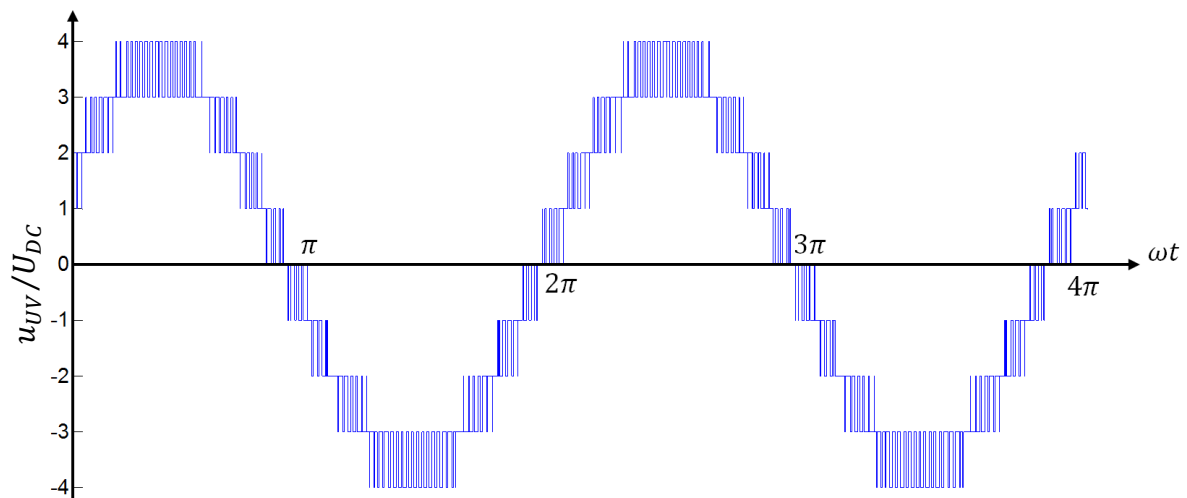


Figure 18 State machine technique: (a) state machine for phase U of the inverter (b) inverter phase voltage (c) switching sequence of the shaded part of the phase voltage depicted in (b)

Figure 19 shows the output voltage of the inverter at the normal switching frequency (5 kHz) and for modulation index $m = 0,9$.



(a) Phase voltage



(b) Line voltage

Figure 19 Inverter output voltage with 5kHz switching frequency at 0,9 modulation index

2.6.2 Phase-shifted sinusoidal pulse width modulation (PS-PWM)

Phase-Shifted PWM (PS-PWM) is the standard modulation method for the commercial CHB multilevel inverter due to simple implementation [40]. This is a natural extension of traditional PWM techniques and is based on the unipolar PWM for single phase H-bridge inverters, since each HB cell generates three output voltage levels. Because of the modularity of CHB topology, each cell can be modulated independently using the same reference signal (or different amplitude reference signals at the same phase as we will see in the next chapter). A phase shift is added among the carrier signals of adjacent cells of one phase to producing a phase-shifted switching pattern. This results

in a stepped multilevel waveform at the output of each phase. To achieve the best switching performance, the phase shift ϕ_y is specified as:

$$\phi_y = \frac{180^\circ}{n_{cell}} \quad (44)$$

where n_{cell} is the number of cells of one phase and in case of 5L-CHB inverter $n_{cell} = 2$. By using PS-PWM technique, the losses are evenly distributed among the switching devices. Figure 20 show the operation principle includes the control circuit diagram of the PS-PWM for two cells of one phase of the inverter as well as the switch pattern S_{11} , S_{12} generated by unipolar PWM for one cell and cell output voltage u_{U1} .

Figure 21 shows the phase shift between the carrier of two different cells in the same phase, the corresponding cell voltage u_{U1} and u_{U2} , the output phase voltage u_{UM} and the output line to line voltage u_{UV} , in which a double step voltage is marked with a red circle. The double step voltage can be reduced by adding a phase shift to the carrier signals among the phases:

$$\phi_x = \frac{\phi_y}{n_{cell}} \quad (45)$$

In this way, the number of double steps in the line-to-line voltage waveform is reduced improving the quality of the output voltage waveform.

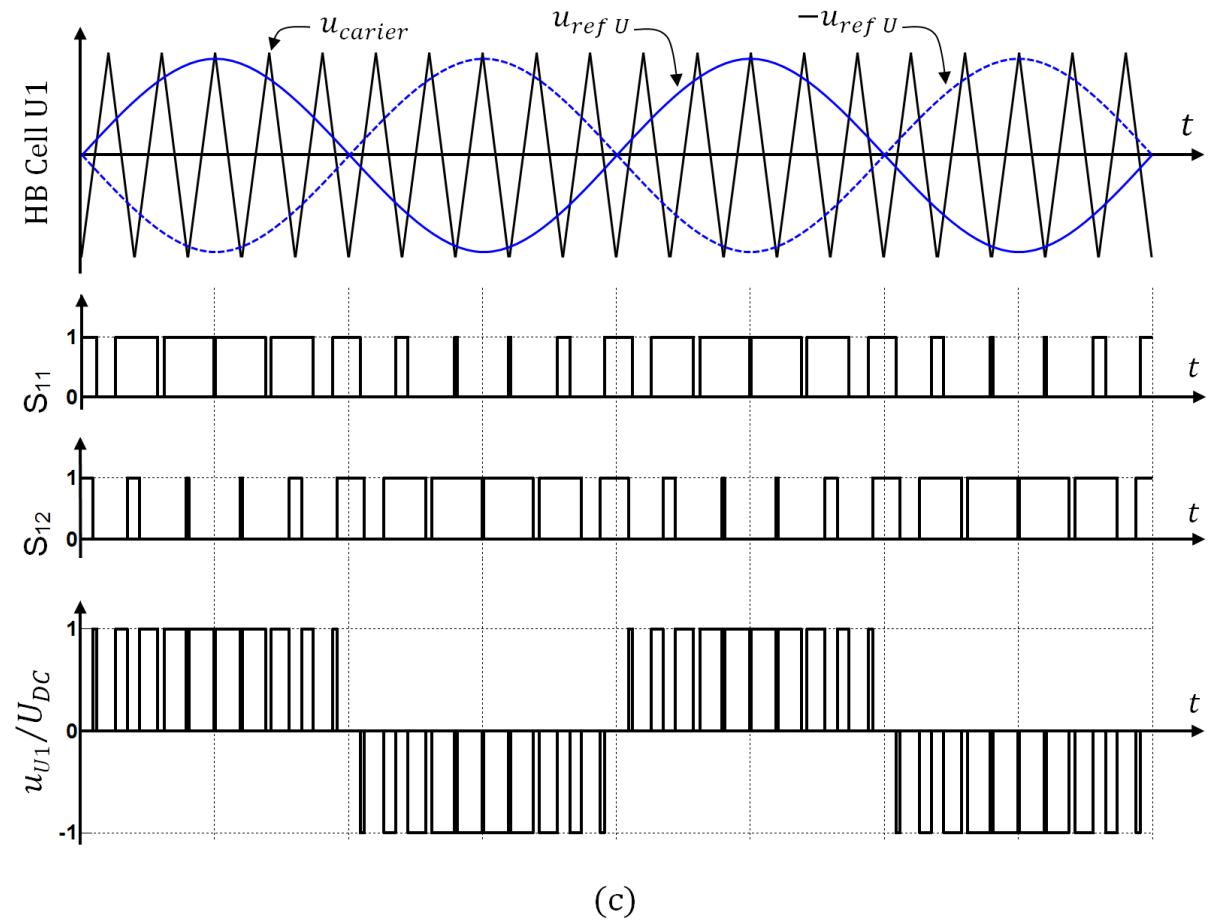
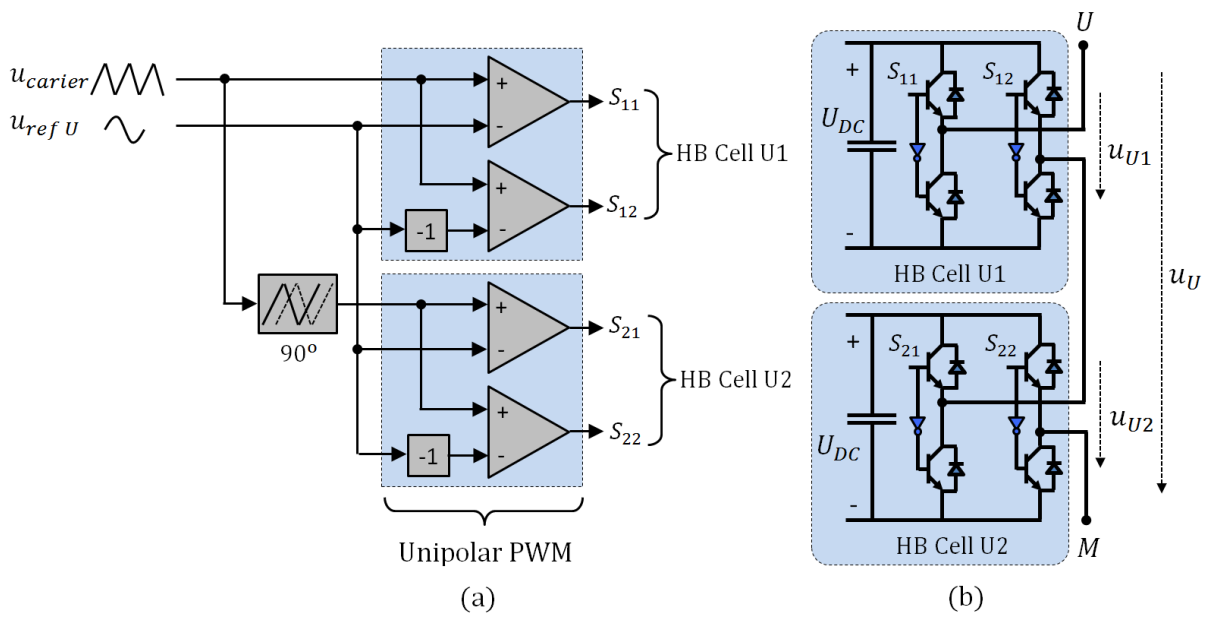


Figure 20 (a) Two-cell (five level) PS-PWM control diagram for CHB (b) Phase U of 5-Level CHB inverter (c) Switch patron generated by unipolar PWM and cell output voltage u_{U1}

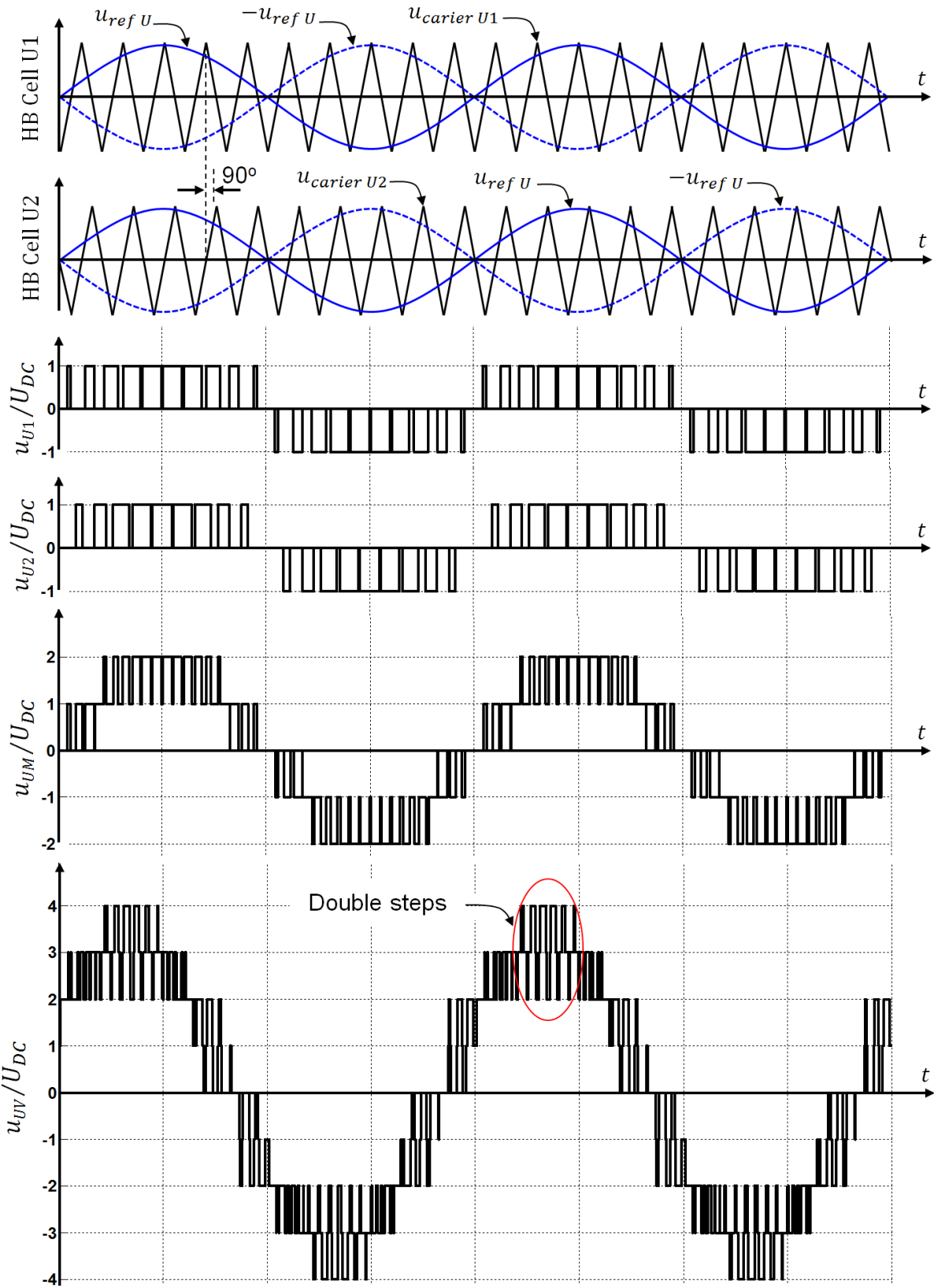


Figure 21 Cell, phase and line voltage of the CHB inverter 5-level using PS-PWM

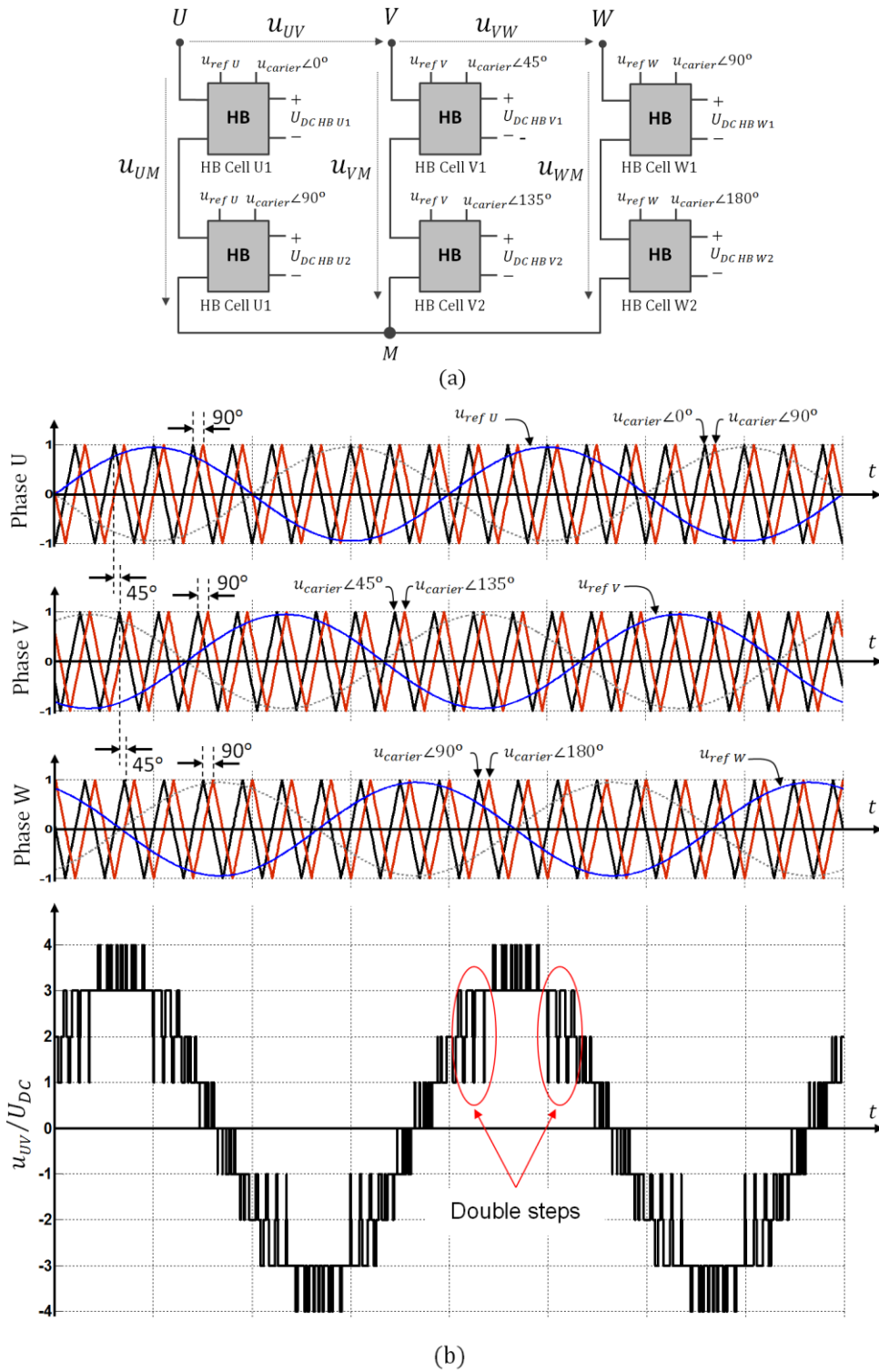


Figure 22 Five level CHB multilevel inverter (a) Block diagram of a 5-level inverter with the corresponding phase shift for the carriers (b) the references voltages and carrier signals for a PS-PWM and the equivalent line voltage

2.6.3 Phase-shifted sinusoidal pulse width modulation with zero sequence signal injection

In the conventional sinusoidal PWM, the range of modulation index is ($0 \leq m \leq 1$), In case of ($m > 1$), the inverter works in the over-modulation region which causes higher harmonics at the output voltage. The utilization of DC-link can be improved, if a zero sequence signal is added to the reference signals [34][35]. Figure 23 shows the block diagram of this technique. Clearly, the addition of the zero sequence reduces the amplitude of the resulting modified reference signals ($u_{ref U}^z, u_{ref V}^z$ and $u_{ref W}^z$), while the fundamental components remain unchanged. This approach expands the range of the linear region as it allows the use of modulation indexes m up to $2/\sqrt{3} \approx 1,155$ without getting into the over modulation region. The zero sequence voltage (or minimum-maximum voltage) $u_{min-max}$ is obtained using the following expression:

$$u_{min-max} = \frac{\max\{u_{ref U}, u_{ref V}, u_{ref W}\}}{2} + \frac{\min\{u_{ref U}, u_{ref V}, u_{ref W}\}}{2} \quad (46)$$

In which the “*max*” function returns the maximum value of the three reference voltages $u_{ref U}, u_{ref V}$ and $u_{ref W}$ and the “*min*” function returns the minimum value of those references.

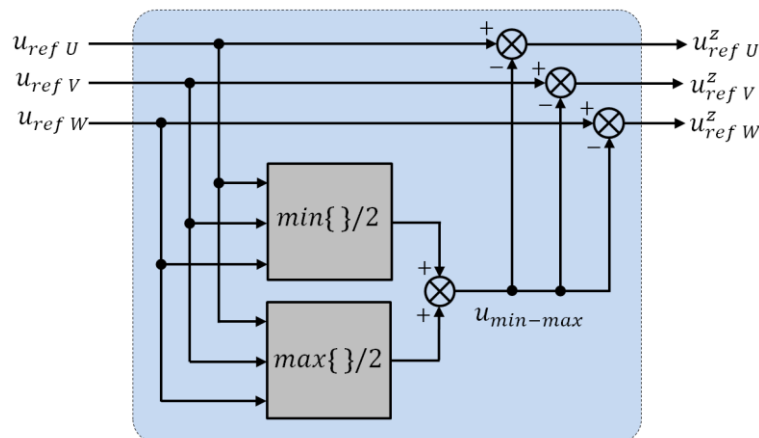


Figure 23 Zero sequence signal addition

Now the modified reference signals are:

$$u_{ref U}^z = u_{ref U} - u_{min-max} \quad (47)$$

$$u_{ref V}^z = u_{ref V} - u_{min-max} \quad (48)$$

$$u_{ref W}^z = u_{ref W} - u_{min-max} \quad (49)$$

Figure 24 shows the ideal reference signal waveform of three phase inverter before (a) and after (b) adding zero sequence signal injected for ($m = 1$) and Figure 24 (d) shows the inverter line voltage corresponding to the references with zero sequence. It can be seen that the double step voltage in the line voltage is reduced more after use of the zero sequence.

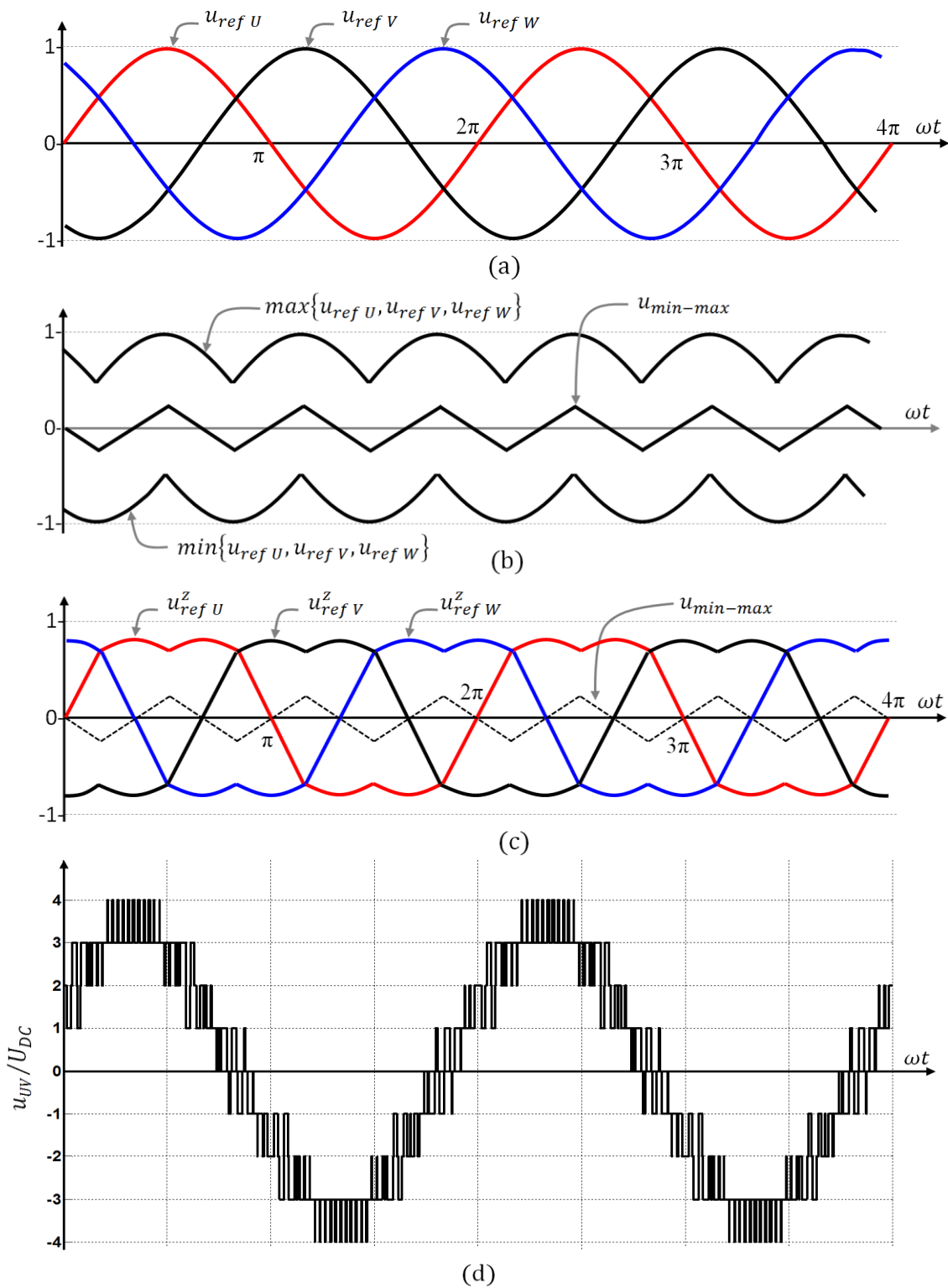


Figure 24 Phase-shifted SPWM with zero sequence signal injection (a) reference signals (b) minimum-maximum sequence with zero sequence signal (c) modified reference signals (d) inverter line voltage

3 Cascaded H-Bridge converter for the grid connection of hybrid systems

As stated at the beginning of the thesis, the scope of this work was defined as the examination of a grid connection of hybrid PV-Wind generation systems by using a cascaded H-bridge converter. In the following, the complete system is comprehensively described and analyzed with all its characteristics and features.

3.1 System Topology

The topology presented in [14] is modified here by connecting three PV sources to the DC-links of the upper level H-bridges and by replacing the PV multi string DC bus from the lower level H-bridges by DC-links fed by PMS generators which are coupled to corresponding wind turbines. Figure 25 shows the proposed cascaded H-bridge voltage source inverter for the hybrid PV-wind system. As shown in the figure, the PV sources as well as the wind generators are connected to the DC-links of the H-bridges directly without DC-DC-converters in order to improve the system reliability and to reduce the number of components as well as the complexity of the control. In addition, the utilization of a CHB allows to have an independent MPPT algorithm for each power cell of the converter.

The power system that is considered in this work is depicted in Figure 25 and consists of five main parts: The H-bridges of the CHB with their respective DC-links, the PV strings that feed the upper DC-links, the permanent magnet synchronous generators driven by the wind turbines together with the rectifiers to feed the DC-links, the grid connection with an inductive filter and the optional isolation transformer. The CHB converter consists of identical, series connected H-bridge cells. Each cell can generate three output voltage levels. The series connection of the cells generates the output voltage in all three phases by using SPM or PS-PWM to generate the three phase output voltage.

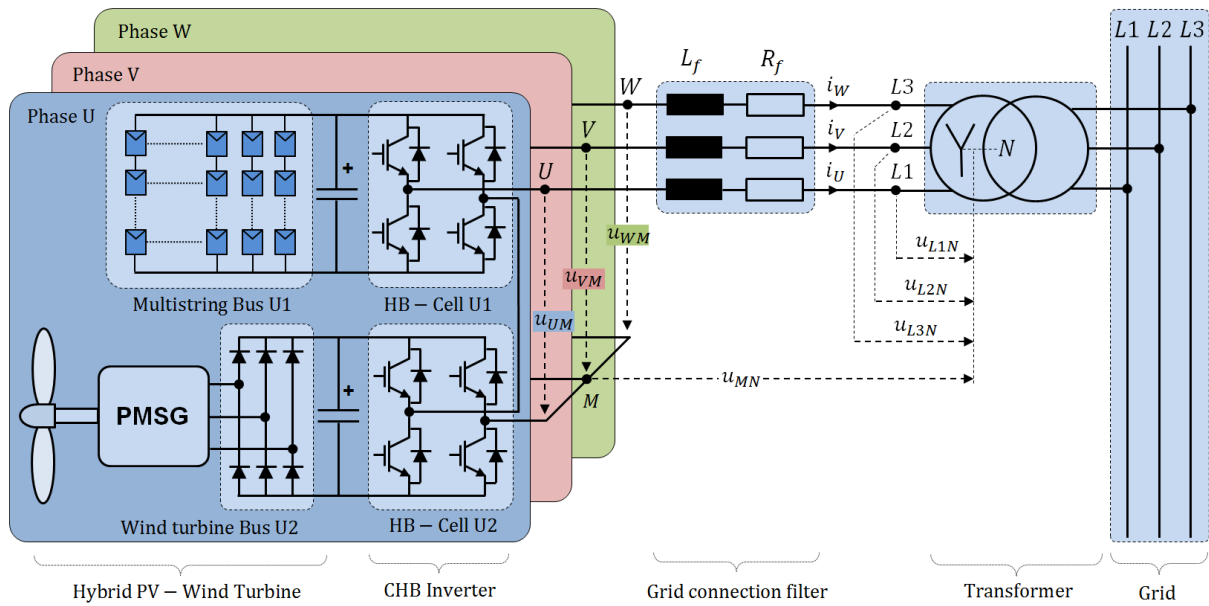


Figure 25 Hybrid energy grid integration system

In general, when n_{cell} H-bridges are connected in series, the output voltages referred to the neutral point in each of the three phases can take $n_L = 2n_{cell} + 1$ levels, if assuming equal dc-link voltages in the cells. Hence, in the used topology with two cascaded H-bridges per phase, the converter can generate five different voltage levels of the phase voltage. An inductive filter is used for the connection of the converter to the grid and a transformer is optionally used for isolation issues.

3.2 Operation modes of the hybrid generation system

The idea behind the use of a CHB inverter for the hybrid PV-Wind system is to achieve an operation of the generation system and its grid integration during the day, when PV- and possibly wind power is transferred to the grid, as well as during the night, when no PV-power is transferred to the grid. For this purpose a single inverter without any additional power electronic components is utilized. In addition, a control scheme is proposed which can manage the different modes of operation without any changes in the hardware and that can be implemented in a single processing unit like digital signal processor. As it is discussed in the following, the inverter has to be designed to handle the power in the operation mode with maximum power generation,

i.e. the rated power of the PV as well as of the WT generators. For a better understanding a single phase hybrid PV-WT grid connection system as shown in Figure 26 is analyzed.

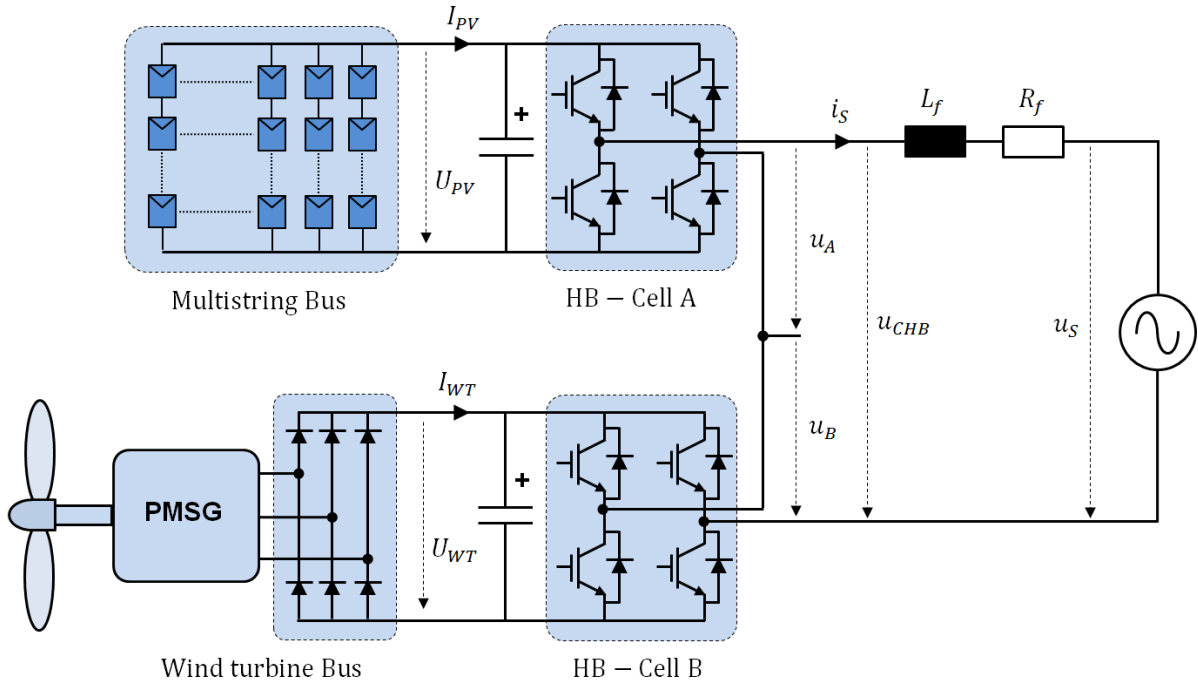


Figure 26 Single phase hybrid PV-Wind grid connection system using 5L-CHB inverter

3.2.1 Operation of the wind generation sub-system

According to (30) and (31), the terminal voltages of each generator will be in good approximation proportional to its rotational speed as:

$$|\underline{u}_S| \approx \omega_e \Psi_0 \quad (50)$$

where $|\underline{u}_S|$ is the absolute value of the stator voltage space phasor, ω_e is the electrical angular speed of the rotor, while Ψ_0 is the amplitude of the flux linkage space phasor produced by the rotor-mounted permanent magnets, which is nearly constant in PMSG.

Each generator is connected to a three phase diode rectifier with a capacitor filter. By supposing that the rectifier is ideal, the DC-link voltage U_{WT} of the wind generator bus on each HB will consequently also be directly proportional to the turbine speed ω_m . Therefore, the power vs. speed characteristics of a wind turbine can be translated to power vs. voltage curves. Without loss of generality Figure 27 show as an example the power vs. voltage characteristics of a wind turbine for different wind speeds that was used as base for the present investigation.

In a period of 24 hours the wind speed is not constant and may vary between zero and the rated value or more. In Figure 27 the red curve describes the possible maximum wind power which can be obtained depending on the DC-link voltage. It is obvious, that the system works in the maximum power point mode for wind speeds between $v_{w,(cut-in)} \leq v_w \leq v_{w,(rated)}$ which is from 40% to 100% of the rated value. The DC-link of the wind generator bus voltage will accordingly deliver voltages in the range of $U_{WT,(min)} \leq U_{WT} \leq U_{WT,(rated)}$ which is between 40% and 100% of the rated voltage. Thus, it is evident, that the wide range of the wind speed leads to a wide range of voltages in the DC-links of the inverters. Accordingly the power produced by the WT generator varies in the range of $P_{WT,(min)} \leq P_{WT} \leq P_{WT,(rated)}$.

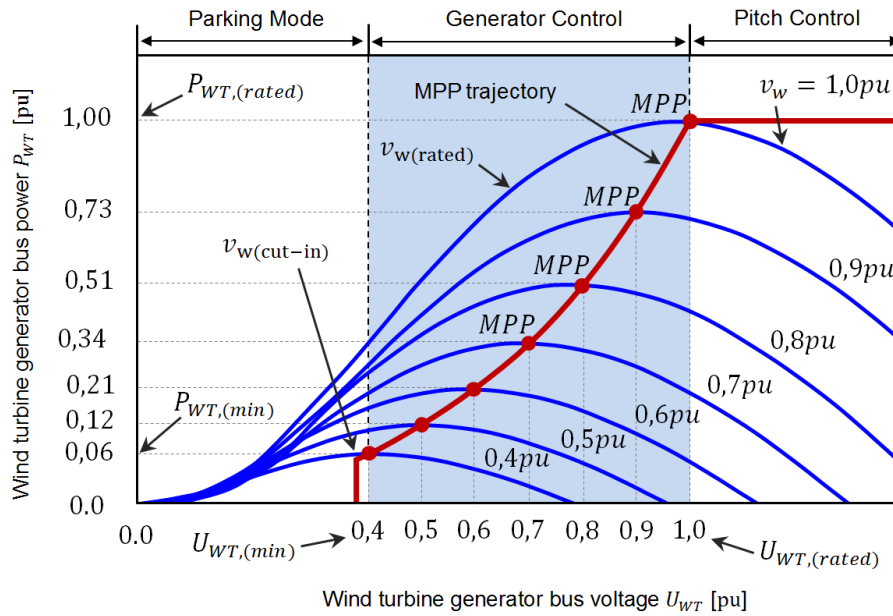


Figure 27 Power vs. voltage characteristics of a wind turbine for different wind speeds

3.2.2 Operation of the solar generation sub-system

In the case of the solar generator the situation is different. If all temperature effects are first neglected and only a wide range of sun irradiance is considered, the voltage at the outputs of the PV strings will only slightly change. The effect of the sun irradiance on the voltage is low compared to the impact of the wind speed in the case before. Again, without the loss of generality these relationships are illustrated for a concrete case depicted in Figure 28, in which the sun irradiance S_{IR} varies in the range $S_{IR,(min)} \leq S_{IR} \leq S_{IR,(rated)}$ which is from 10% to 100% of the rated value. However, the PV string bus voltages U_{PV} in the maximum power point only varies in the range of $U_{PV,(min)} \leq U_{PV} \leq U_{PV,(rated)}$ which is between 90% and 100% of the rated voltage while the power produced by the PV generator varies in the range of $P_{PV,(min)} \leq P_{PV} \leq P_{PV,(rated)}$.

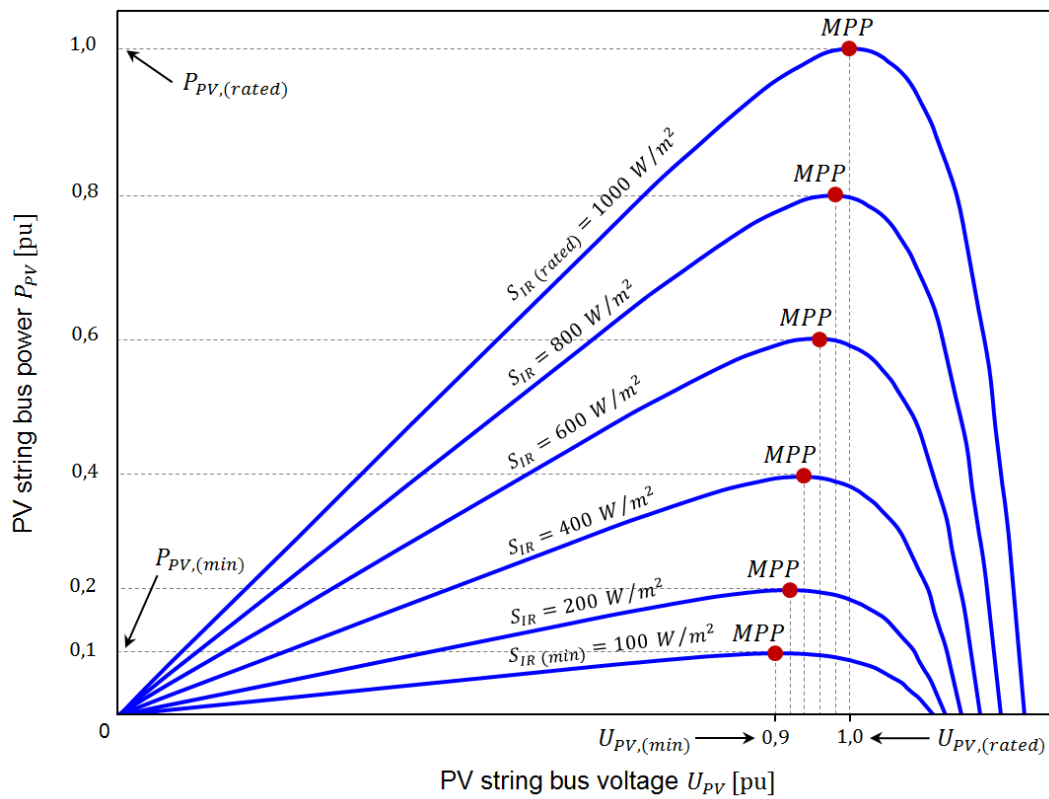


Figure 28 Solar panel power vs. voltage characteristics for different values of sun irradiance

3.2.3 Hybrid operation of wind turbine and PV cells

For the better understanding of the hybrid operation of the converter, it is assumed that the wind turbine generator and PV-panels are designed in a way, that under rated conditions (rated sun irradiance $S_{IR,(rated)}$ and rated wind speed $v_{w,(rated)}$) the rated power produced by each generator is equal ($P_{PV,rated} = P_{WT,rated}$).

The rated DC-link voltages of both generator busses can be selected freely by adjusting either the winding of the permanent magnet synchronous generator or by choosing the proper amount of series connected PV-panels. But the question is how to choose the proper value of the rated DC-link voltages to prevent massive oversizing on the one hand and to allow the injection of power to the grid in the partial load region on the other hand. In order to answer this question, two quantities k_{WT} and k_{PV} are introduced which help to describe the behavior of the system in the partial load region:

$$k_{WT} = \frac{U_{WT,(min)}}{U_{WT,(rated)}} \quad (51)$$

$$k_{PV} = \frac{U_{PV,(min)}}{U_{PV,(rated)}} \quad (52)$$

where k_{WT} is the ratio between the minimum DC-link voltage $U_{WT,(min)}$ (at $v_{w,(cut-in)}$) of the WT generator bus and the rated voltage $U_{WT,(rated)}$ (at $v_{w,(rated)}$). In the same manner, k_{PV} is defined as the ratio between the minimum DC-link voltage $U_{PV,(min)}$ at $S_{IR,(min)}$ of the PV generator bus and the rated voltage generated $U_{PV,(rated)}$ at $S_{IR,(rated)}$. In the examples in Figure 27 and Figure 28, the two ratios are $k_{WT} = 0,4$ and $k_{PV} = 0,9$.

In order to inject power to the grid with unity power factor, the fundamental component of the inverter output voltage must be slightly higher than the grid voltage:

$$\hat{u}_{CHB,1} \geq \sqrt{2}U_s \quad (53)$$

where the fundamental component of the inverter output voltage is the sum of the fundamental component of the two series cell voltages:

$$\hat{u}_{CHB,1} = \hat{u}_{A,1} + \hat{u}_{B,1} \quad (54)$$

Based on these relations, the system must be designed in such a way that the DC-link voltage is sufficient to inject power to the grid even in the partial load region. The lowest power mode is therefore considered as the worst case of operation. Now two worst case scenarios are analyzed:

- Case 1: The PV generation is zero (for example in the night) and the wind speed is at its minimum level i.e. $v_{w,(cut-in)}$:

In this case, the DC-link voltage bus of the PV generator will be zero while the DC-link voltage bus of the WT generator will be at the minimum level $U_{WT,(min)}$.

Therefore, in order to inject the power to the grid only the wind-cell can be used to generate the required voltage:

$$\hat{u}_{CHB,1} = \hat{u}_{B,1} \geq \sqrt{2}U_S \quad (55)$$

where $U_{WT,(min)}$, the minimum required DC-link voltage is equal to the amplitude $\hat{u}_{B,1}$ of the fundamental component of the output voltage.

$$U_{WT,(min)} = \hat{u}_{B,1} = \sqrt{2}U_S \quad (56)$$

Thus, the rated DC-link voltage of the WT generator is:

$$U_{WT,(rated)} = \frac{U_{WT,(min)}}{k_{WT}} = \frac{\sqrt{2}U_S}{k_{WT}} \quad (57)$$

The modulation index will be at its maximum limit of $m_{WT,(max)} = 1$:

$$m_{WT,(max)} = \frac{\sqrt{2}U_S}{U_{WT,(min)}} = \frac{\hat{u}_{B,1}}{U_{WT,(min)}} = 1 \quad (58)$$

In this case if the rated power of WT generator is injected to the grid at rated DC-link voltage $U_{WT,(rated)}$, the minimum modulation index applies to the *HB – cell B* as in the following expression:

$$m_{WT} = \frac{\sqrt{2}U_S}{U_{WT,(rated)}} = \frac{\hat{u}_{B,1}}{U_{WT,(rated)}} \quad (59)$$

By substituting (51) in (59), the minimum modulation index in this case ($P_{PV} = \text{zero}$ and $P_{WT} = \text{rated}$) follows:

$$m_{WT} = \frac{k_{WT} \cdot \hat{u}_{B,1}}{U_{WT,(min)}} \quad (60)$$

and from (58) $\frac{\hat{u}_{B,1}}{U_{WT,(min)}} = 1$, so that the minimum modulation index applied in this case is:

$$m_{WT} = k_{WT} \quad (61)$$

In general the power produced and delivered by the WT generator at unity power factor ($PF = 1$) is:

$$P_{WT} = U_{WT} \cdot I_{WT} = U_{B,1} \cdot I_S \quad (62)$$

- Case 2: The wind generation is zero and the sun irradiance is at its minimum level:

In this case, the DC-link voltage of the wind generator is zero while the DC-link voltage of the PV generator will be at the minimum level $U_{PV,(min)}$. With the same considerations like explained above this leads to:

$$\hat{u}_{CHB,1} = \hat{u}_{A,1} \geq \sqrt{2}U_S \quad (63)$$

where $U_{PV,(min)}$, the minimum required DC-link voltage is equal to the amplitude $\hat{u}_{A,1}$ of the fundamental component of the output voltage:

$$U_{PV,(min)} = \hat{u}_{A,1} = \sqrt{2}U_S \quad (64)$$

Thus, the rated DC-link voltage of the PV generator is:

$$U_{PV,(rated)} = \frac{U_{PV,(min)}}{k_{PV}} = \frac{\sqrt{2}U_S}{k_{PV}} \quad (65)$$

The modulation index will be at its maximum limit of $m_{PV,(max)} = 1$:

$$m_{PV,(max)} = \frac{\sqrt{2}U_S}{U_{PV,(min)}} = \frac{\hat{u}_{A,1}}{U_{PV,(min)}} = 1 \quad (66)$$

In this case if the rated power of PV generator is injected to the grid at rated DC-link voltage $U_{PV,(rated)}$, the minimum modulation index applies to the *HB – cell A* as in the following expression:

$$m_{PV} = \frac{\sqrt{2}U_S}{U_{PV,(rated)}} = \frac{\hat{u}_{A,1}}{U_{PV,(rated)}} \quad (67)$$

Substitute (52) in (67), the minimum modulation index in this case ($P_{WT} = \text{zero}$ and $P_{PV} = \text{rated}$) will be:

$$m_{PV} = \frac{k_{PV} \cdot \hat{u}_{A,1}}{U_{PV,(min)}} \quad (68)$$

and from (66) $\frac{\hat{u}_{A,1}}{U_{PV,(min)}} = 1$, so that the minimum modulation index applied in this case is:

$$m_{PV} = k_{PV} \quad (69)$$

In general the power produced and delivered by the PV generator at unity power factor ($PF = 1$) is:

$$P_{PV} = U_{PV} \cdot I_{PV} = U_{A,1} \cdot I_S \quad (70)$$

Now the case when both, the PV as well as the WT generators are work at their rated values is considered. So that:

$$\hat{u}_{A,1} + \hat{u}_{B,1} = \hat{u}_{CHB,1} = \sqrt{2}U_S \quad (71)$$

The rated current $I_{S,(rated)}$ is flowing to the grid at unity power factor. By assuming that both generators produce the same rated power ($P_{PV,(rated)} = P_{WT,(rated)}$), and the same rated current flowing through both HB cells, (i.e. *HB – cell A* and *HB – cell B*), thus:

$$\hat{u}_{A,1} = \hat{u}_{B,1} = \frac{1}{2}\hat{u}_{CHB,1} = \frac{1}{\sqrt{2}}U_S \quad (72)$$

For the WT generator the modulation index applies to the *HB – Cell B* in this case will be:

$$m_{WT} = \frac{\hat{u}_{B,1}}{U_{WT,(rated)}} = \frac{\frac{1}{\sqrt{2}}U_S}{U_{WT,(rated)}} = \frac{1}{2}k_{WT} \quad (73)$$

The same for the PV generator where the modulation index applies to the *HB – Cell A* in this case will be:

$$m_{PV} = \frac{\hat{u}_{A,1}}{U_{PV,(rated)}} = \frac{\frac{1}{\sqrt{2}}U_S}{U_{PV,(rated)}} = \frac{1}{2}k_{PV} \quad (74)$$

Thus, the total power injected to the grid at unity power factor ($PF = 1$) is:

$$P_{S,(rated)} = P_{PV,(rated)} + P_{WT,(rated)} = I_{S,(rated)} \cdot (U_{A,1} + U_{B,1}) \quad (75)$$

So that the inverter is operated in the minimum modulation index in order to generate the required RMS voltage at the inverter terminal to inject the grid by the rated power.

Taking all significant operating modes (zero power, lowest power, rated power) of the two generator bus bars together, the system may face nine modes of operation during a 24 hours period. These modes are:

- Zero mode of operation:

In this mode of operation, the sun irradiance is zero or more precisely below the minimum sun irradiance level suitable to transfer power and the wind speed v_w is slower than cut-in wind speed (or higher than rated wind speed). In this mode of operation the wind turbine will be blocked to standstill and there is no power injected to the grid.

- Eight active modes of operation

In each one of the active modes of operation, the two energy sources i.e. PV or WT are working either at their limits or in the range between the maximum and rated values of irradiance or wind speed. Depending on the available power on each of the sources, the available voltages in the DC-links are different and the modulation index of the inverter has to be adapted for delivering a constant output voltage.

The so defined different modes of operation are summarized in **Table 1** that includes the limit values taken by the sun irradiation and the wind speed for each mode. There are two cases in which one of the sources is not delivering any power

- If the wind speed is outside of the permitted limits, the turbine is blocked and the corresponding HB is bypassed by turning on the switches in one of the half bridges.
- If the sun irradiance is not high enough, i.e. night operation, the PV is not delivering power and the associated HB is bypassed as in the previous case.

Mode	PV generator Sun irradiance S_{IR}	WT generator Wind speed v_w
1	0	0
2	0	$v_{w,(cut-in)}$
3	$S_{IR,(min)}$	0
4	0	$v_{w,(rated)}$
5	$S_{IR,(rated)}$	0
6	$S_{IR,(min)}$	$v_{w,(cut-in)}$
7	$S_{IR,(rated)}$	$v_{w,(cut-in)}$
8	$S_{IR,(min)}$	$v_{w,(rated)}$
9	$S_{IR,(rated)}$	$v_{w,(rated)}$

It can be concluded from the nine modes described above, that the whole system should be carefully designed from the point of view of rated voltage and power. The DC-link of each HB cell must be designed to handle the rated voltage and current, i.e. the switches in each HB cell must handle the voltage limit of the DC side and the current limit at the ac side. The case of zero power in one of the sources and minimum power in the other one is the critical situation, which leads to the oversizing in the voltage capability of the inverter. Even though the CHB- topology offers some redundancy and fault tolerance, these critical cases define the operational limits of the system.

3.3 Proposal for reducing the oversizing of the inverter

The idea of a hybrid generation system connected to the grid by means of a CHB inverter has some advantages and disadvantages that are interrelated with each other.

One of the main disadvantages of the system is the problem of oversizing. As explained in 3.2, the DC-link is designed in such a way that at cut-in wind speed or minimum sun irradiance the DC-link voltage is still sufficient for the grid connection. However, this leads to a much higher DC-link voltage in the rated operation than necessary. Consequently, both HB cells of the inverter work in the low modulation index and will handle the same inverter output current $I_{S,(rated)}$. Therefore, the switches have to be dimensioned for a safe operation at rated current and voltage for the expected maximum temperature. The design for the worst case can yield to an oversizing of the power switches even if the worst case will seldom or never occur. Additionally, the operation with low modulation index tends to be less efficient, depending on the used power semiconductors. On the one hand, the on-times of the IGBTs are quite short in this operating point, which leads to low conduction losses in the IGBTs. However, during the off state of the IGBTs the corresponding diodes will conduct the current, which in general only slightly reduces the overall conduction losses of the inverter. On the other hand, the switching losses are much higher as the DC-link voltage in this mode is also higher. Hence, in general the inverter losses at same output power are higher for higher the DC-link voltage and low modulation index.

In the case of the three phase inverter as proposed in this work there is a possibility to alleviate the problem of oversizing, which is the switching between star and delta connection of the inverter or of the isolation transformer. In this section only the idea of this proposal will be discussed. The detailed investigation can be left for future works.

For the explanation the single phase example above is extended to the three phase topology. By assuming that the grid side line voltage is U_P , the isolation transformer

(if any) has a unity turn ratio and the primary side has a fixed connection (always star or always delta), there are three possible scenarios of grid integration:

a) If the inverter is connected directly to the grid or to the fixed isolation transformer, there is the possibility to switch the inverter topology between star and delta connection as depicted in Figure 29. Note that the filter inductors are connected in the delta arms of the inverter, which is not drawn in the figure for the sake of simplicity. The star connection is used, when the sum of the cell fundamental voltages ($U_{A,1} + U_{B,1}$) is lower than U_S . The phase current of the inverter is the same as the line current $I_{CHB} = I_S$, the inverter is switched to delta connection when the sum of $U_{A,1} + U_{B,1}$ is higher than U_S . In this case when the rated power is injected (case number 9 in Table 1), the inverter current I_{CHB} is reduced with the factor of $\sqrt{3}$ reducing the oversizing of the HB switches by this factor

$$I_{CHB,(\Delta-Y)} = \frac{1}{\sqrt{3}}I_S \quad (76)$$

And the inverter voltage is:

$$U_{CHB,(\Delta-Y)} = \sqrt{3}U_S \quad (77)$$

The advantage of switching to the delta configuration when sufficient DC-link voltage is available is thus the reduction of the inverter current while injecting the same power which leads to both, less switching as well as less conduction losses.

However, the delta configuration of the CHB has the drawback of circulating currents which flow through the H-Bridges of the inverter and lead to further losses, especially when injecting third harmonic voltage components to increase the maximum line to line voltage. Hence, the switching of the inverter topology to the delta configuration is quite complex and needs to be examined more in detail.

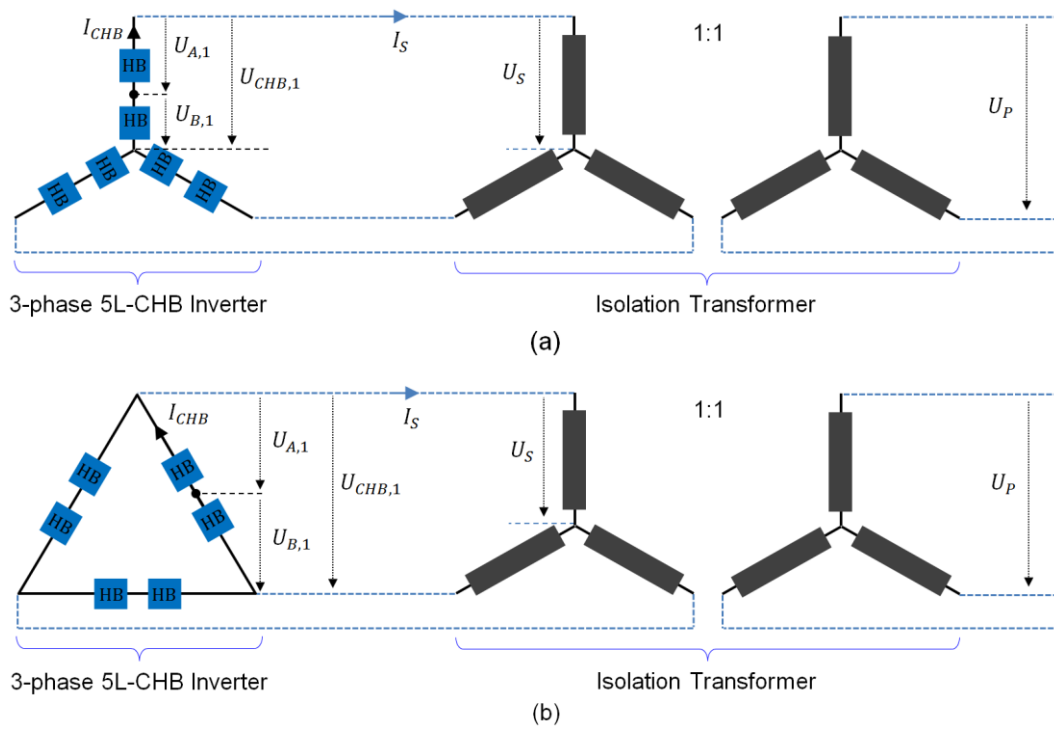


Figure 29 Star-Delta connection at the inverter side (a) Star connection (b) Delta connection

b- If the inverter is fixed to star connection but the secondary side of the isolation transformer is able to switch between the star and delta connection as shown in Figure 30, the same results of the previous scenario is achieved.

c- The third scenario of the star-delta connection is achieved by combining the two previous scenarios as shown in Figure 31. Three different cases can be achieved by switching both: the inverter and the secondary side of the isolation transformer from star to delta and vice versa depending on the required connection.

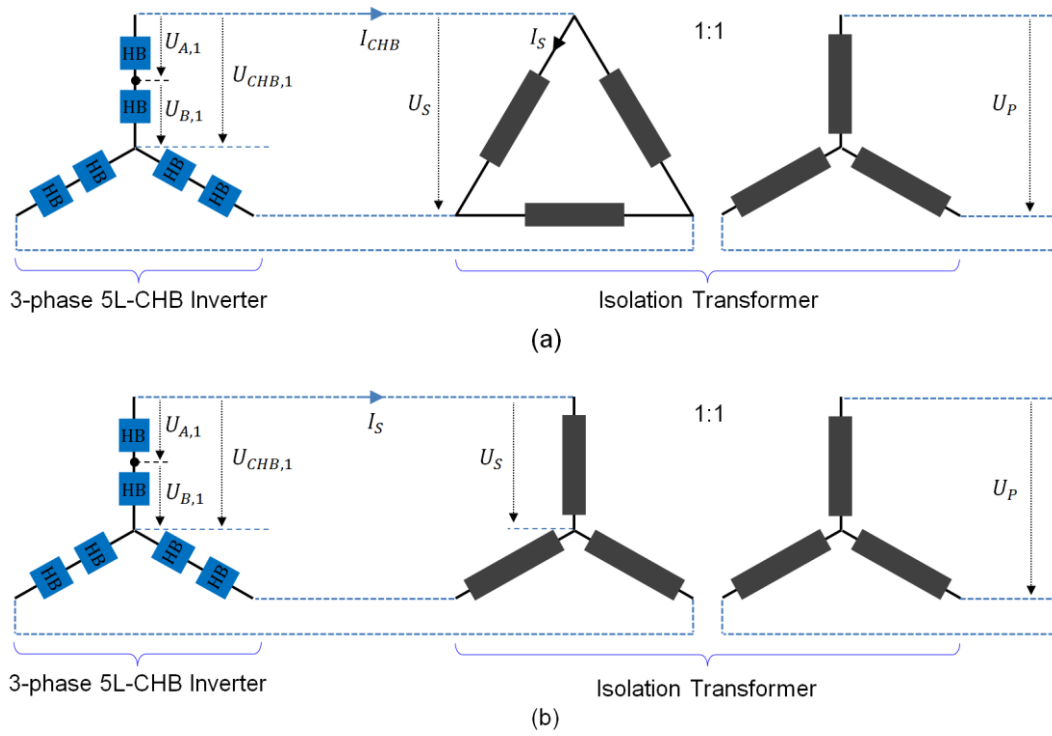


Figure 30 Star-Delta connection at the transformer side (a) Delta connection (b) Star connection

In the configurations depicted in Figure 31 a), the inverter voltage at the $(Y - \Delta)$ configuration $U_{CHB,(Y-\Delta)}$ is expressed by:

$$U_{CHB,(Y-\Delta)} = \frac{1}{\sqrt{3}} U_s \quad (78)$$

And in $(Y - Y)$ (Figure 31b) configuration it is expressed by:

$$U_{CHB,(Y-Y)} = U_s \quad (79)$$

And in $(\Delta - Y)$ (Figure 31c) configuration is expressed by:

$$U_{CHB,(\Delta-Y)} = \sqrt{3} U_s \quad (80)$$

From the expressions (78),(79) and (80) it can be written:

$$U_{CHB,(\Delta-Y)} = 3 U_{CHB,(Y-\Delta)} \quad (81)$$

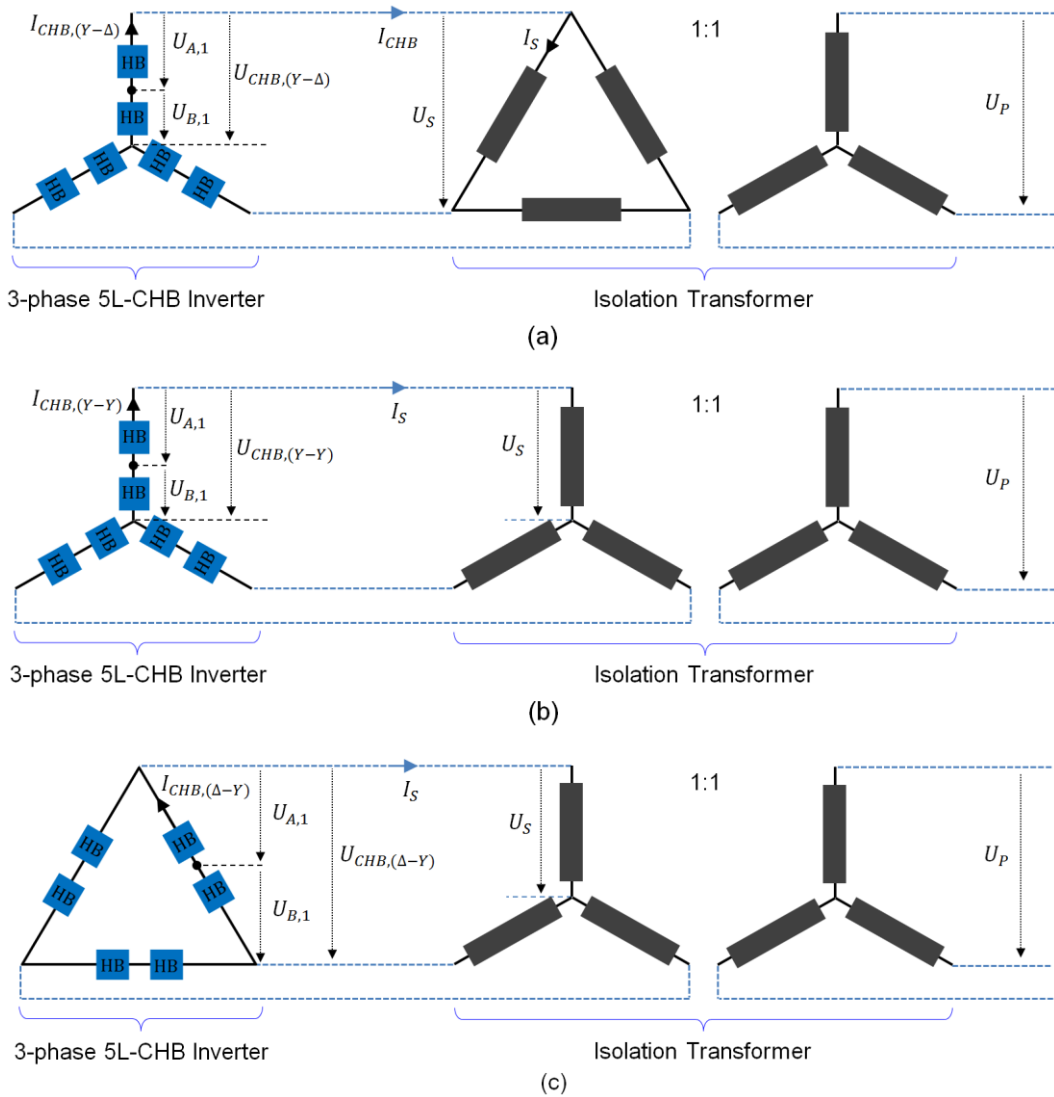


Figure 31 Star-Delta connection at both inverter and transformer side (a) Star inverter – Delta transformer (b) Star inverter and transformer (c) Delta inverter – Star transformer

The inverter current at the $(Y - \Delta)$ configuration $I_{CHB,(Y-\Delta)}$ is expressed by:

$$I_{CHB,(Y-\Delta)} = \sqrt{3} I_s \quad (82)$$

And in $(Y - Y)$ configuration is expressed by:

$$I_{CHB,(Y-Y)} = I_s \quad (83)$$

And in $(\Delta - Y)$ configuration is expressed by:

$$I_{CHB,(\Delta-Y)} = \frac{1}{\sqrt{3}} I_s \quad (84)$$

From the expressions (78), (79) and (80) it can be written:

$$I_{CHB,(\Delta-Y)} = \frac{1}{3} I_{CHB,(Y-\Delta)} \quad (85)$$

Thus, when the power is injected has its rated value, the inverter current I_{CHB} is reduced by a factor of 3 times alleviating the oversizing of the HB switches.

However, the star-delta solution still has some disadvantages like the costs of the contactors used to execute the star-delta reconfiguration. By comparing this solution with the conventional one, which uses additional DC-DC converters for each DC-link of the inverter to offer a constant DC-link voltage, the costs for the additional contactors for the star-delta-switching have to be put into relation to the expenditures for the DC-DC converters. Furthermore, the conventional solution with DC-DC converters will need ancillary devices, circuits, controllers etc. that may increase the complexity, the size and the cost, while reducing the overall system reliability. Thus, the proposed system offers a single inverter to perform the grid integration for different types of energy sources, without additional DC-DC units and with only one central controller.

3.4 Control scheme for the grid connection of the Hybrid PV-Wind system

In the area of the grid integration of regenerative power sources the main task of the inverter is to control the amount of active and reactive power which is injected into the grid. For this purpose there are two well-known control techniques: Direct Power Control (DPC) and Voltage Oriented Control (VOC) [9][12]. In the current work the VOC methods is adopted because it contains a modulator stage in the control loop

while the DPC does not. The modulator unit is very important in this work since it yields a simple maximum power point tracking algorithm (MPPT) which is applied to each H-bridge cell individually. In addition it is suitable for dealing with the power unbalance issues as it is explained in the following discussion in the feedforward modulation index compensation stage.

3.4.1 Voltage oriented control (VOC)

Voltage oriented control (VOC) is one of the common methods, which is used for the integration of the inverter to the grid. The control scheme presented in this work is based on the one proposed in [14].

Similar to the field oriented control for electrical machines, the voltage oriented control uses the space phasor equations and the system is described in a d - q rotating frame of coordinates aligned with the space phasor of the grid voltage.

The space phasor diagram of the VOC is depicted in Figure 32 and the block diagram of the VOC scheme is depicted in Figure 33.

All the quantities, the currents and the voltages are transformed from natural U - V - W reference frame to the grid voltage fixed d - q frame of coordinates by using the well-known transformation formulas.

First, the phase currents in the U - V - W system of coordinates are transformed to the orthogonal $\alpha - \beta$ coordinates by using:

$$\begin{bmatrix} i_\alpha \\ i_\beta \end{bmatrix} = \frac{2}{3} \begin{bmatrix} 1 & \frac{1}{2} & -\frac{1}{2} \\ 0 & \frac{\sqrt{3}}{2} & \frac{\sqrt{3}}{2} \end{bmatrix} \cdot \begin{bmatrix} i_U \\ i_V \\ i_W \end{bmatrix} \quad (86)$$

As long as the sum of all stator currents is zero (the star point is not connected) the three phase quantities can be transferred to the orthogonal system without loss of information.

A second transformation is used for changing from $\alpha - \beta$ coordinates to the rotating $d-q$ frame that has an angular displacement θ with respect to the α -axis.

$$\begin{bmatrix} i_d \\ i_q \end{bmatrix} = \begin{bmatrix} \cos \theta & \sin \theta \\ -\sin \theta & \cos \theta \end{bmatrix} \cdot \begin{bmatrix} i_\alpha \\ i_\beta \end{bmatrix} \quad (87)$$

The same relationships are used for the transformation of the voltages u_{UN}, u_{VN}, u_{WN} to u_α, u_β .

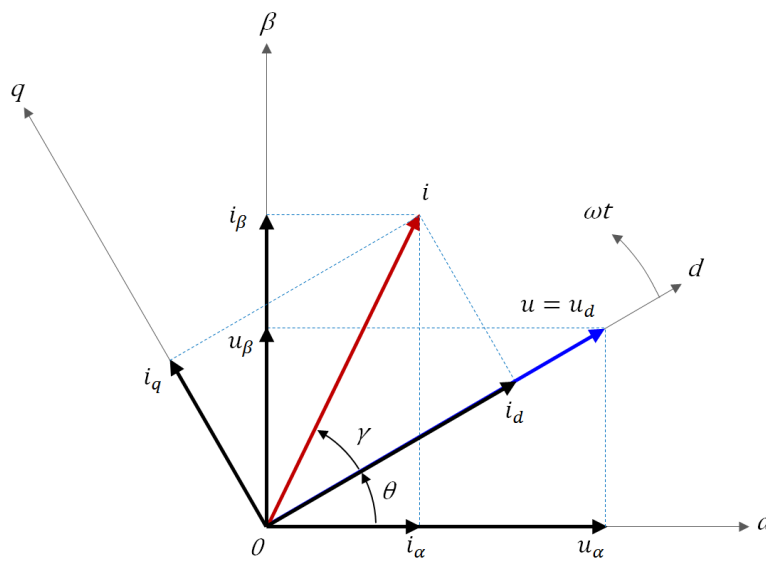


Figure 32 Space Phasor diagram of voltage oriented control (VOC)

The advantage of this rotating system of coordinates is that the controlled quantities become DC-values in steady state and that there is a simple relationship between active and reactive power and the components of the current space vectors [51], [52]:

$$p_d(t) = u_d i_d + u_q i_q \quad (88)$$

$$q_q(t) = u_q i_d - u_d i_q \quad (89)$$

where $p_d(t)$ is the instantaneous active power and $q_q(t)$ is the instantaneous reactive (or non-active) power. With the definition of the voltage fixed reference frame used here ($u_q = 0$) follows:

$$p_d(t) = u_d i_d \quad (90)$$

$$q_q(t) = -u_d i_q \quad (91)$$

From the classical VOC diagram in Figure 33 which is generally applied to conventional inverters with a single DC-Link, two types of control loops can be recognized: the voltage control loop and the current control loop. The voltage control loop is the outer loop that is used to control the DC-link voltage of the inverter while the current control loop or the inner loop is dedicated to control the power flow between the inverter and the grid.

In the voltage loop the DC-link voltage u_{DC} is measured and compared with the desired reference voltage u_{DC}^* . The reference voltage error e_{DC} is controlled to zero by using a linear proportional integral controller (*PI*) that delivers the reference value of i_d^* , which is proportional to the active power to be injected to the grid. If the voltage error e_{DC} is negative, i.e. the DC-link voltage is lower than the desired value, the controller will reduce the active power transferred from the DC-link to the grid and the DC-link voltage will rise to the desired value. If the voltage error is positive, the inverse action will be applied to increase the injection of the active power to the grid and reduce the DC-link voltage to the desired value again.

In the current control loop two of the phase currents injected to the grid i_U and i_V are measured and first transformed to the α - β reference frame (i_α and i_β) and then to the d - q system with the currents i_d and i_q . The component of the grid current i_d is compared with the reference i_d^* which is directly proportional to the active power p_d (which is given indirectly from the results of the voltage loop) while the second part of the grid current i_q is compared with the reference i_q^* which is directly proportional to the non-active or reactive power q_q . The reactive power component i_q^* is chosen depending on the system requirements. In the case of renewable energy generation it is normally set to zero in order to inject the current to the grid with unity power factor ($PF = 1$). The d - q current components are controlled by *PI* controllers and the

results are the d - q reference voltages ($u_{ref d}$ and $u_{ref q}$). These values are converted to α - β values ($u_{ref \alpha}$ and $u_{ref \beta}$) and finally to the U - V - W system ($u_{ref U}$, $u_{ref V}$, $u_{ref W}$) and sent to the modulator unit in order to generate the suitable gate signals for the IGBTs of the inverter.

$$\begin{bmatrix} u_{ref \alpha} \\ u_{ref \beta} \end{bmatrix} = \begin{bmatrix} \cos \theta & -\sin \theta \\ \sin \theta & \cos \theta \end{bmatrix} \cdot \begin{bmatrix} u_{ref d} \\ u_{ref q} \end{bmatrix} \quad (92)$$

and

$$\begin{bmatrix} u_{ref U} \\ u_{ref V} \\ u_{ref W} \end{bmatrix} = \begin{bmatrix} 1 & 0 \\ -\frac{1}{2} & \frac{\sqrt{3}}{2} \\ -\frac{1}{2} & -\frac{\sqrt{3}}{2} \end{bmatrix} \cdot \begin{bmatrix} u_{ref \alpha} \\ u_{ref \beta} \end{bmatrix} \quad (93)$$

In the current work a 5L-CHB inverter is used to perform the grid connection of the hybrid PV-Wind energy. Figure 34 shows the modified VOC block diagram with CHB inverter. There are two additional blocks added to the classic VOC as depicted in Figure 33, one block is dedicated to perform the MPPT calculation and the other one makes a compensation of the modulation index as it will be explained later. In the proposed scheme the control error for the voltage loop e_t is obtained from the difference between the sum of all measured DC-Link voltages and the sum of all reference values calculated by MPPT algorithm

$$e_t = \sum_{\substack{i = U, V, W \\ j = 1, 2}} u_{DC-HB ij} - \sum_{\substack{i = U, V, W \\ j = 1, 2}} u_{MPPT-HB ij} \quad (94)$$

where $u_{DC-HB ij}$ is the DC-link voltage of the upper ($j = 2$) or lower ($j = 1$) cell in phase “ i ” (which may be either phase U , V or W). $u_{MPPT-HB ij}$ is the reference voltage for the certain DC-Link which is obtained by the maximum power point tracking unit. It is important to point out, that a positive error means that the sum of all DC-Link voltages is higher than the reference.

Finally, the grid phase voltages are measured for the synchronization of the control with the grid voltage, i.e. for obtaining the angular position of the d - q frame of coordinates which is aligned with the grid voltage space phasor. In this work a Quadrature Phase Locked Loop (QPLL) is used which is described in the following.

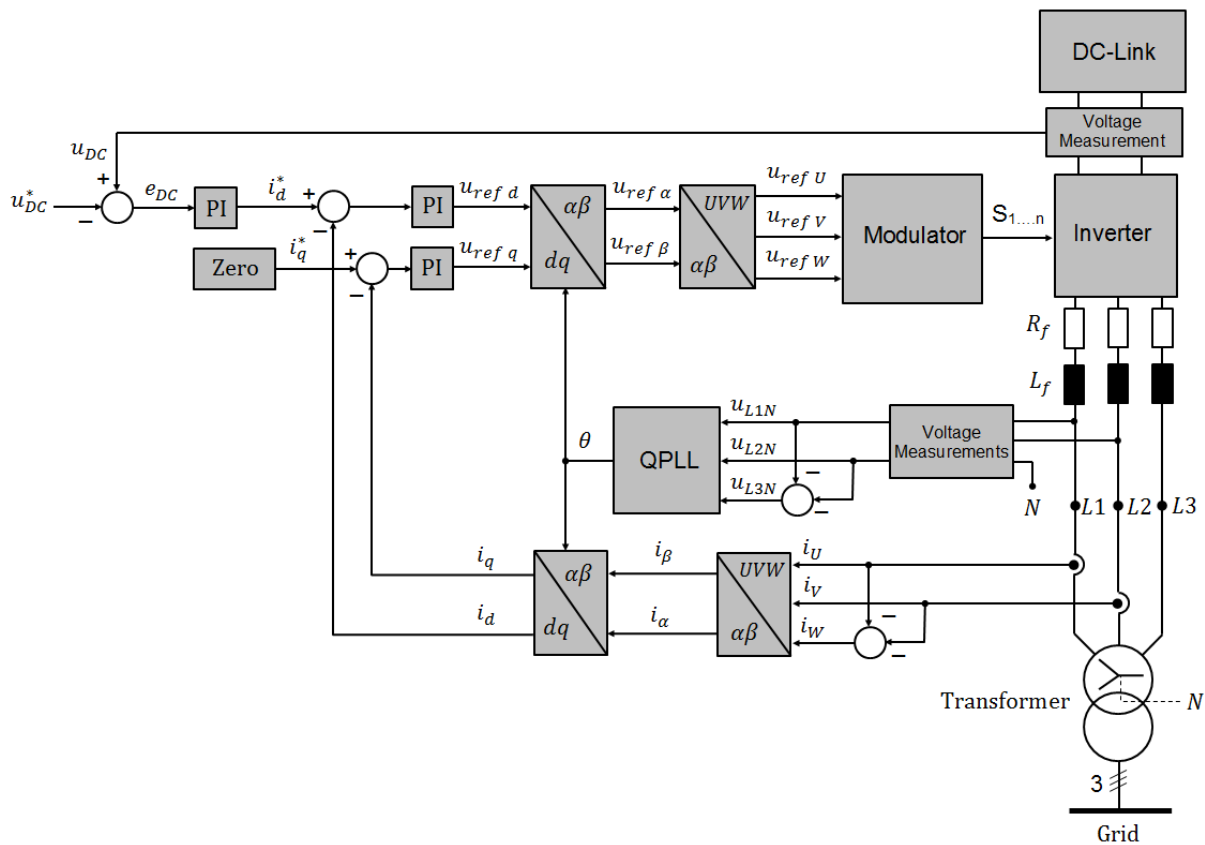


Figure 33 Classic VOC diagram

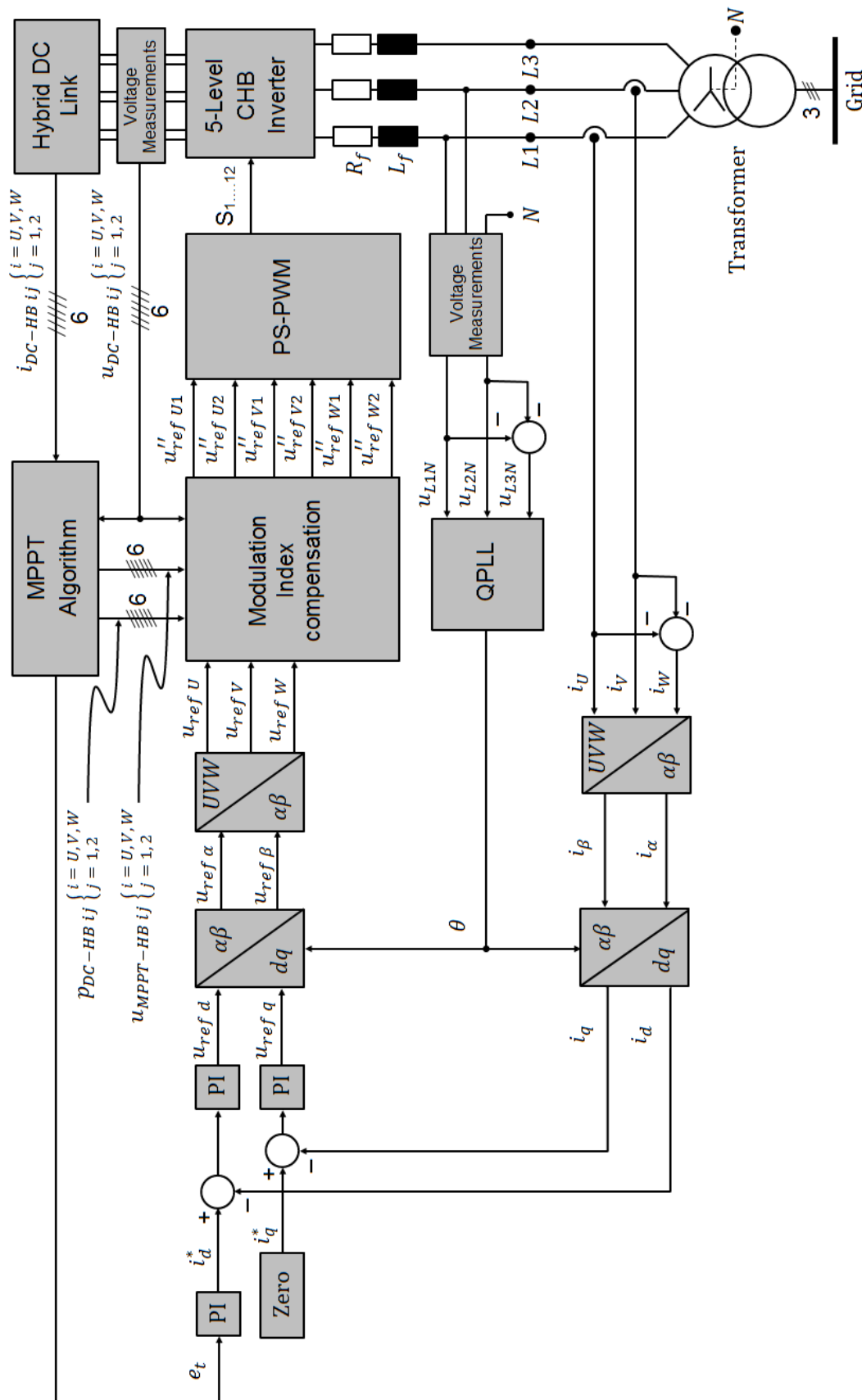


Figure 34 voltage oriented control diagram with feedforward modulation index compensation

3.4.2 Phase Locked Loop (PLL)

For the grid connection of the system, the amplitude and the phase as well as the frequency of the grid voltage are essential information. In order to ensure the correct alignment of the d - q system of coordinates, the detection of the phase angle of the grid voltage must be fast and correct [53]. The Phase Locked Loop (PLL) scheme is widely used for the detection of the orientation angle because of its excellent noise-rejection capability [54]. It can detect the phase and frequency of a sinusoidal signal with high resolution even in presence of noise and ensures a very wide dynamic range of operation. The Quadrature Phase Locked Loop (QPLL) is used in the grid integration and in motor control applications [41][55]-[60]. It uses two orthogonal sinusoidal signals (sine and cosine) as input signals obtained from the measurement of the grid voltage.

Three basic components of the QPLL are depicted in the block diagram in Figure 35: a phase detector (PHD), a PI and an I controller. In the same figure θ_i and θ_o represent the angle of the input (real angle of the grid voltage vector) and output (identified angle of the grid voltage space phasor) signals respectively and θ_D represent the phase error between the input and the output signals. The phase detection in the quadrature PLL is based on a space phasor representation of the voltages. Thus, the control loop is fed by the three measured phase voltages u_{UN}, u_{VN}, u_{WN} that are transformed to u_α, u_β and normalized by using the expression

$$\left. \begin{aligned} \cos(\theta_i) &= \frac{u_\alpha}{\sqrt{u_\alpha^2 + u_\beta^2}} \\ \sin(\theta_i) &= \frac{u_\beta}{\sqrt{u_\alpha^2 + u_\beta^2}} \end{aligned} \right\} \quad (95)$$

The phase error between the measured voltage space vector and the one synthesized by the PLL $\theta_D = \theta_i - \theta_o$ can be obtained by using the following trigonometric calculations:

$$v_D = \sin(\theta_i) \cdot \cos(\theta_o) - \cos(\theta_i) \cdot \sin(\theta_o) \quad (96)$$

by using the trigonometric transformations follows:

$$v_D = \sin(\theta_i - \theta_o) = \sin(\theta_D) \quad (97)$$

For small values of θ_D , v_D can be approximated as:

$$v_D \approx \theta_D \quad (98)$$

The PI controller has the function of reducing the phase error $v_D \approx \theta_D$ to zero by changing the frequency ω , that is integrated for obtaining θ_o , the phase of the synthesized system.

Further information about the QPLL can be found in [54][55]. In this work the modified version of a QPLL like presented in [41] was used as explained above. The block diagram of the proposed modified QPLL is depicted in Figure 35.

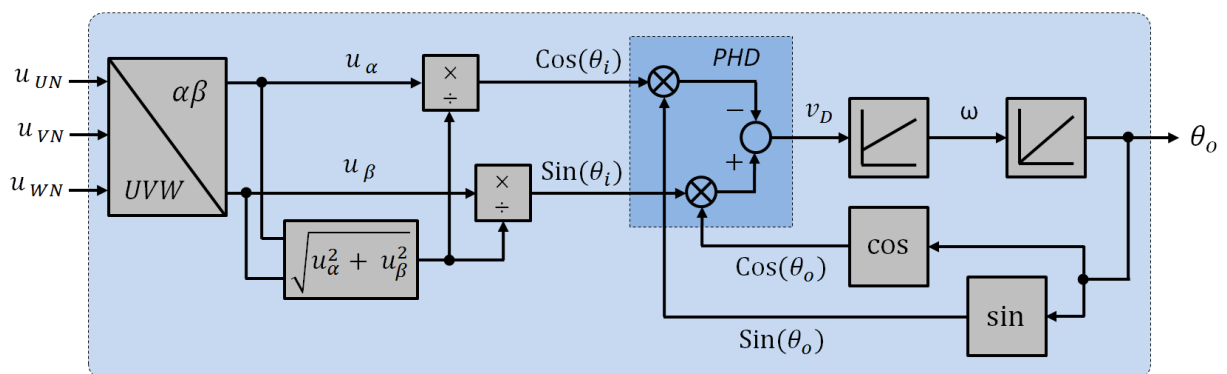


Figure 35 Modified quadrature phase locked loop (QPLL) block diagram

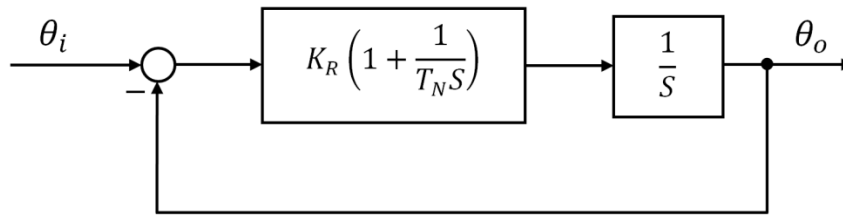


Figure 36 Block diagram of the modified QPLL in the frequency domain

The transfer function of the modified QPLL can be written as:

$$\frac{\theta_o(s)}{\theta_i(s)} = \frac{K_R T_N s + K_R}{s^2 T_N + K_R T_N s + K_R} \quad (99)$$

where K_R and T_N represent the proportional and time constant of the PI controller respectively. The last equation can be rewritten as:

$$\frac{\theta_o(s)}{\theta_i(s)} = \frac{K_R s + K_R/T_N}{s^2 + 2\xi\omega_n s + \omega_n^2} \quad (100)$$

Being

$$\left. \begin{aligned} \omega_n &= \sqrt{\frac{K_R}{T_N}} \\ \xi &= \frac{K_R T_N}{2 \cdot \sqrt{K_R T_N}} \end{aligned} \right\} \quad (101)$$

where ω_n is the natural frequency of the modified QPLL and ξ is the damping coefficient. Equation (101) means that different dynamic characteristic can be obtained by selecting suitable parameter of the PI controller. The performance of the modified QPLL is presented in the next chapter within experimental results.

3.5 Feedforward compensation of the modulation index

As it was mentioned in the previous chapter, the maximum power generated by the PV-panels is affected by two factors: the operating temperature of the panels and the sun irradiance. Even if supposing that all the PV-panels have the same operating temperature, each HB cell of the inverter is connected to a large number of PV-panels in several sectors and therefore they are operated under changing and distinct conditions. As practical example, the clouds may cause a partial shading of the PV-panels, that leads to an operation, in which the maximum power points of the PV-modules feeding the HB cells in the phases of the inverter may be different.

In the wind turbine generator the power generated by the turbine depends directly on the wind speed. It is also affected by the maximum power point of the wind turbine system which may change from one turbine to the other even if they are located close to each other in the same field. In order to perform the grid integration of the hybrid PV-Wind energy using a CHB inverter, two very important issues must be taken into account: the first is that the power injected to the grid should be balanced. This means, the current injected to the grid must be balanced as the grid voltage is normally balanced. An unbalanced injection of the current is not allowed by the grid code and generates pulsations in the power signals. The second aspect to be taken into account is that all the possible power generated by the PV and wind turbine must be utilized and injected to the grid in order to keep high performance of the conversion with the highest efficiency. In order to achieve these two objectives, two types of feedforward compensations can be applied in addition to the VOC. As explained in the following the feedforward loop acts on the reference voltages generated by the voltage oriented control before they are sent to the modulation stage:

- The first type of feed forward is called *per-phase compensation* which is achieved through the modification of the reference phase voltages.
- The second one is called *per-cell compensation* which is attained by compensating the reference signal of each individual HB cell.

3.5.1 Compensation of the reference signals (per-phase compensation)

In the conventional VOC scheme as depicted in Figure 33 the current loop will generate a balanced three phase system described by the three reference voltages that are sent to the modulator unit in order to generate the output phase voltages of the inverter. However, in the system described here, each HB of the inverter may deliver a different power to the grid even if the system has the same DC-Link voltages (especially in the PV-panels) resulting in an unbalanced current system injected to the grid. By assuming a balanced voltage on the grid an unbalance of power is the result. In order to overcome this problem, an inverse unbalanced voltage must be added to the inverter output voltages that have to be proportional to the power unbalance. That can be achieved by a shifting of the neutral point of the inverter [14]. The phase voltage equations of the grid side as depicted in Figure 25 can be written as:

$$u_{UM} = u_{L1N} + R_f i_U + L_f \frac{di_U}{dt} + u_{MN} \quad (102)$$

$$u_{VM} = u_{L2N} + R_f i_V + L_f \frac{di_V}{dt} + u_{MN} \quad (103)$$

$$u_{WM} = u_{L3N} + R_f i_W + L_f \frac{di_W}{dt} + u_{MN} \quad (104)$$

where R_f and L_f are respectively the winding resistance and inductance of the filter, u_{MN} is the common mode voltage difference between the inverter (M) and grid (N) neutral points. The average value of this voltage is equal to zero under balanced operation conditions.

From the equations above it is obvious that the currents in each phase not only depend on the inverter output voltage in the corresponding phase but also on the common mode voltage u_{MN} . Thus, it is possible to redistribute the power generated by the three phases of the inverter in order to guarantee balanced currents at the grid side even under unbalanced power distribution in the HB cells by shifting the neutral point of the inverter. In this way the inverter phases can inject a different power to the grid while the current remains balanced. In other words, the phase of the inverter which has a cell operated at lower MPP will generate a lower output phase voltage with the same

current like the other phases working at normal MPP (desired operation point) resulting in an unbalanced three phase voltage system. Nevertheless, it results into balanced inverter line voltages, currents and power. Figure 37 shows the phasor diagram of the inverter output voltages for both the balanced and the unbalanced conditions.

To perform the shifting of the neutral point some methods have been proposed in the literature. In [7] the neutral point is moved to the new position by changing the phase angle between the inverter voltages, in order to rebalance the output currents for the CHB under fault or under reduced power conditions. In the present work the proposed scheme is based on the idea presented in [14] where the movement of the neutral point is performed through the injection of a zero sequence in the modulation stage. It is a straightforward method with a simple implementation. Moreover, as the injected voltage is a zero sequence it does not affect the line-to-line voltages of the inverter, allowing the symmetrical operation even under unbalanced operating conditions. The proposed compensation scheme is depicted in Figure 38 (a), where $u_{ref U}$, $u_{ref V}$ and $u_{ref W}$ are the reference voltages obtained from the VOC scheme and $u'_{ref U}$, $u'_{ref V}$ and $u'_{ref W}$ are the compensated reference voltages by the *per-phase compensation*.

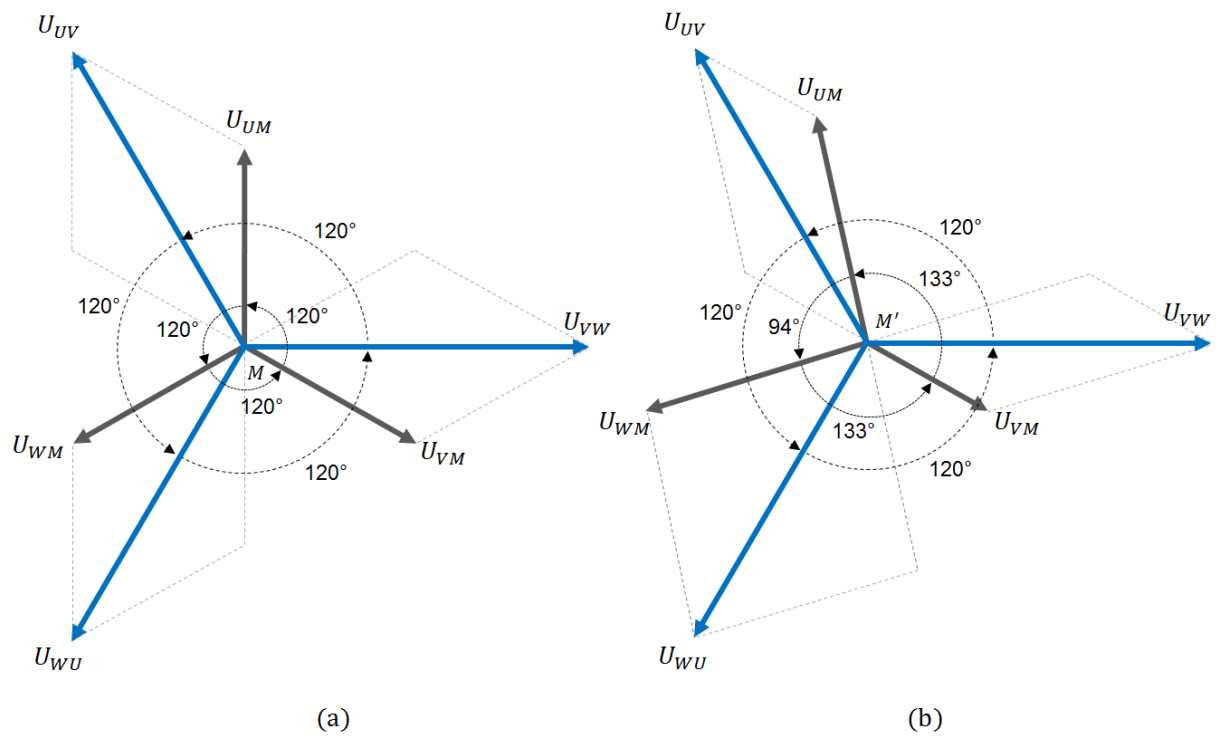


Figure 37 Phasor diagram of the inverter output phase and line voltages (a) for balanced operation conditions (b) for unbalanced operation conditions

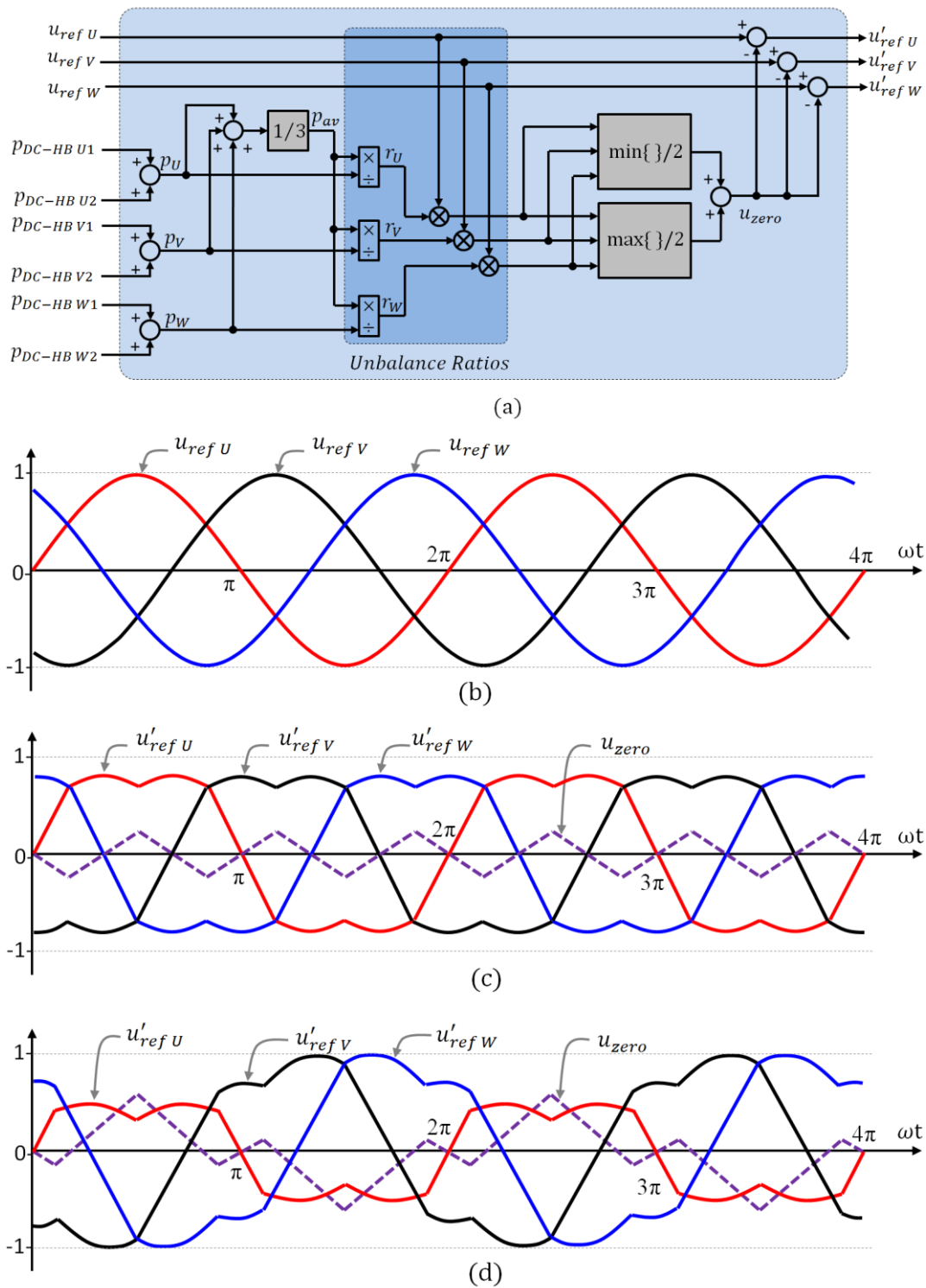


Figure 38 Reference signal compensation (a) Block diagram (b) Reference signal before compensation (c) Reference signal after compensation for balanced conditions (d) Reference signal after compensation for unbalanced conditions

To perform the compensation, an imbalance ratio is computed for each phase (r_U , r_V and r_W) as:

$$r_U = \frac{p_{av}}{p_U} \quad (105)$$

$$r_V = \frac{p_{av}}{p_V} \quad (106)$$

$$r_W = \frac{p_{av}}{p_W} \quad (107)$$

where, p_U , p_V and p_W are the summation of the instantaneous input powers of both cells (upper and lower) of the corresponding phase (U , V and W) of inverter (i.e. $p_U = p_{DC-HB U1} + p_{DC-HB U2}$, $p_V = p_{DC-HB V1} + p_{DC-HB V2}$ and $p_W = p_{DC-HB W1} + p_{DC-HB W2}$) (the grid power in the three phases is equal due to the per phase balancing method) and the average power p_{av} over all three phases is calculated as:

$$p_{av} = \frac{p_U + p_V + p_W}{3} \quad (108)$$

After obtaining the factors r_U , r_V and r_W the min-max sequence u_{zero} is calculated according to the following equation:

$$u_{zero} = \frac{\max\{r_U \cdot u_{ref U}, r_V \cdot u_{ref V}, r_W \cdot u_{ref W}\}}{2} + \frac{\min\{r_U \cdot u_{ref U}, r_V \cdot u_{ref V}, r_W \cdot u_{ref W}\}}{2} \quad (109)$$

In which the “*max*” function returns the maximum value of the three instantaneous arguments and the “*min*” function returns the minimum value of the three instantaneous arguments.

The compensated phase reference voltages are computed as:

$$u'_{ref U} = u_{ref U} - u_{zero} \quad (110)$$

$$u'_{ref V} = u_{ref V} - u_{zero} \quad (111)$$

$$u'_{ref W} = u_{ref W} - u_{zero} \quad (112)$$

The method of compensation described above has some advantages: there is no need to install extra current measurements or to implement additional estimators to calculate the power delivered by each DC-link of the inverter because these values are already calculated and required for the MPPT algorithm. Moreover, the computational effort is very low because it computes the zero sequence in (109) by using the trivial minimum-maximum sequence functions and delivers a simple scheme of additive compensation to the original references. Therefore, this control structure offers a good and fast dynamic response. The compensation will occur as soon as the unbalance in the power produced by the different cell is detected and takes the system back to the balance operation. The original and the modified reference voltages are depicted in the Figure 38 (b, c and d).

3.5.2 Compensation of the individual reference signals (per-cell compensation)

Once the reference signals have been changed by the per-phase compensation unit, the redistribution of the power of the two cells in one phase of the converter is still required. If a phase-shifted PWM is used, the reference voltage that results from the voltage oriented control (VOC) and is compensated by the above explained per-phase balancing method results to be the same for both, upper and lower HB cell of one phase of the inverter.

In a CHB inverter, the multilevel stepped waveform is produced based on the phase shift between the carrier signals. This kind of modulation produces the same average utilization of the cells and leads to similar average powers in both cells. However, in the proposed hybrid system the power produced by the PV panels is not necessarily equal to the power generated by the WT generators as it was previously discussed in

this chapter. For this reason the redistribution of the power between the HB cells in the same phase becomes mandatory, especially when there is only one type of energy generation present (either solar or wind) and the other one is bypassed.

This type of imbalance was investigated for a single phase CHB PV system in [8][9] and for a three phase CHB PV system in [10][12][14]. The same approach used in [10] is utilized in this work.

The idea behind this type of compensation mechanism is to redistribute the usage of the cells of one phase in the same proportion of the unsymmetrical power generated by each HB cell. For this purpose the *ON* and *OFF* times generated by the PWM unit are redistributed. By changing the conduction times of the switches, the voltage and finally the active power delivered by the cell is increased or decreased. In other words, the total required voltage which the inverter needs to generate in one phase is the sum of the two corresponding cells. The voltage distribution is now set according to the actual DC-powers of the two cells. E.g. if the upper cell delivers currently the double power compared to the lower cell, the upper cell will generate $2/3$ of the phase voltage while the lower cell generates $1/3$ of the phase voltage. This simple compensation scheme is shown in Figure 39 (a).

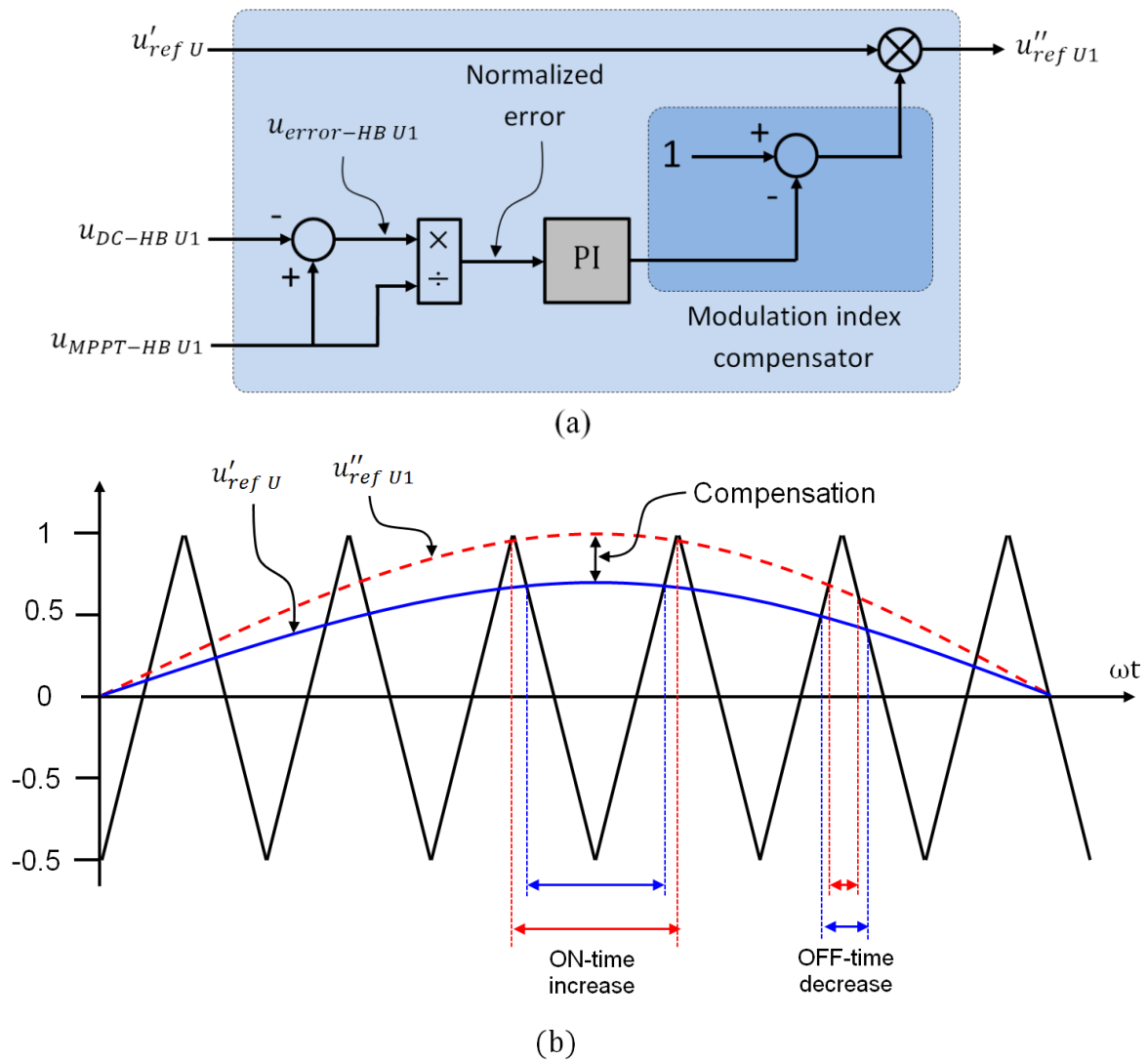


Figure 39 Compensation of the individual reference signals (a) Compensation scheme block diagram (b) effectiveness of compensation in ON time and OFF time

The DC-link voltage error for each individual HB cell is obtained from the difference between the voltage reference generated by the MPPT algorithm $u_{MPPT-HB}$ and the actual, measured DC-link voltage u_{DC-HB} .

$$u_{error-HB ij} = u_{MPPT-HB ij} - u_{DC-HB ij} \quad (113)$$

$$i = U, V, W; j = 1, 2$$

The result is normalized and fed to a *PI* controller that adjusts the amplitude of the individual reference signal $u''_{ref U1}$. The compensation acts in a manner that the

amplitude of the references used for each HB cell is modified proportionally to the error of their respective DC-link voltages. A feedforward correction that redistributes the *ON* and *OFF* times as shown in Figure 39 (b) is obtained in this manner, where $u''_{ref\ U1}$ is the compensated reference voltage by the *per-cell compensation*. The *ON/OFF*-times of the power switches depend on the modulation indices i.e. to the ratio between the modulation and the carrier (triangular) function. Hence, the same waveform with higher instantaneous value i.e. higher modulation index produces larger *ON*-times while lower *OFF*-times are achieved the desired redistribution of the power in the cells.

The same procedure can be applied if a SPM technique is used, yet its implementation is not straightforward like in the case of PS-PWM because the compensation has to be carried out in the state machine unit by modifying the *ON/OFF* time calculated by the SPM algorithm after each cycle of modulation, which demands a higher computational effort. For this reason, in this work the PS-PWM is used, it is simple, it represents a straightforward approach, leads to less computational efforts and is easier in the implementation.

3.6 Maximum power point tracking (MPPT)

The tracking of the maximum power point (MPP) of a photovoltaic (PV) array and of a wind turbine (WT) is an essential task in the operation of PV and WT systems. It is well known that the solar and wind turbine generators have nonlinear power-voltage characteristic which varies with the sun irradiation and temperature in the case of a PV generator or with the wind speed in case of the WT generator as it is depicted in Figure 27 and Figure 28. Both characteristics have only one maximum power point (MPP), in which the PV or WT systems are operated at maximum efficiency and generate their maximum output power, whose amplitude depends on ambient conditions. For the optimum operation of the system, the location of the MPP has to be found online. There are several methods for fulfilling this task. Two of them are commonly used. The first approach is a model based method that requires the exact knowledge of the weather conditions, e.g. sun irradiance, wind speed, etc. as well as all the parameters

for the PV or WT generator. Since these values are in general not known, the second approach is favored which is based on search algorithms. By using one of these procedures, the PV arrays or WT generators are kept working at their MPP [61].

In the PV generator a DC-DC converter is normally used to interface the PV module to the load or to the grid connected inverter. This DC-DC converter adapts the load to the PV array in order to ensure that the PV module works at its maximum power point and maximum power is transferred from the array to the load. For this purpose the duty cycle of the DC-DC- converter is changed by the control until the optimum power point is obtained [61]. One of the contributions of the present research work is that the PV array and the WT generator are connected to the HB cell without requiring a DC-DC-converter in between. Therefore, the adaptation has to be performed in the modulation stage. As discussed in a previous section, in this stage the reference signal of each HB cell is individually modified by adding compensation signals.

The shape of the power-voltage curve of the WT generator is principally similar to the power-voltage curve of the PV array as it is depicted in Figure 27 and Figure 28, thus the same maximum power point tracking techniques can be used.

The Perturb and Observe method (P&O) is the most frequently used algorithm to track the maximum power for PV system [61]-[66] as well as for WT system [67]-[71]. It is based on the idea that the operating voltage of the PV generator is perturbed in a given direction by a small voltage disturbance and the change in power is observed. If the power delivered from the generator increases, the operating point is being moved toward the MPP. Therefore, the operating voltage must be further perturbed in the same direction. If the power delivered from the PV array decreases, the operating point is being moved away from the MPP. In this case, the direction of the perturbation of the operating voltage must be reversed [64]. Thanks to its simple structure, that it requires few parameters and that it is easy to implement, it has become a standard MPPT method in many applications [63]. Figure 40 show the flow chart of the P&O-MPPT algorithm used in the current work.

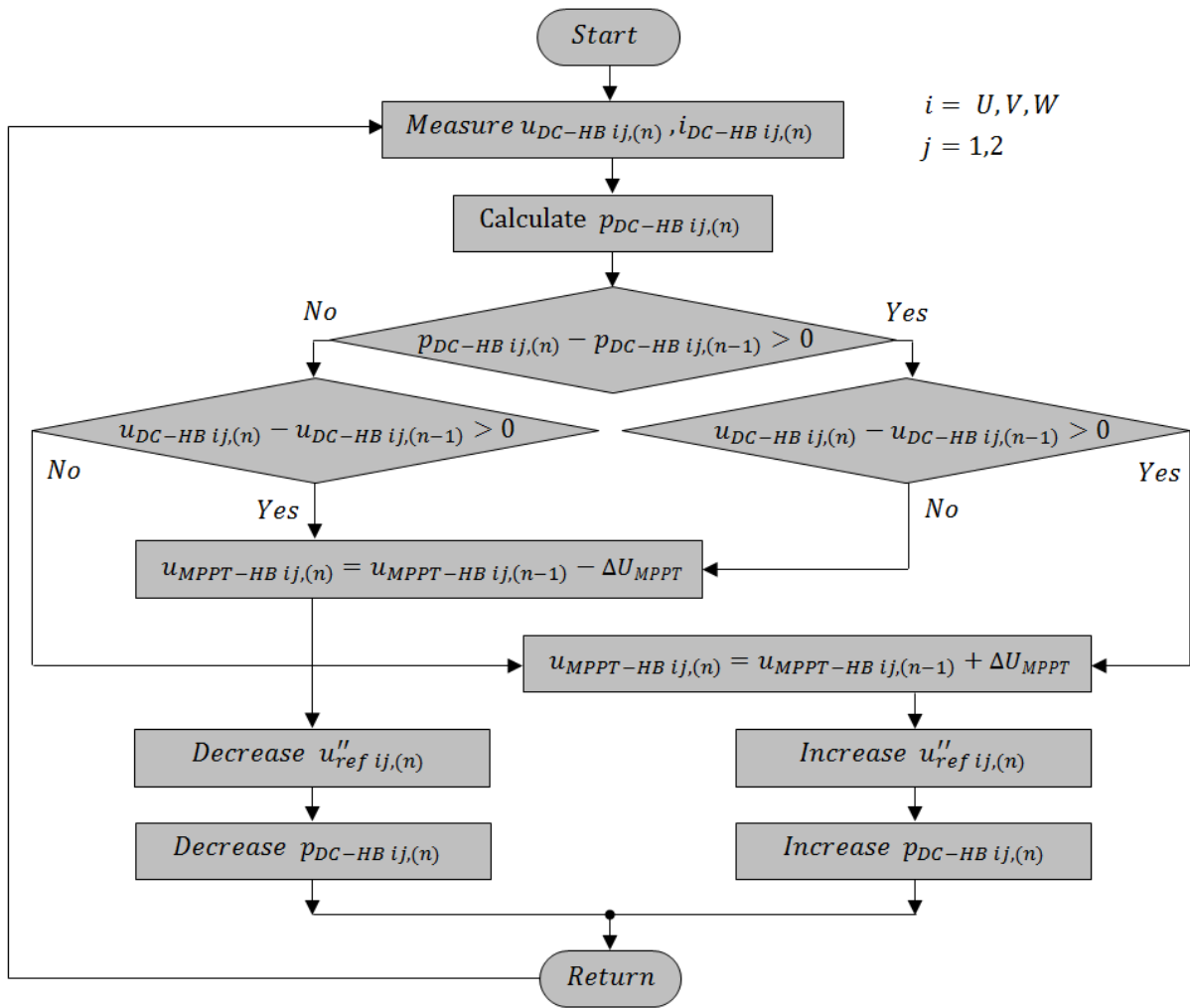


Figure 40 Flow chart for P&O MPPT algorithm

Based on the previous operation principle, the perturbation and observation process in the proposed hybrid system including WT and PV generator is realized in the present work as explained in the following. Without loss of generality, the PV array connected to the upper HB of phase U is considered ($HB-Cell U1$) but the same procedure can be applied to the other HB cells. At each sampling time, the voltage and the current of the PV are measured and the power is calculated. The voltage and power are compared with the values obtained in the previous sample time, depending on this, four different cases are possible and summarized in Table 2.

Table 2 Four different cases of P&O MPPT algorithm

	$u_{DC-HB U1,(n)} \uparrow$	$u_{DC-HB U1,(n)} \downarrow$
$p_{DC-HB U1,(n)} \uparrow$	Case 1 $u_{MPPT-HB U1,(n)} = u_{MPPT-HB U1,(n-1)} + \Delta U_{MPPT}$	Case 2 $u_{MPPT-HB U1,(n)} = u_{MPPT-HB U1,(n-1)} - \Delta U_{MPPT}$
$p_{DC-HB U1,(n)} \downarrow$	Case 3 $u_{MPPT-HB U1,(n)} = u_{MPPT-HB U1,(n-1)} - \Delta U_{MPPT}$	Case 4 $u_{MPPT-HB U1,(n)} = u_{MPPT-HB U1,(n-1)} + \Delta U_{MPPT}$

- Case 1 and 4: The reference voltage $u_{MPPT-HB U1}$ is incremented by a small perturbation value (ΔU_{MPPT}) and the power injected to the grid $p_{DC-HB U1}$ is reduced, while the amplitude of the reference signal $u''_{ref U1}$ in the compensation unit is reduced.
- Case 2 and 3: The reference voltage is decremented and the power injected to the grid increases as the amplitude of the reference signal $u''_{ref U1}$ in the compensation unit increases.

The process is repeated periodically for each sample time until the MPP is reached. The system is operated around the MPP. This variation can be minimized by reducing the size of the perturbation value. In this work, the perturbation value of the MPPT process used for the WT generator is only 10% of the perturbation value used in the MPPT process for the PV generator because the dynamic response of the WT generator is much slower than the dynamics of the PV generator due to the high inertia of the turbine, the gearbox (if any) and the generator.

4 Simulation and Experimental Results

4.1 Introduction

The effectiveness of the control scheme and of feedforward compensation technique for the grid integration of the hybrid PV-WT system has been verified by experiments in the laboratory. This chapter is divided in two sections: the first section is dedicated to the detailed explanation of the laboratory setup, which include the emulator system for both PV and WT generators. The second section deals with simulation and experimental results of the steady state operation using hybrid PV-WT generator for both balanced and unbalanced operation conditions.

4.2 Laboratory setup

4.2.1 Grid connection system

The structure of the laboratory set up for the grid integration of the hybrid *PV-WT* system is shown in Figure 41. The utilized experimental five-level, three-phase modular cascaded converter, shown in Figure 42 (a), was built by using six identical H-bridge modules (two H-bridges per phase). Each H-bridge is placed on a single module containing four discrete IGBTs of type IRGPH40UD and the heat sink. Figure 42 (b) shows one of the single H-bridge modules. Six isolated DC-links were connected to the inverter, each HB cell of the upper layer (*HB U1, V1 and W1*) was connected to a corresponding emulator for the PV generator. The lower layer cells (*HB U2, V2 and W2*) were each connected to a separate emulator of the WT generator. The overall cascaded converter switched output was connected to the 50-Hz grid via an inductive filter and transformer.

The system is controlled by a single floating-point digital signal processor unit (TMS320F28335 eZdsp). This board is especially devised for control tasks. It includes sixteen channels of 12-bit A/D converters and up to 18 PWM channels. The DSP was programmed in C code and compiled to machine language using the software “code

composer studio v3.3”. The communication between the DSP board and the computer is carried out by using a built-in standard USB interface. Fiber optic communication interface is used in order to avoid the influence of noise in the switching signals.

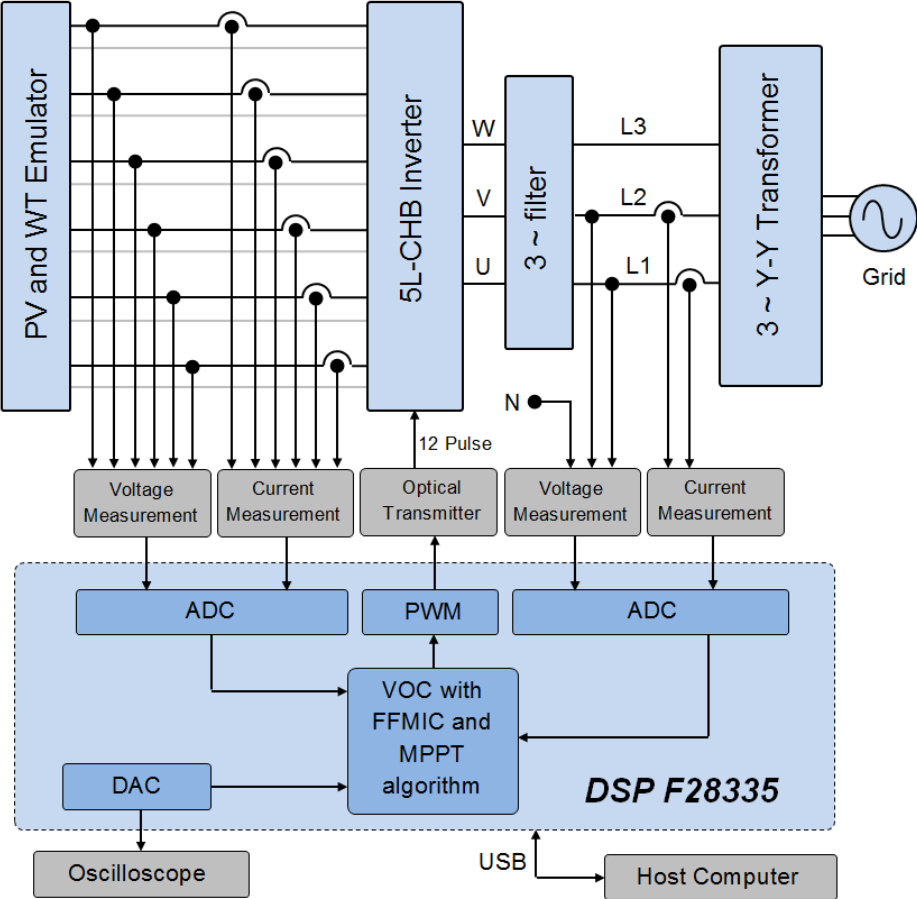


Figure 41 Structure of the laboratory set up for the grid integration of the hybrid PV-WT system

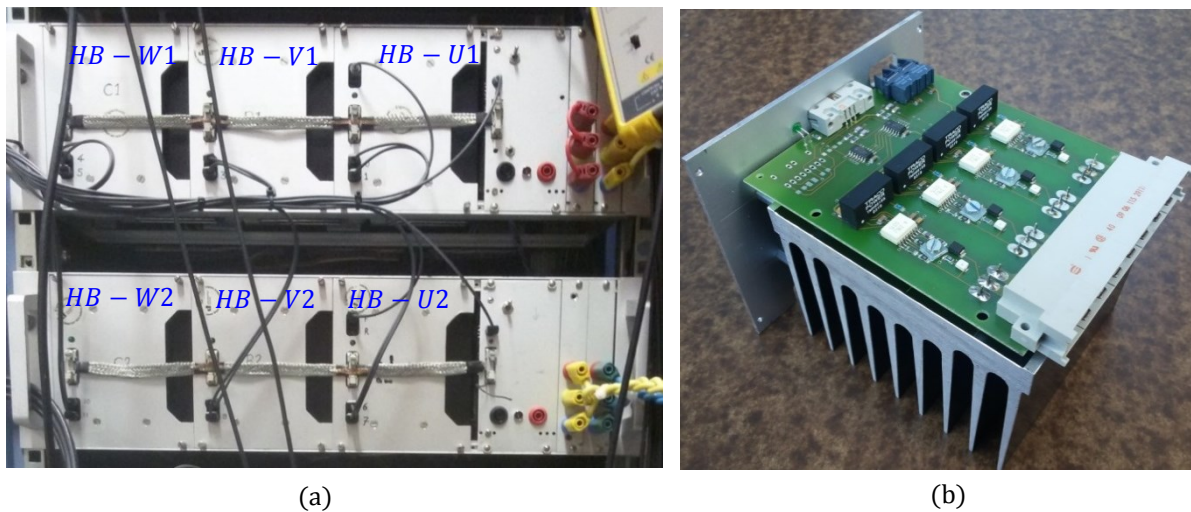


Figure 42: (a) Three phase 5-level CHB inverter (b) Single H-bridge cell

4.2.2 Photovoltaic and Wind turbine emulator

The PV and WT generators were emulated in the experimental set-up. Figure 43 shows the block diagram of the PV and WT emulator system. An extra DSP was used to control the emulation process. The PV panels were emulated by using three programmable DC supplies; each device offers the possibility to control either the current or the terminal voltage, in the implemented set-up the current control mode was used and the produced terminal DC voltage was measured and sent to the DSP through an A/D converter for its processing.

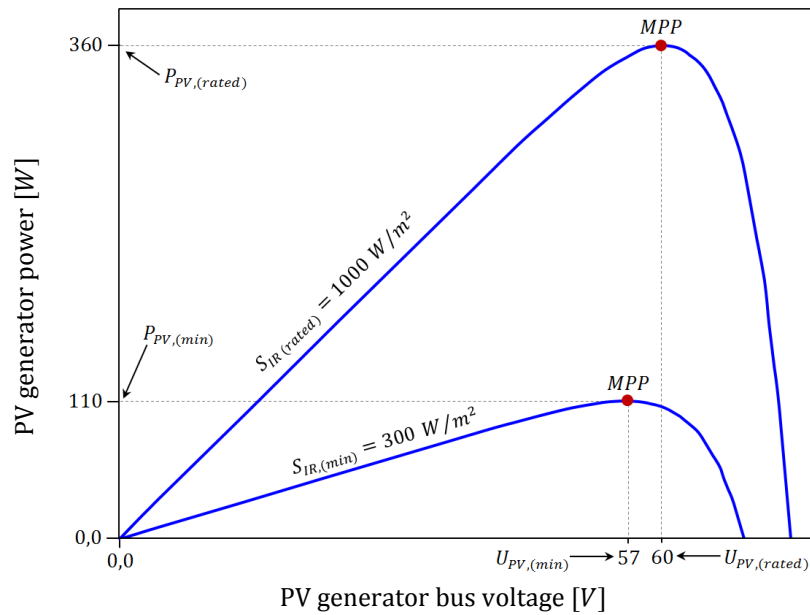


Figure 44 PV generator Voltage vs. Power characteristics curve

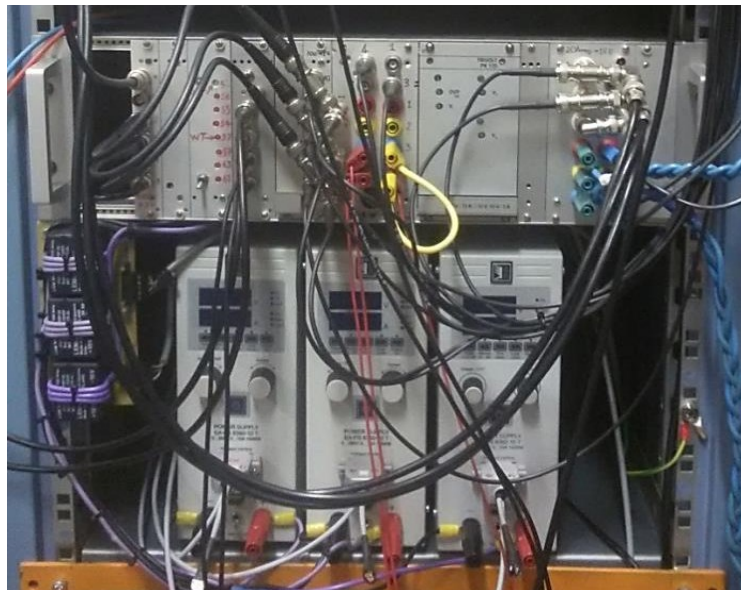


Figure 45 Emulator system for the PV-panels

The WT generators were emulated by using three identical PMSGs. Each generator was connected to a separate three phase diode rectifier. The rated DC voltage of the WT generator bus at rated wind speed $v_{w,(rated)}$ was set to be 70V while each of the generators produces 315W at the MPP. The generators are coupled mechanically to a

single induction machine via toothed belts and pulleys. The induction machine was driven by an inverter, which has the possibility to control either the motor torque or the speed. In the designed set-up, the speed control mode was used while the motor torque that is calculated by the drive is sent to the control board through an A/D converter. The torque-speed characteristics curve was programmed in the DSP by using a lookup table as well. As in the case of the PV-Emulator the output value of the lookup table was sent via pulse width modulated signal with low pass filtering to the drive of the induction machine in order to control the speed of the generators and close the emulator loop. Figure 46 shows the voltage vs. power characteristic used in the emulation of the WT generator and Figure 47 shows the WT emulator system. Figure 48 shows the complete laboratory set-up for the grid connection of the hybrid PV-Wind system.

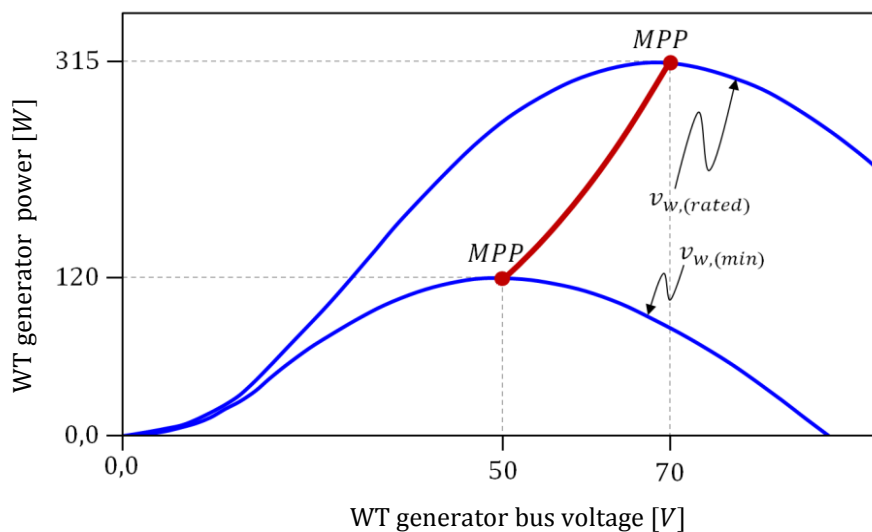


Figure 46 WT generator Voltage vs. Power characteristics curve

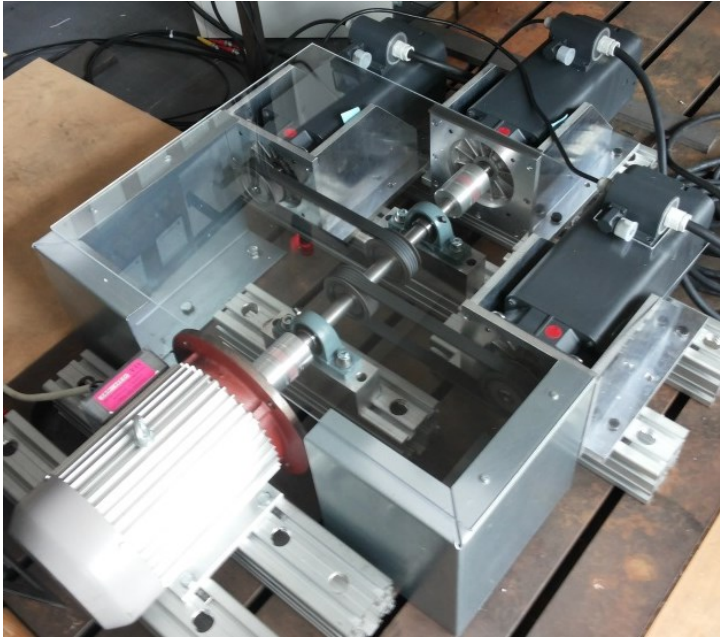


Figure 47 Emulator system for the wind-turbines



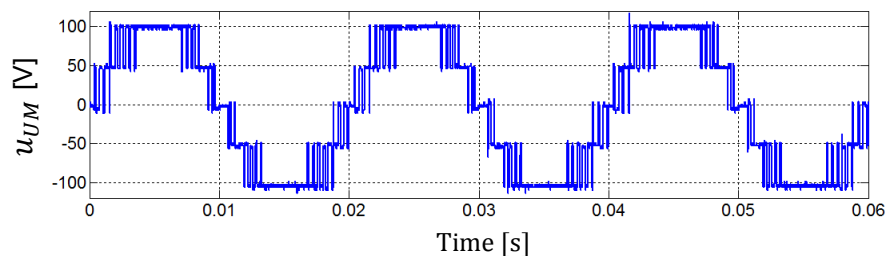
Figure 48 View of the inverter and control part of the laboratory set-up

4.3 Experimental results of the modulation methods

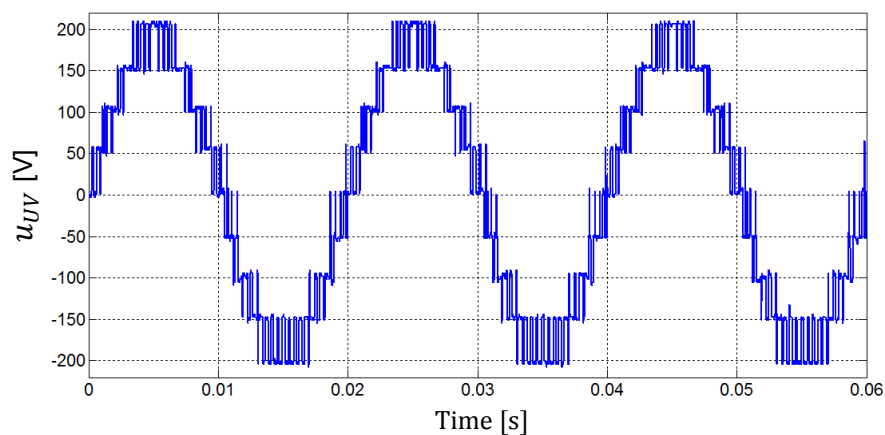
First the two implemented modulation techniques were validated by means of measurements in open loop operation and by using a resistive load, the DC-link voltages of the all HB cells of the inverter were set to the fixed value of $50V$ by using six isolated DC supplies.

4.3.1 Space phasor modulation (SPM)

The results of the SPM were obtained at a modulation frequency $f_s = 2,5kHz$ and a modulation index $m = 0,95$. As it was mentioned in section 2.6.1.3 there are two types of the modulation sequences: the *continuous* - PWM (C-PWM) and *discontinuous* - PWM (DC-PWM). Figure 49 and Figure 50 show the inverter output phase voltage u_{UM} and line to line voltage u_{UV} for the *discontinuous* and *continuous* modulation respectively.



(a) Phase voltage



(b) Line to line voltage

Figure 49 Inverter output voltages in the case of discontinuous modulation (DC-PWM)

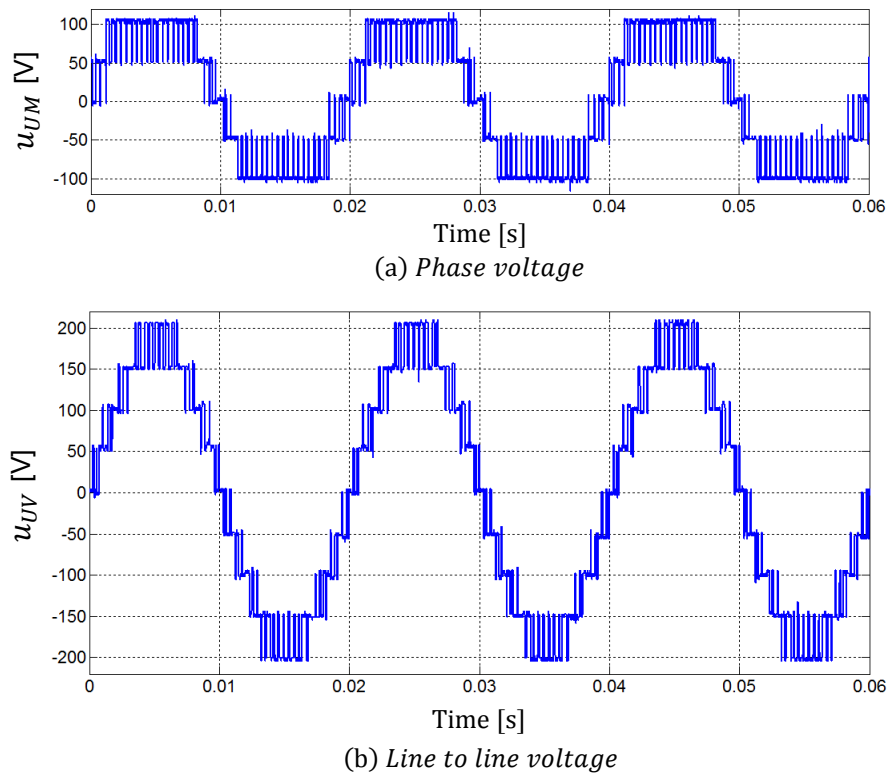
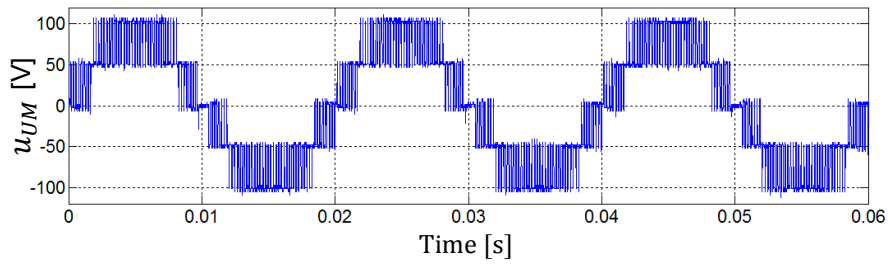


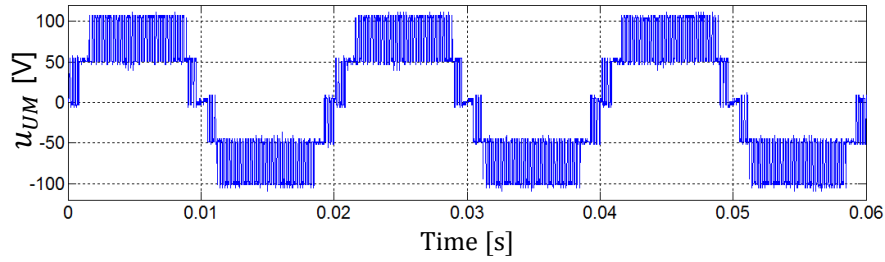
Figure 50 Inverter output voltages in the case of continuous modulation (C-PWM)

4.3.2 Phase-shifted pulse width modulation (PS-PWM)

The results of the PS-PWM were obtained at a modulation frequency $f_s = 5kHz$ and a modulation index $m = 0,95$. Figure 51 shows the inverter output phase voltage u_{UM} with and without zero sequence voltage injection method.



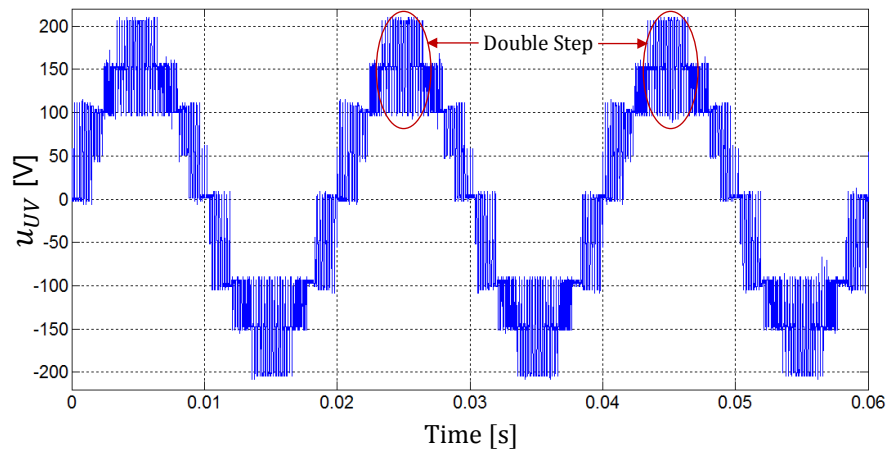
(a) without zero sequence voltage injection



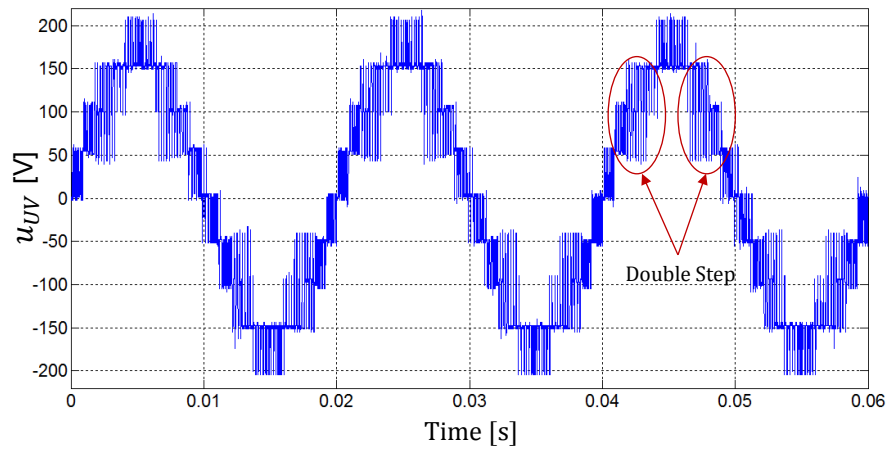
(b) with zero sequence voltage injection

Figure 51 Inverter output phase voltage

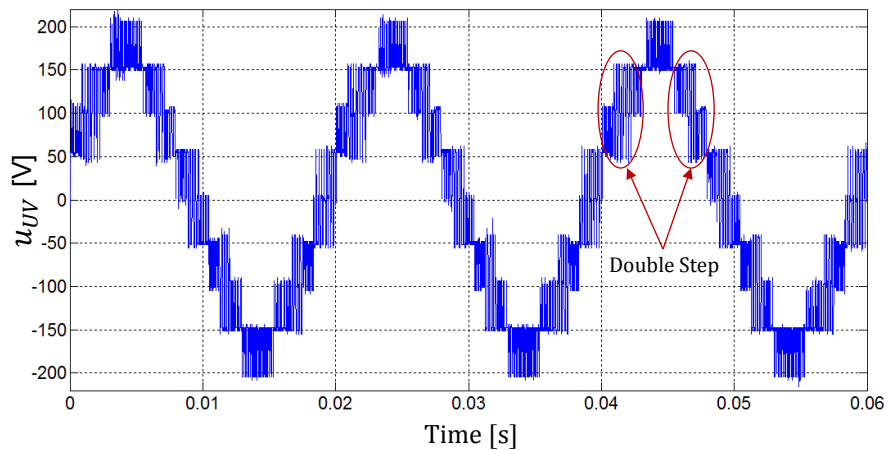
Figure 52 (a) shows line to line voltage u_{UV} at the output of the inverter without phase shift to the carrier signals among the phases and without zero sequence voltage injection. Figure 52 (b) shows the output voltage u_{UV} with phase shift to the carrier signals among the phases but with zero sequence voltage injection while Figure 52 (c) shows the output voltage u_{UV} with phase shift to the carrier signals among the phases as well as the zero sequence voltage injection method is used. The double-step voltage is reduced in the figure (b) and more improvement is achieved in figure (c).



(a) Without phase shift of the carrier signals among the phases and without zero sequence voltage injection



(b) With phase shift of the carrier signals among the phases and without zero sequence voltage injection



(c) With phase shift of the carrier signals among the phases and with zero sequence voltage injection

Figure 52 Line to line voltage at the output of the inverter by using PS-PWM

4.4 Steady state operation of the hybrid system

4.4.1 Performance of the QPLL

Figure 53 illustrates the performance of the QPLL. Figure 53 (a) shows the grid voltages frame u_α and u_β in the α - β coordinates. At $t = 0,015s$ the system is connected to the grid. The QPLL starts the calculation of the grid reference angle θ as shown in Figure 53 (b). The orientation to the grid voltage is achieved within one of system frequency period where the control error v_D was reduced to almost zero at $t = 0,035s$ as shown in Figure 53 (c).

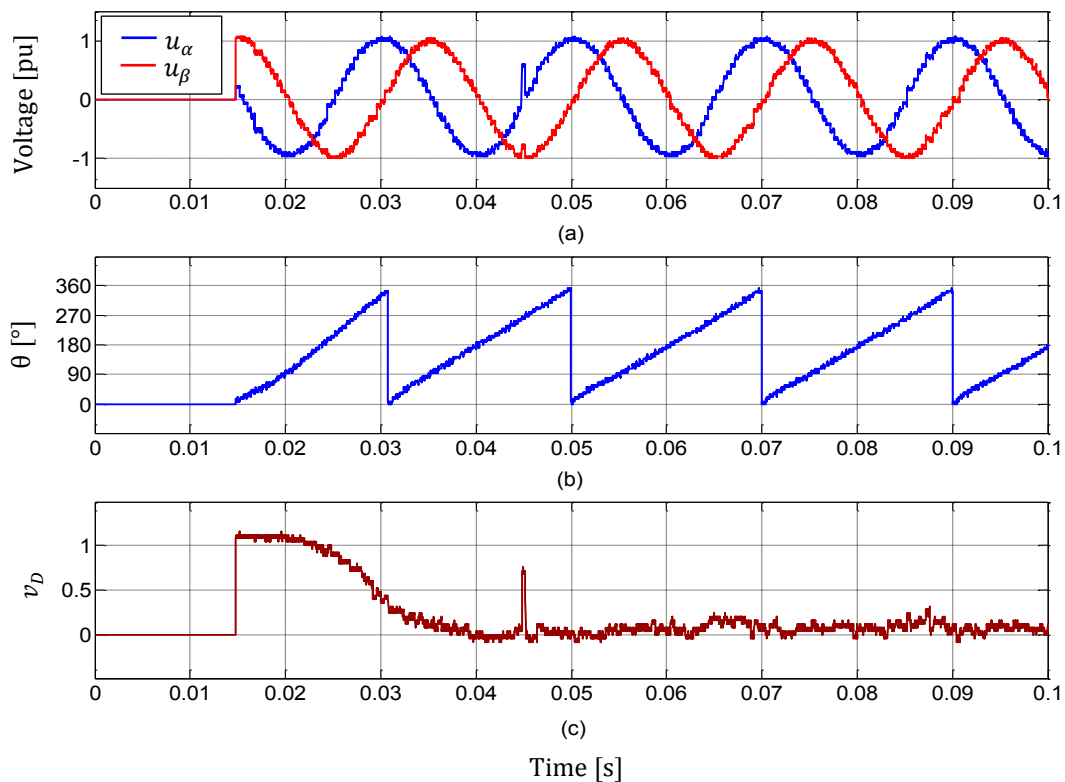


Figure 53 QPLL performance (a) Grid voltage in α - β coordinates (b) Reference angle of the grid voltage (c) Control error v_D (see Figure 35)

4.4.2 Performance of the per-phase and the per-cell compensation

The performance of the two types of compensation, the *per-phase compensation* and the *per-cell compensation*, that were discussed in the previous sections were examined in the laboratory. If all HB cells of the inverter work with the same DC-link voltage and produce the same power, the compensation is not active, thus the reference voltages are not modified and directly sent to the modulator.

However, if the DC-link voltages of all HB cells are equal but the power produced by the upper layer cells of the inverter ($HB - U1, HB - V1$ and $HB - W1$) are different than the power produced by the lower layer cells ($HB - U2, HB - V2$ and $HB - W2$), only the *per-cell compensation* is applied to the reference voltages and balanced power is injected to the grid.

If the DC-link voltages of the upper layer cells of the inverter are different from the lower layer DC-link voltages as it is the case in the current hybrid setup, the *per-cell compensation* will become active for the whole time regardless of the symmetrical power situation.

The unsymmetrical power produced by different cells in the same phase, leads to unbalance in the power injected to the grid. In this case, both types of the compensation will work to redistribute the power between the two cells in the same phase and rebalance the injected power to the grid.

For the sake of simplicity, in the experimental setup, the PV panel temperature is considered to be constant and the wind turbine only works in the MPP region. As explained above, the rated DC voltages of the PV generator busses at the MPP were set to 60V and the rated power produced by each PV generator was set to 360W. The rated DC voltage of each WT generator bus was set to 70V and the each generator produces a rated power of 315W at the MPP. The grid line to line voltage U_{L1L2} at the secondary side of the isolation transformer was set to 80V, so that a minimum DC-link voltage of 66V is required to inject power to the grid. The setup was designed for a total rated power injected to the grid P_{Total} of 1800W. Based on these considerations,

the behavior of the grid integration of the hybrid PV-WT system was experimentally examined in three different modes of operation according to Table 1 which was already discussed in 3.2.3:

- Mode 9: Rated PV-Power and Rated WT-Power

In this mode of operation, the *WT* generators are operated emulating a rated wind speed $v_{w,(rated)}$ and produce the rated power. In this scenario, the effectiveness of the feedforward compensation was tested by considering the changes in the power produced by the *PV* generators in three different cases of operation:

Case 1

Balanced operation: all the *PV* generators for cell *U1*, *V1* and *W1* produce their rated power at the maximum power point with emulated rated sun irradiance of $S_{IR,(rated)} = 1000 \text{ W/m}^2$.

Case 2

Single cell unbalanced operation: the power produced by cell *U1* is reduced to 30% of its rated power due to the emulated reduction in the sun irradiance to the minimum value ($S_{IR,(min)} = 300 \text{ W/m}^2$) as a result of partial shading to the *PV* generator of cell *U1*, while the power produced by *HB* cells *V1* and *W1* stay at the rated value.

Case 3

Double cell unbalanced operation: the power produced by cell *U1* and *V1* are both reduced to 30% of the rated power due to the emulated reduction in the sun irradiance to the minimum value $S_{IR,(min)}$. The power produced by cell *W1* stays at the rated value.

- Mode 8: Minimum PV-Power and Rated WT-Power

In this mode of operation the power produced by the upper layer HB cells $U1, V1$ and $W1$ are all set to 30% of the rated power due to the reduction in the emulated sun irradiance to $S_{IR,(min)}$. The cells stay working in the maximum power point. The WT generators work at rated wind speed and produce the rated power.

- Mode 7: Rated PV-Power and Minimum WT-Power

In this mode of operation the power produced by all the PV generators is at the rated value and the cells work at the maximum power point while the power produced by WT generators is reduced to 38% of the rated power due to the emulated reduction in the wind speed to the minimum value $v_{w,(min)}$. The lower layer cells stay working in the maximum power point region.

Table 3 shows the generated voltages and the power produced by each HB cell as well as the total power injected to the grid for different cases and different modes of operation.

Table 3 the power generation and injection for the different modes of operation

Power calculations					
Values	Mode 9 Case 1	Mode 9 Case 2	Mode 9 Case 3	Mode 8	Mode 7
$U_{DC-HB U1}$ (V)	60	57	57	57	60
$U_{DC-HB V1}$ (V)	60	60	57	57	60
$U_{DC-HB W1}$ (V)	60	60	60	57	60
$U_{DC-HB U2}$ (V)	70	70	70	70	50
$U_{DC-HB V2}$ (V)	70	70	70	70	50
$U_{DC-HB W2}$ (V)	70	70	70	70	50
$I_{DC-HB U1}$ (A)	6	1,9	1,9	1,9	6
$I_{DC-HB V1}$ (A)	6	6	1,9	1,9	6
$I_{DC-HB W1}$ (A)	6	6	6	1,9	6
$I_{DC-HB U2}$ (A)	4,5	4,5	4,5	4,5	2,4
$I_{DC-HB V2}$ (A)	4,5	4,5	4,5	4,5	2,4
$I_{DC-HB W2}$ (A)	4,5	4,5	4,5	4,5	2,4
$P_{DC-HB U1}$ (W)	360	110	110	110	360
$P_{DC-HB V1}$ (W)	360	360	110	110	360
$P_{DC-HB W1}$ (W)	360	360	360	110	360
$P_{DC-HB U2}$ (W)	315	315	315	315	120
$P_{DC-HB V2}$ (W)	315	315	315	315	120
$P_{DC-HB W2}$ (W)	315	315	315	315	120
Total power generated by PV (W)	1080	830	580	330	1080
Total power generated by WT (W)	945	945	945	945	360
Total power generated (W)	2029	1772	1521	1275	1438
Total power injection (W)	1800	1593	1386	1178	1316
Total power losses (W)	228	178,5	135	98	122
Inverter line current I_U (A)	13	11,5	10	8,5	9,5
Reduction in the total power	0 %	12,7%	25 %	37,1 %	29,1 %

4.4.3 Simulation and experimental results in balanced operation

Since the experimental results focus on the compensation process, the results of the balanced operation (mode 9 / case 1) will be the reference for the other cases and modes. Figure 54 shows the reference voltages $u_{ref U}$, $u_{ref V}$ and $u_{ref W}$ sent to the compensation stage as the output of the current controller loop. The green triangle signal corresponds to the zero sequence injection voltage u_{zero} . Figure 55 shows the reference voltages resulting from the *per-phase compensation* unit. It is clear that the *min-max* of the zero sequence voltage is kept unchanged because there is no unbalance.

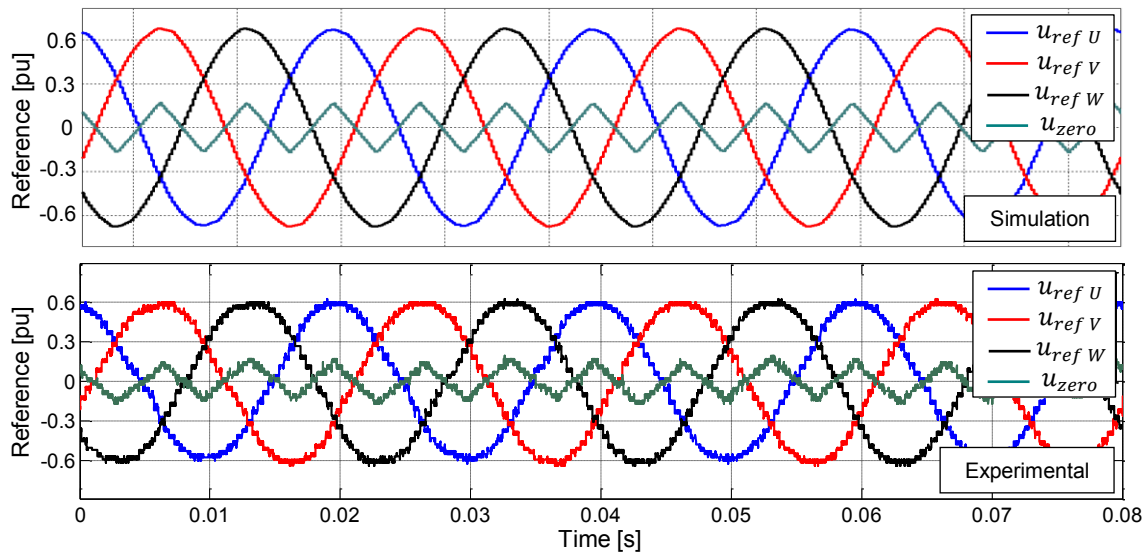


Figure 54 Reference voltages before *per-phase compensation* for mode 9 / case 1

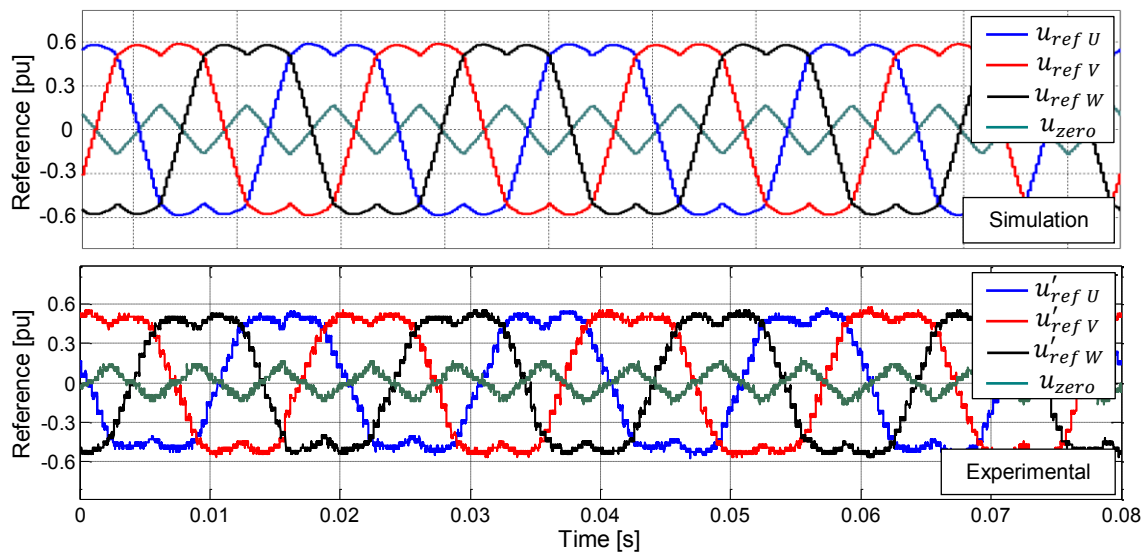


Figure 55 Reference voltages after *per-phase compensation* for mode 9 / case 1

Figure 56 shows the reference voltage of phase U where the signal in the black color is the reference voltage $u'_{ref U}$ before *per-cell compensation*. The one in the blue is the reference voltage $u''_{ref U1}$ of HB cell $U1$ and the one in red is the reference voltages $u''_{ref U2}$ of HB cell $U2$ after compensation. The compensation process slightly increase the modulation index of the cell $U2$ from 0,57 to 0,6 because cell $U2$ has a higher DC-link voltage 80V and injects lower power of 315W while cell $U1$ has a lower DC-link voltage of 60V and higher power injected to the grid (360W) so that the compensator increase the modulation index of the reference voltage for cell $U1$ to 0,75.

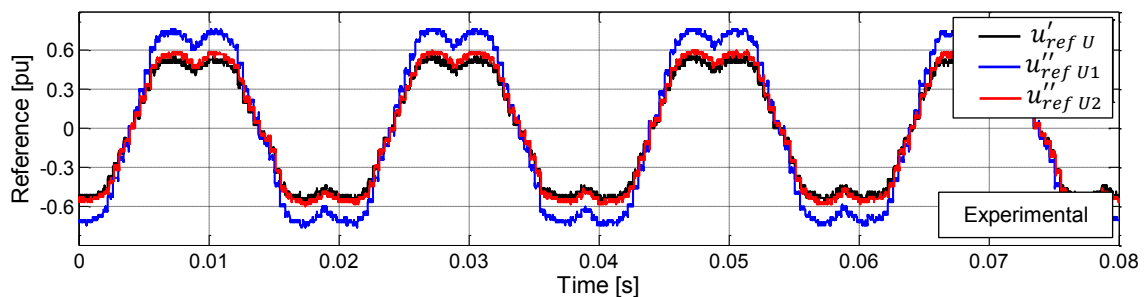


Figure 56 Reference voltage of phase U before and after *per-cell compensation* for mode 9 / case 1

Figure 57 shows the rated inverter line currents injected to the grid. The current is 13A RMS and is balanced in all phases. Figure 58 show the phase voltages of the inverter and their fundamental.

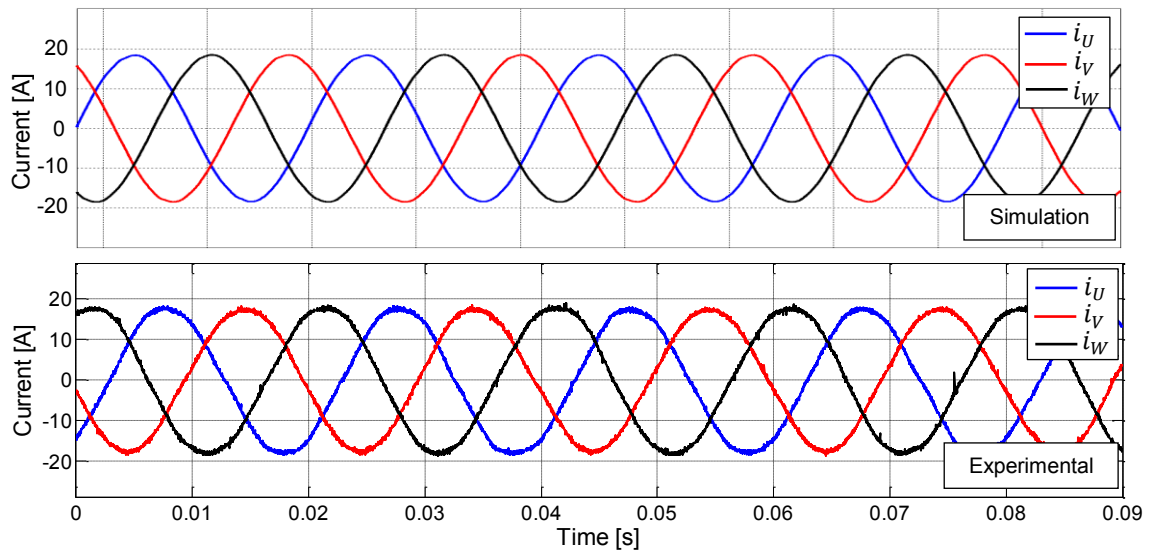


Figure 57 Inverter currents injected to the grid for mode 9 / case 1

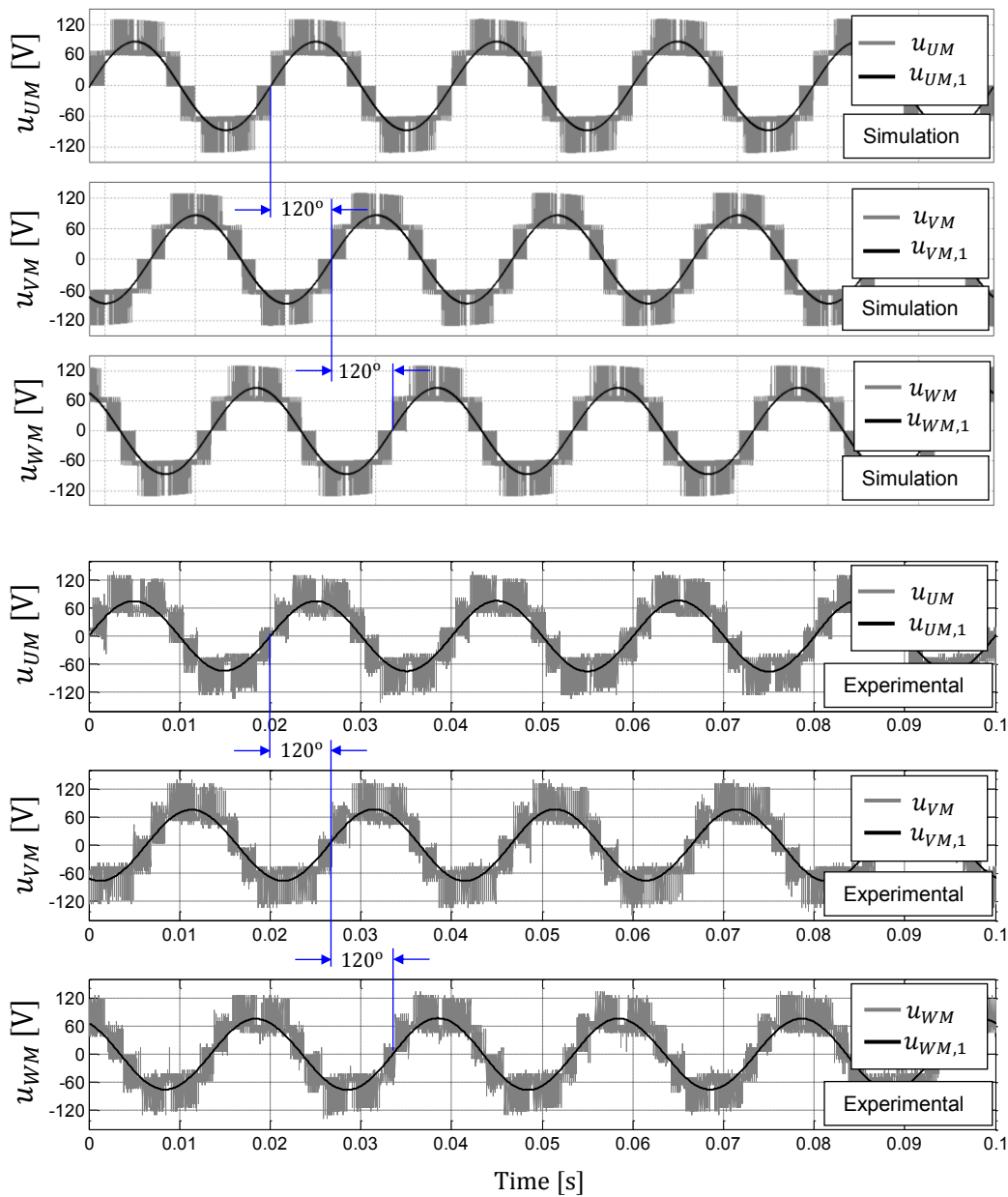


Figure 58 Inverter phase voltages and their fundamentals for mode 9 / case 1

Figure 59 shows the inverter line to line voltages. Figure 60 shows that the currents were injected to the grid with almost unity power factor. In this figure the blue lines represent the grid phase voltages u_{L1N} , u_{L2N} and u_{L3N} while the red lines represent the corresponding inverter line currents i_U , i_V and i_W .

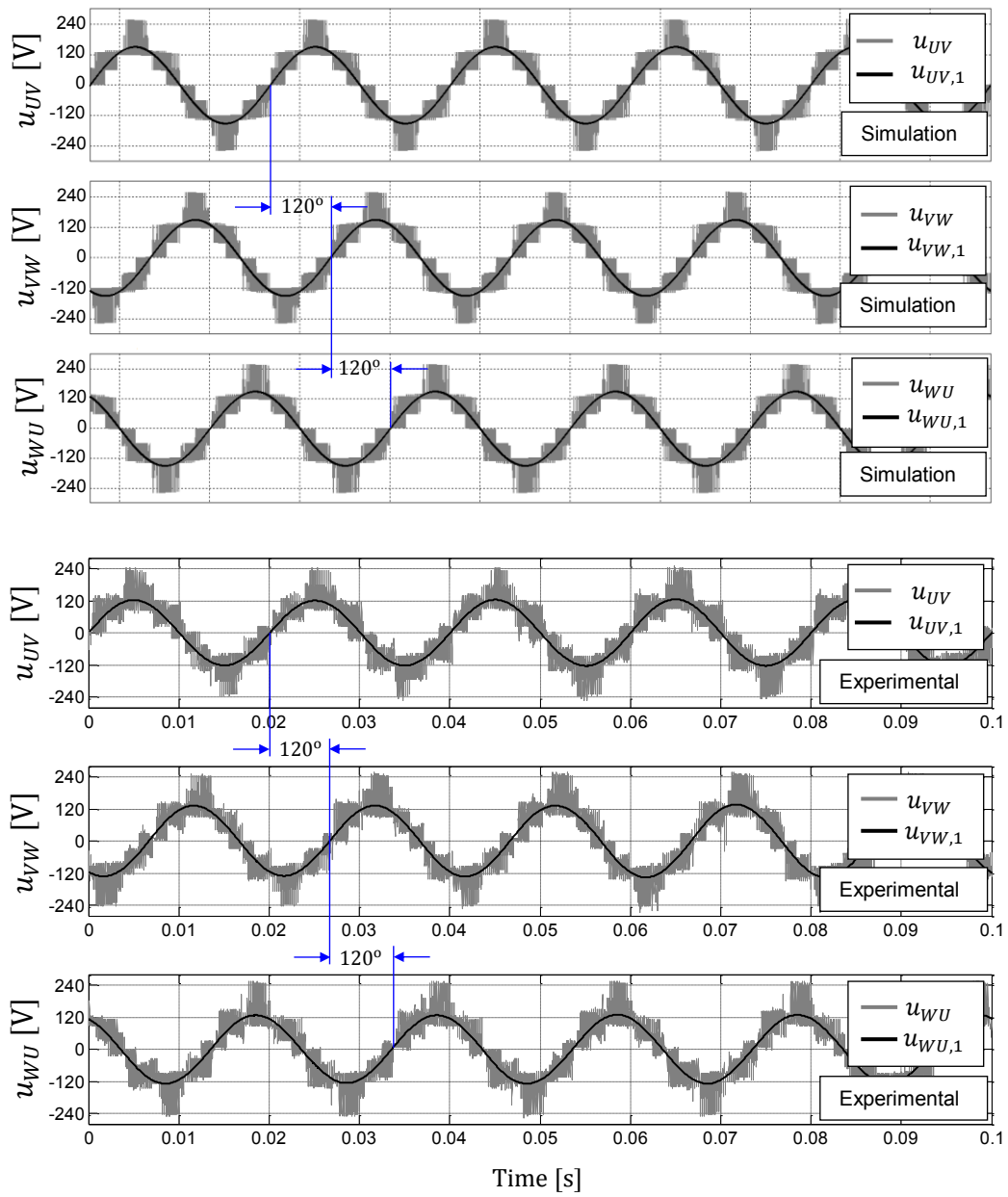


Figure 59 Inverter line to line voltages and their fundamentals for mode 9 / case 1

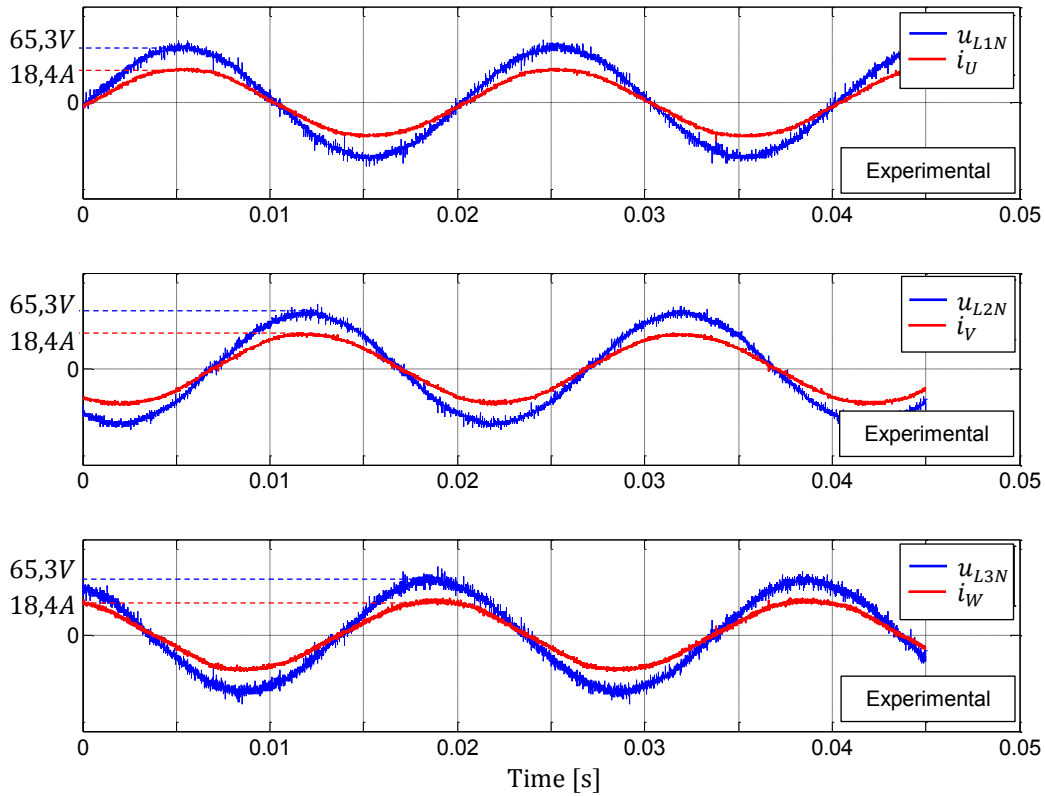


Figure 60 Grid phase voltages and the corresponding currents at unity power factor for mode 9 / case 1

4.4.4 Simulation and experimental results in single cell unbalanced operation

In mode of operation 9 case 2 according to Table 3 the unbalanced operation occurs due to the reduction in the power produced by HB cell $U1$ from $360W$ to $110W$. The reference voltages before the compensation process $u_{ref U}$, $u_{ref V}$ and $u_{ref W}$ are almost symmetrical with amplitude of 0,7 as shown in Figure 61. In Figure 62 the reference voltages $u'_{ref U}$, $u'_{ref V}$ and $u'_{ref W}$ after the *per-phase compensation* and the *min-max* of the zero sequence are shown. The *min-max* sequence is changed here in order to compensate the difference between the power processed by the phases (p_U , p_V and p_W) and the average power p_{av} . Because of phase U is generating less power, the zero sequence signal u_{zero} is in phase with its reference voltage $u_{ref U}$. This becomes obvious for the phases V and W , which are modified to redistribute the

power and increase the current in phase U . Now, in relation with the redistribution of the power delivered by the cells of phase U , Figure 63 clearly shows how the amplitude of each cell voltage reference is modified in order to redistribute the ON/OFF times of the cell accordingly with the produced power which ensures that the PV generator of HB cell $U1$ keeps working at the maximum power point. As it is shown in Figure 63 (a), the reference for the cell $U1$ has dropped to 0,3 approximately, because its radiation has dropped to 30% of the rated value. Figure 63 (b and c) show the reference voltages before and after *per-cell compensation* for phase V and W respectively. It is clear that the amplitude of each cell voltage reference is modified while the ratio between the reference voltage for the upper cells ($u''_{ref V1}, u''_{ref W1}$) and the lower cells ($u''_{ref V2}, u''_{ref W2}$) are kept constant in order to compensate the reduction in the total power of phase U which leads to the rebalance of the injection of the power to the grid.

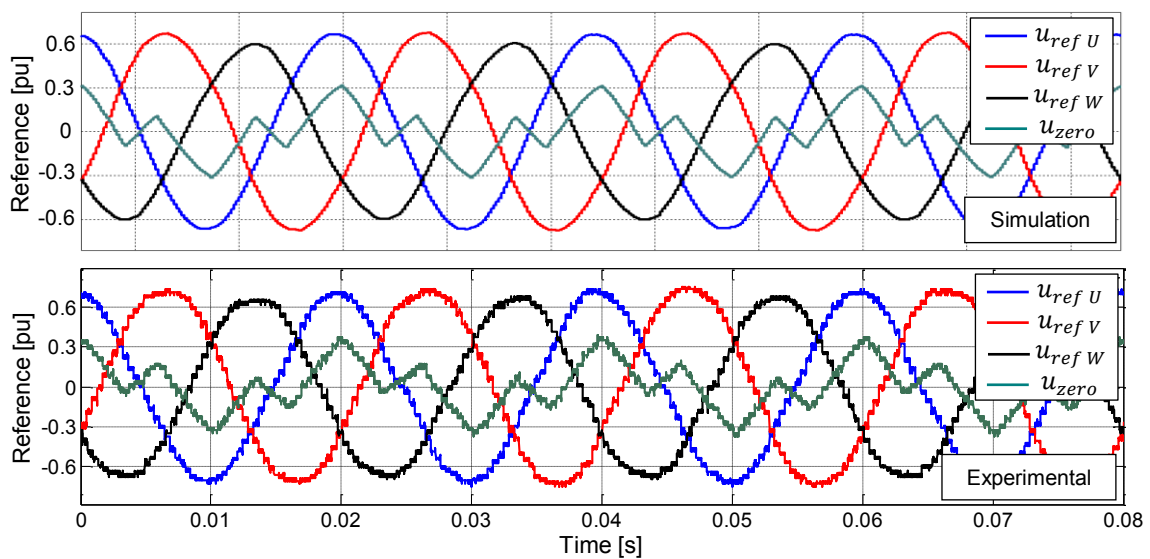


Figure 61 Reference voltages before *per-phase compensation* for mode 9 / case 2

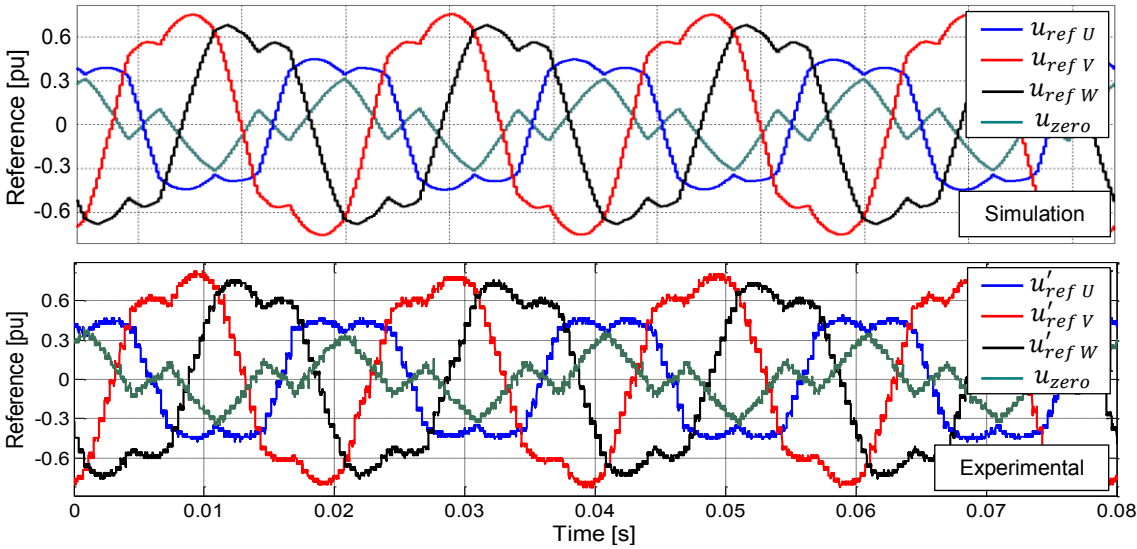


Figure 62 Reference voltages after *per-phase compensation* for mode 9 / case 2

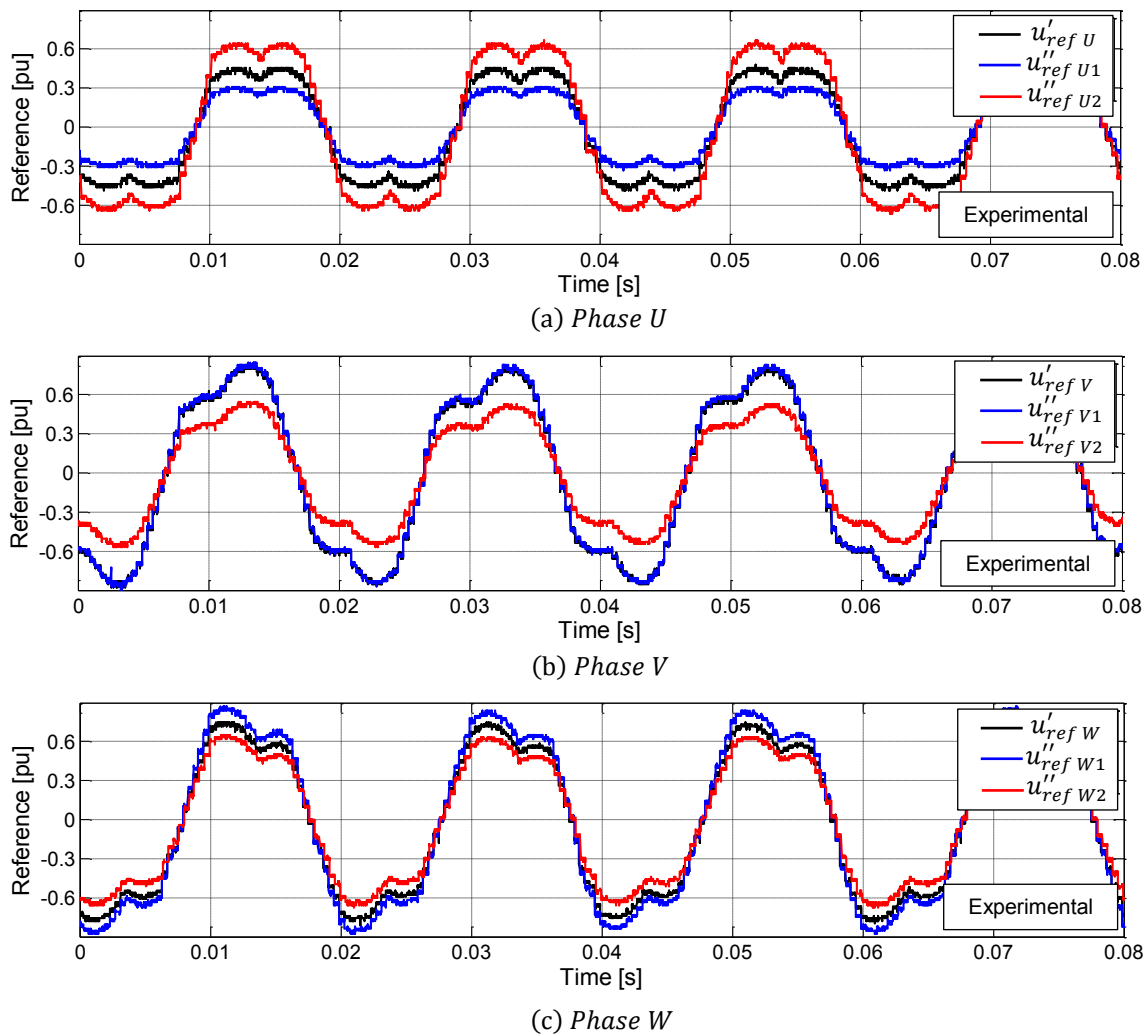


Figure 63 Reference voltages before and after *per-cell compensation* for mode 9 / case 2

Figure 64 shows the inverter line currents injected to the grid under unbalanced operation condition. From the figure it is clear that the currents remain balanced and exhibit a RMS value of 11,5A which is lower than the rated value in case1 because the total injected power has dropped to 1593W due to the reduction in the power production of phase *U*. Working at low modulation index leads to a reduction in the number of output voltage level as shown in Figure 65. From the figure it can be seen that the number of levels of phase *U* is reduced to 3-levels while the other phases keep working in 5-level mode. Moreover, the inverter phase voltages are unbalanced in amplitude and phase. As shown in the previous figure, the fundamental components

$u_{UM,1}$, $u_{VM,1}$ and $u_{WM,1}$ of the inverter phase voltages have different amplitudes and different phase shift among them.

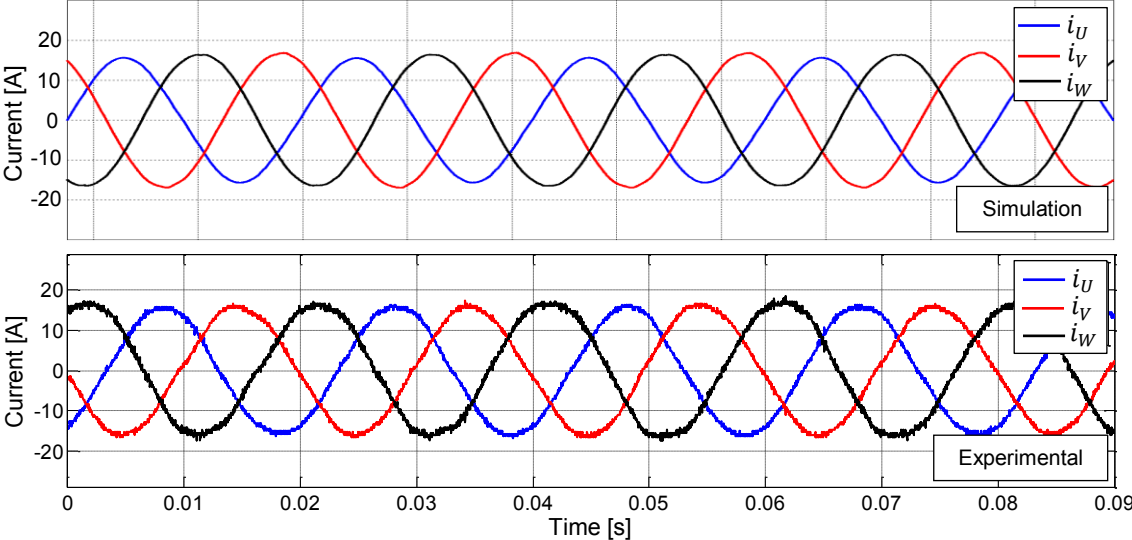


Figure 64 Inverter currents injected to the grid for mode 9 / case 2

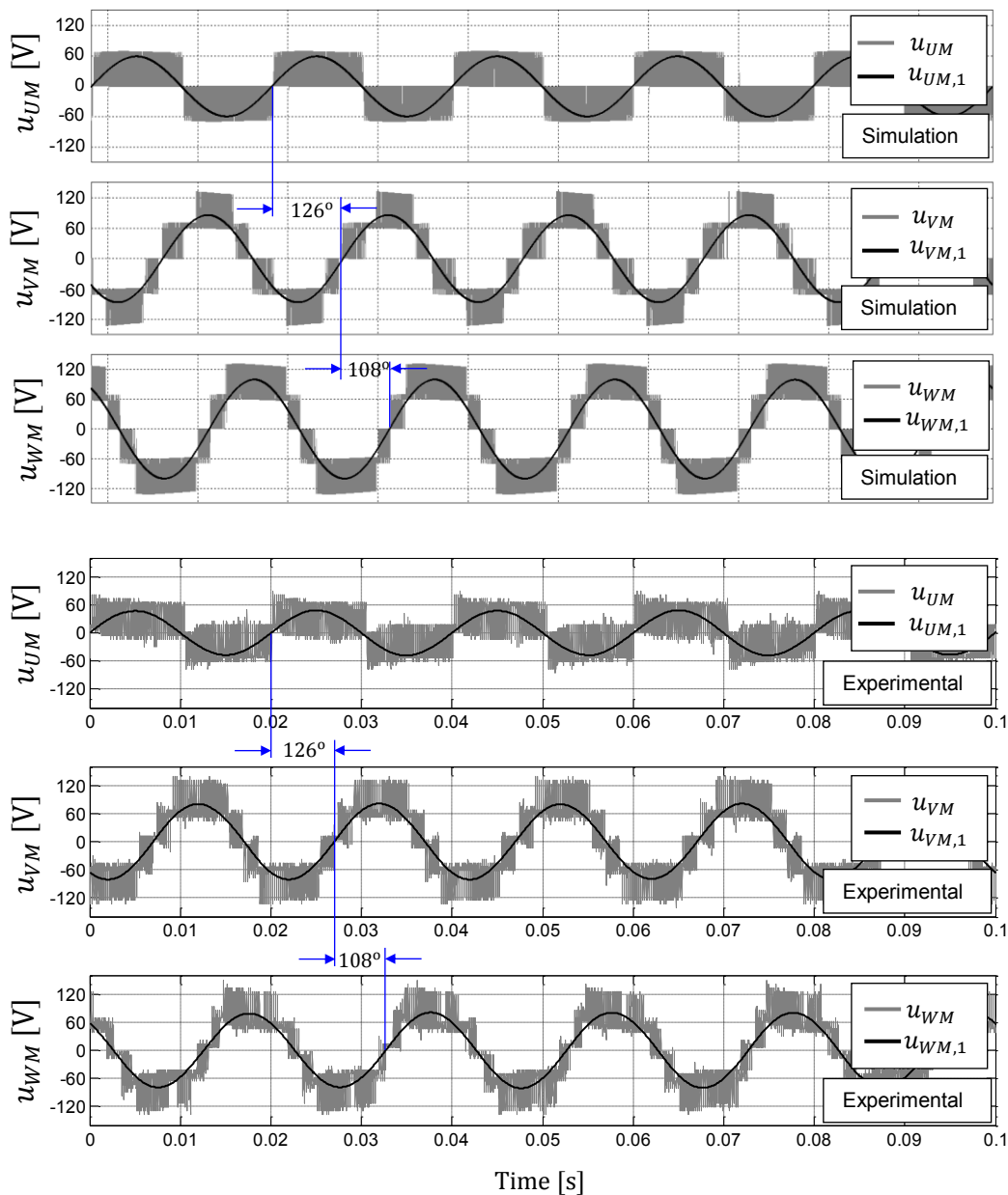


Figure 65 Inverter phase voltages and their fundamentals for mode 9 / case 2

The performance of the modulation index compensation becomes obvious in the results of Figure 66 with the inverter line to line voltages. The fundamental harmonics of the line to line voltages $u_{UV,1}$, $u_{VW,1}$ and $u_{WU,1}$ remain balanced in the amplitude and phase because the neutral point was shifted in the direction that allows the inverter to balance the line voltages. The unsymmetrical operation of the current controller keeps the injection of the power at unity power factor as shown in Figure 67.

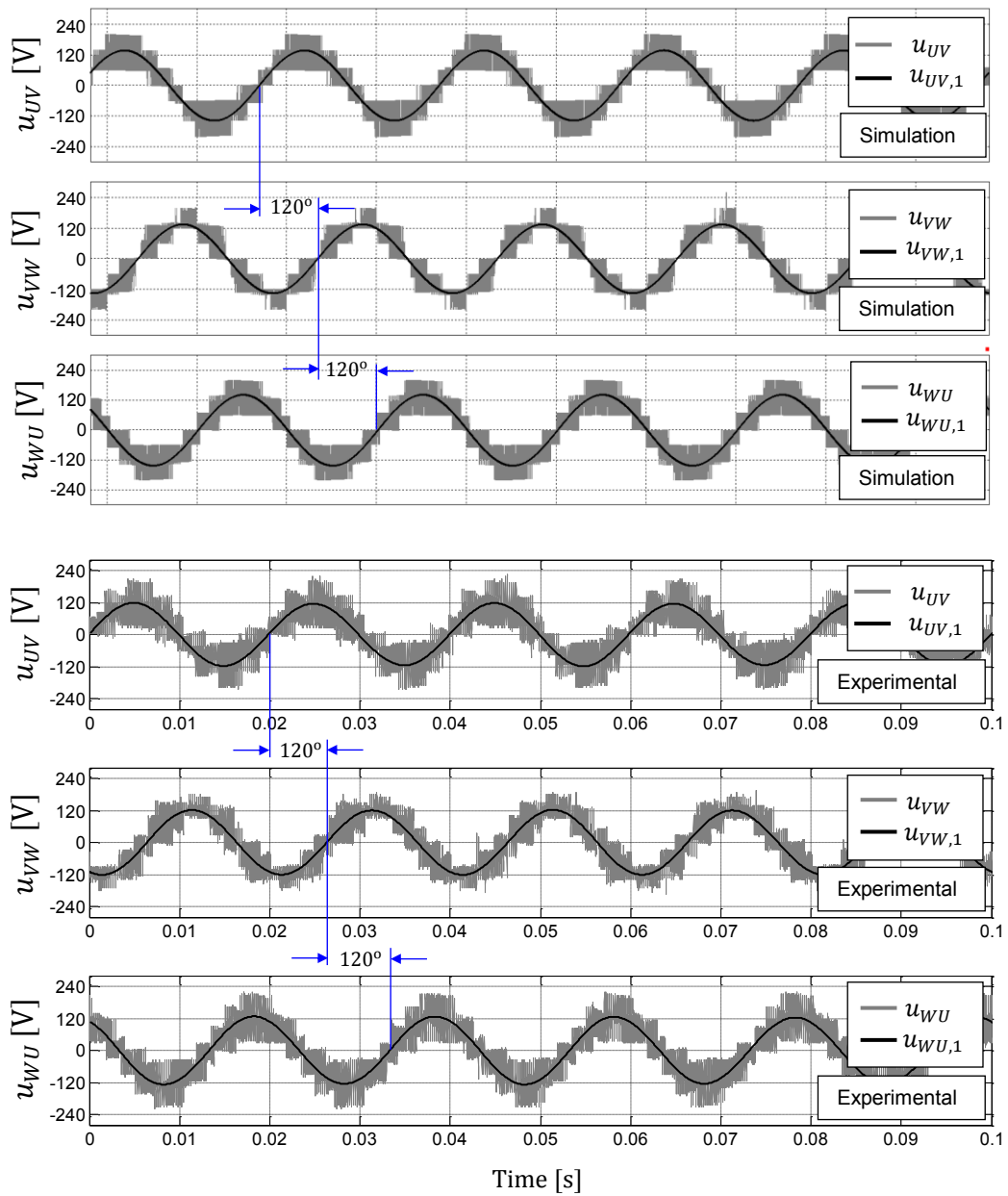


Figure 66 Inverter line to line voltages and their fundamentals for mode 9 / case 2

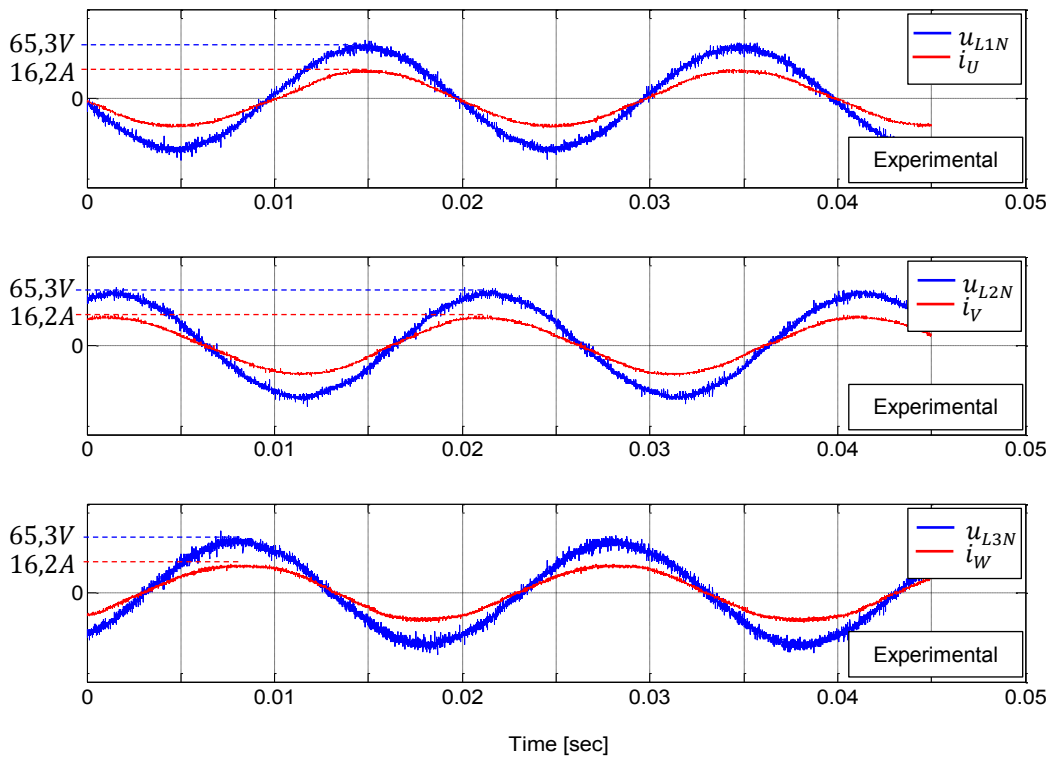


Figure 67 Grid phase voltages and the corresponding currents at unity power factor for mode 9 / case 2

4.4.5 Simulation and experimental results for two cell unbalanced operation

In the mode 9 of operation, case 3 according to Table 3, the unbalance occurs due to the reduction in the power produced by HB cell $U1$ and $U2$ from $360W$ to $110W$. The reference voltages before the compensation process stay symmetrical as shown in Figure 68. In Figure 69 the reference voltages after the per-phase compensation are shown. Like in case 2 above, the *min-max* of the zero sequence u_{zero} is modified in order to achieve the *per-phase compensation* due to the difference between the power produced in the phases. However, in this case both phase U and V are producing less power and the zero sequence signal u_{zero} is 180° out of phase with the reference voltage of phase W . From Figure 70 (c), it becomes obvious that the reference voltage of phases W is modified to redistribute the power and to increase the current in both phase U and V . Figure 70 (a and b) illustrates the modification in the reference

voltages in order to perform the redistribution of the power delivered by the cells of phase U and phase V respectively. In both phases the amplitude of each cell voltage reference is modified in order to redistribute the ON/OFF times of the cell according with the produced power which ensures that the PV generators of HB cell $U1$ and $V1$ keep working at their maximum power point.

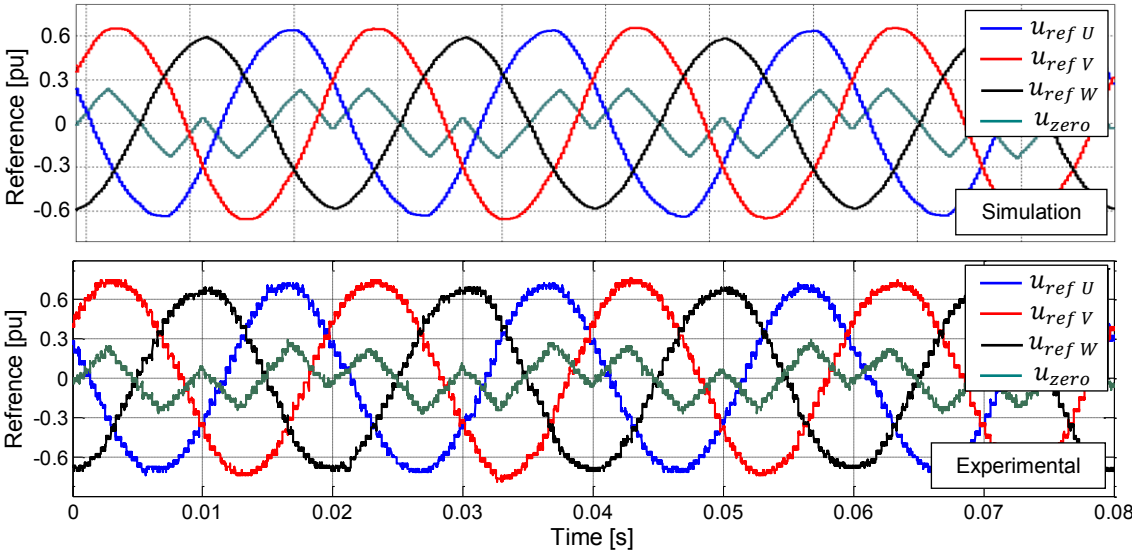


Figure 68 Reference voltages before *per-phase compensation* for mode 9 / case 3

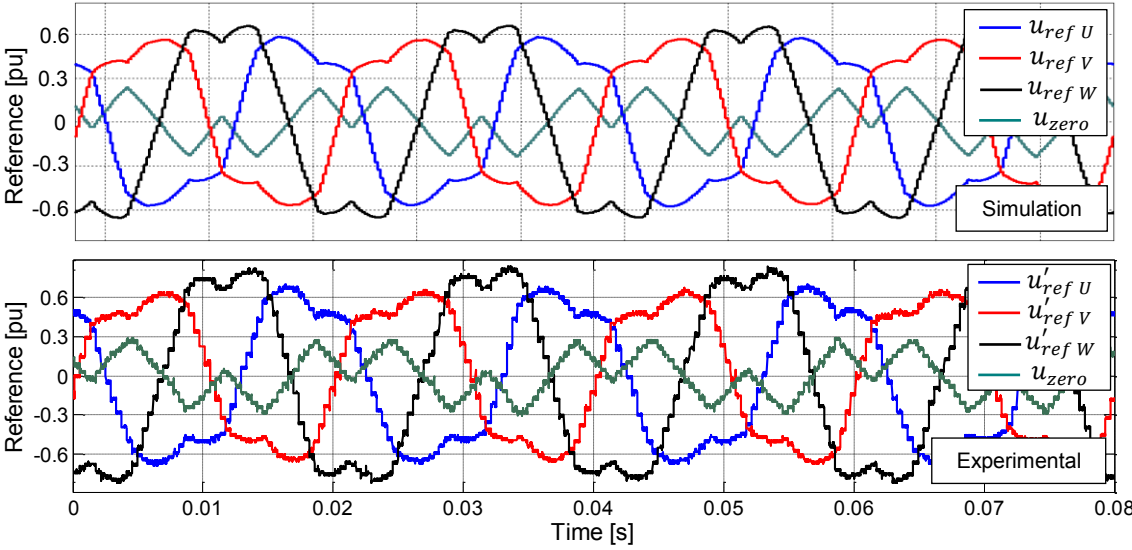


Figure 69 Reference voltages after *per-phase compensation* for mode 9 / case 3

As shown in Figure 70 (a) the reference for the cell $U1$ has dropped to 0,3 approximately, because its radiation has dropped to 30% of its rated value. The same reduction is done for cell $V1$ as shown in Figure 70 (b).

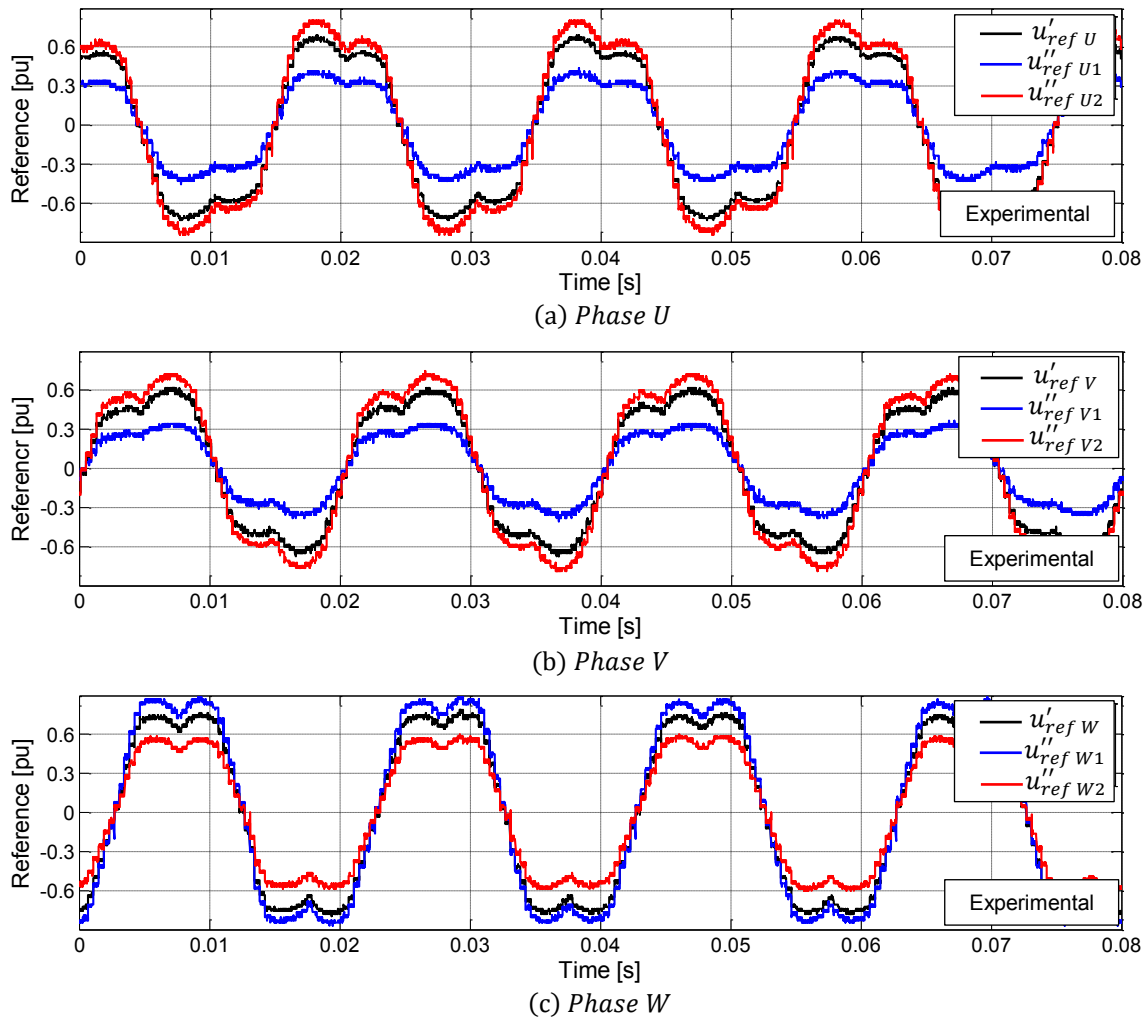


Figure 70 Reference voltages before and after *per-cell compensation* for mode 9 / case 3

Figure 71 shows the inverter line currents injected to the grid. The currents are balanced and have a RMS value of 10A which is lower than the rated currents in case 1 and the currents in case 2 because the total injected power have dropped to 1386W due to the reduction in the power production of phase U and phase V . Figure 72 shows the inverter phase voltages. Like in the previous case, the fundamental components ($u_{UM,1}$, $u_{VM,1}$ and $u_{WM,1}$) of the phase voltages of the inverter have different

amplitudes and different phase shift among them, while the line voltages are balanced as shown in Figure 73. The fundamental of the line voltages $u_{UV,1}$, $u_{VW,1}$ and $u_{WU,1}$ remain balanced in amplitude and phase due to the shift of the neutral point in the direction that leads to resynthesize balanced line voltages.

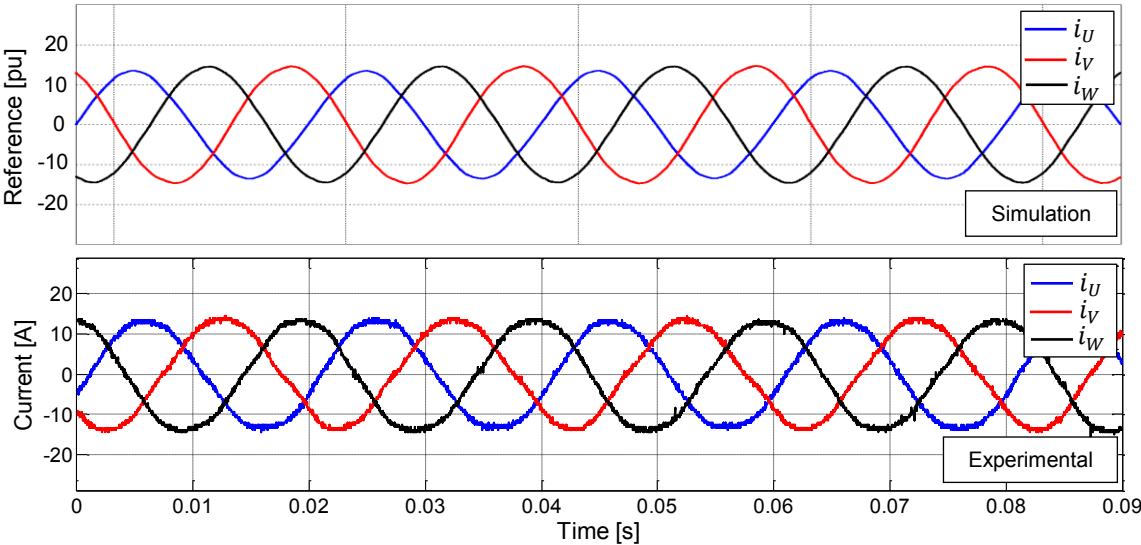


Figure 71 Inverter currents injected to the grid for mode 9 / case 3

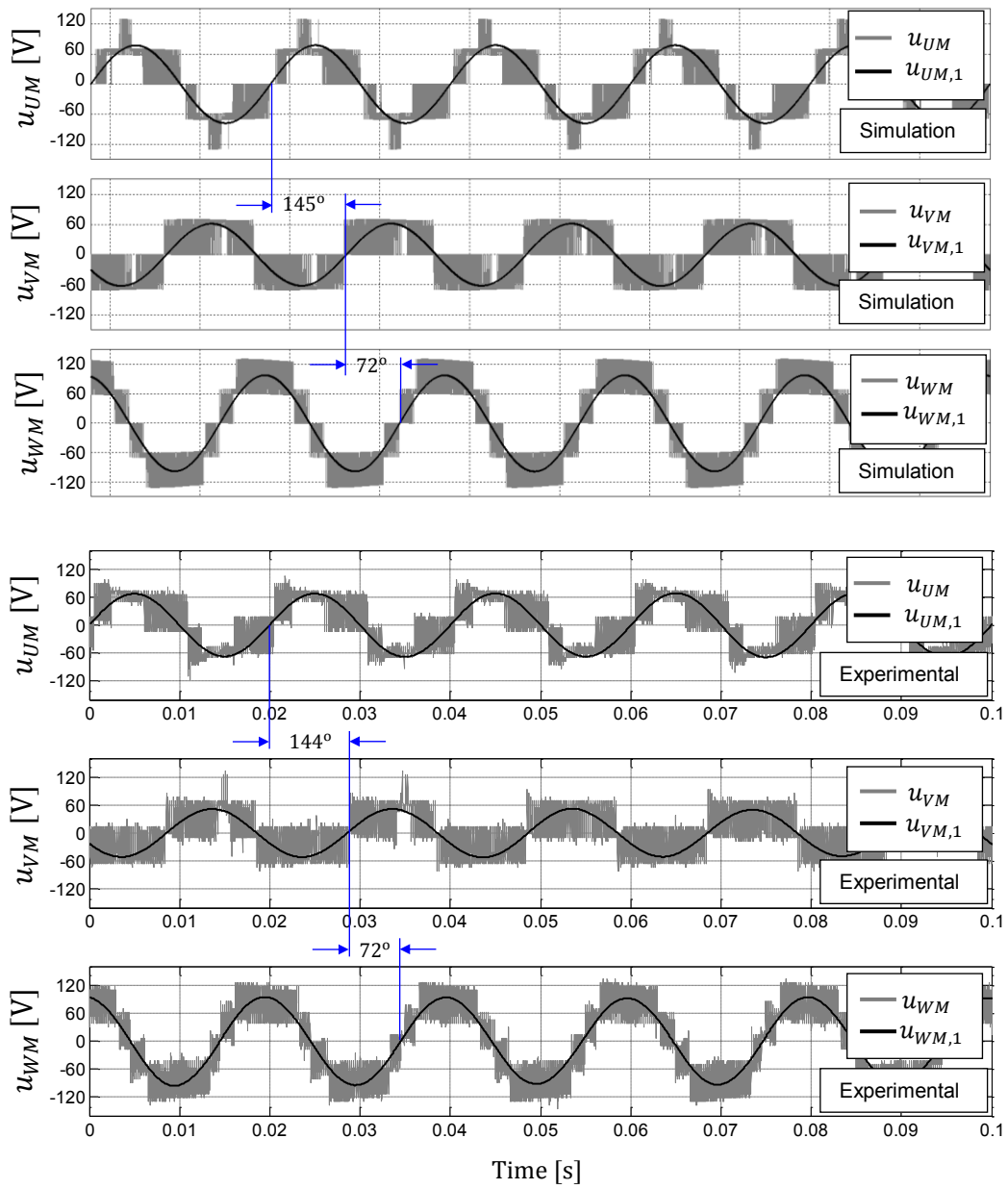


Figure 72 Inverter phase voltages and their fundamentals for mode 9 / case 3

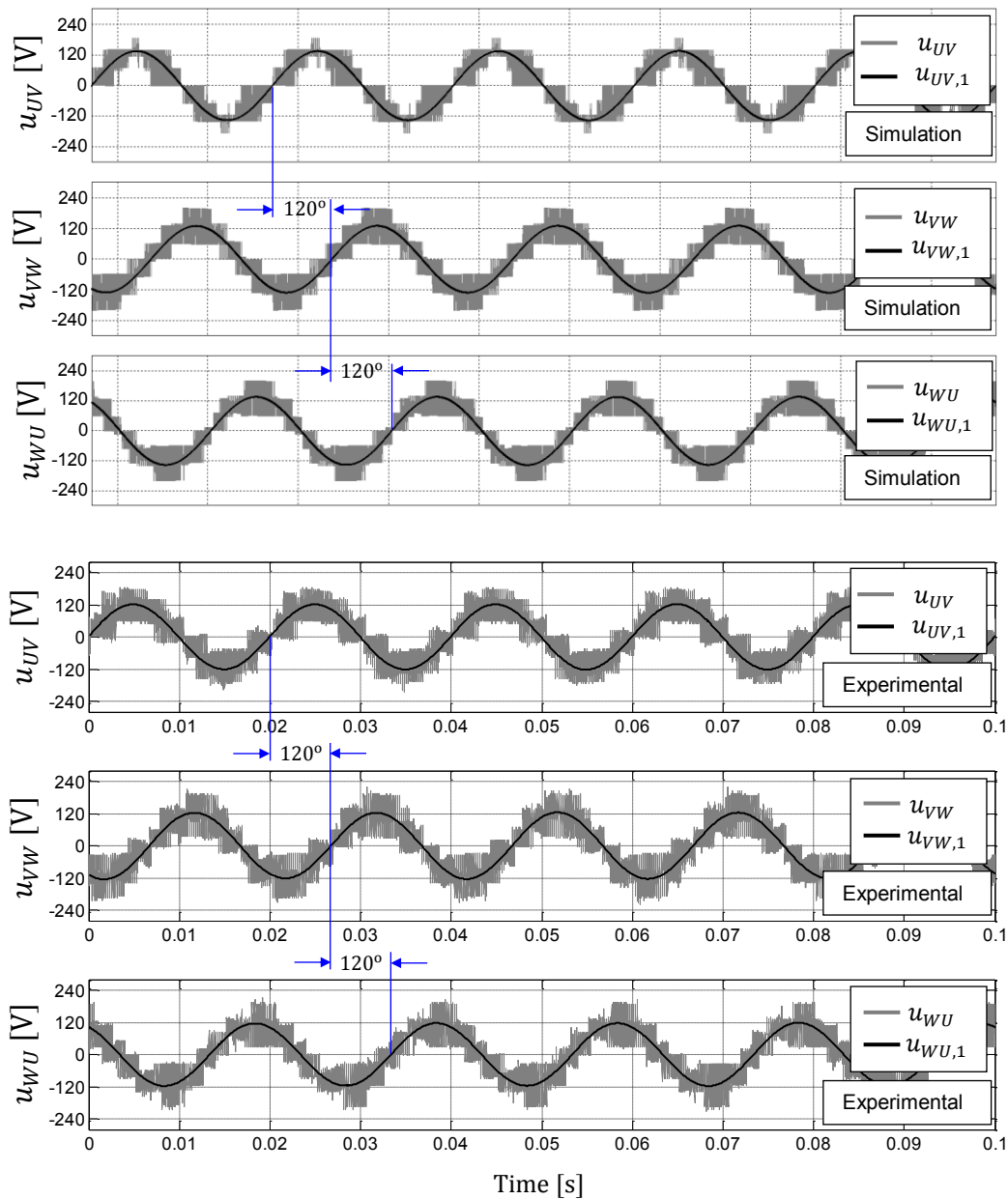


Figure 73 Inverter line to line voltages and their fundamentals for mode 9 / case 3

4.4.6 Experimental results at minimum PV-power and rated WT-power

In the mode 8 of operation according to Table 3, the power produced by the phases is equal. Yet an unsymmetrical operation occurs due to the reduction in the power produced by the H-bridges of the upper layer cells $U1, V1$ and $W1$ from $360W$ to $110W$. The reference voltages $u_{ref U}, u_{ref V}$ and $u_{ref W}$ before the

compensation process are symmetrical with amplitude of 0,7 as shown in Figure 74. In Figure 75 the reference voltages $u'_{ref U}$, $u'_{ref V}$ and $u'_{ref W}$ after the *per-phase compensation* and the *min-max* of the zero sequence u_{zero} are shown. Like in the mode 9 of operation / case 1 presented above, the *min-max* of the zero sequence is kept unchanged deactivating the *per-phase compensation* because there is no difference in the power produced in the phases. Figure 76 illustrates the modification in the reference voltage of phase *U* due to the *per-cell compensation* in order to perform the redistribution of the power delivered by the upper layer and the lower layer cells of the inverter. In all phases the amplitude of each cell voltage reference is modified in order to redistribute the *ON/OFF* times of the cell accordingly with the produced power which ensures that the PV generators of the upper layer HB cells keep working at their maximum power point. As shown in Figure 76 the reference voltage $u''_{ref U1}$ for the cell *U1* drops to 0,3 approximately, because its radiation has become 30% of its rated value. The same reduction is done for cell *V1* and *W1*, while the reference voltage $u''_{ref U2}$ of the cell *U2* has been increased to 0,7 approximately in order to compensate the drop in the voltage of the upper layer cells. The same increment is done for cell *V2* and *W2*

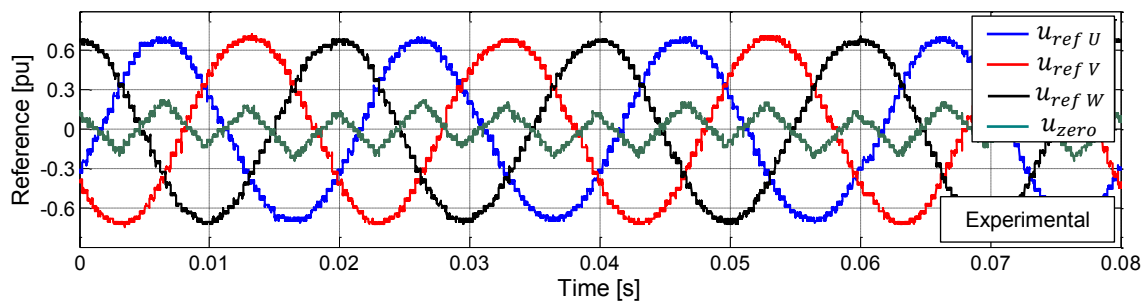


Figure 74 Reference voltages before *per-phase compensation* for mode 8

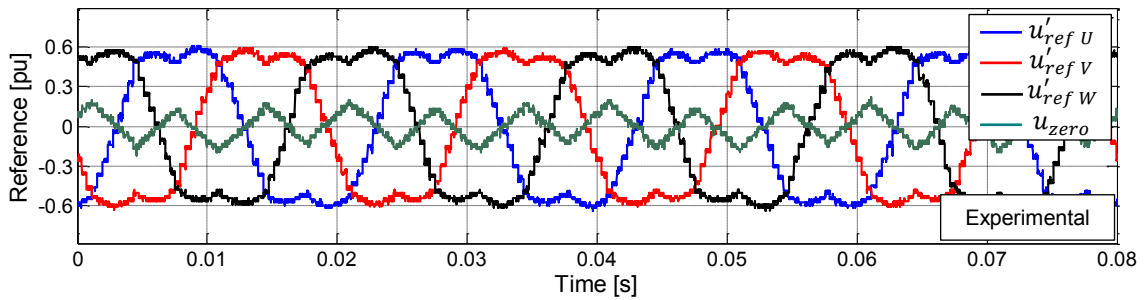


Figure 75 Reference voltages after *per-phase compensation* for mode 8

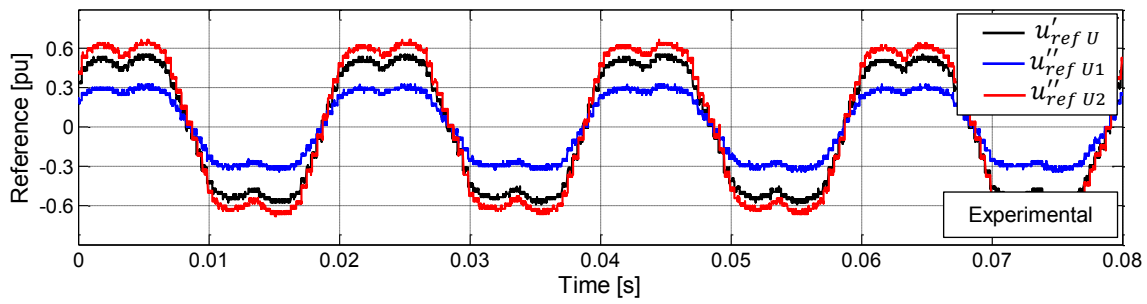


Figure 76 Reference voltage of phase *U* before and after *per-cell compensation* for mode 8

Figure 77 shows the inverter line currents injected to the grid. It is clear that the currents are almost balanced and exhibit a RMS value of 8,5A which is lower than the currents in mode 9 because the total injected power is now 1178W due to the reduction in the power production in the all PV generators to their minimum values. Figure 78 shows the inverter phase voltages. In this case the fundamental components of the inverter phase voltages are balanced because there is no unbalanced power production among the phases of the inverter, thus the neutral point of the inverter remains in the origin. Figure 79 shows the balanced inverter line to line voltages and their fundamental harmonics.

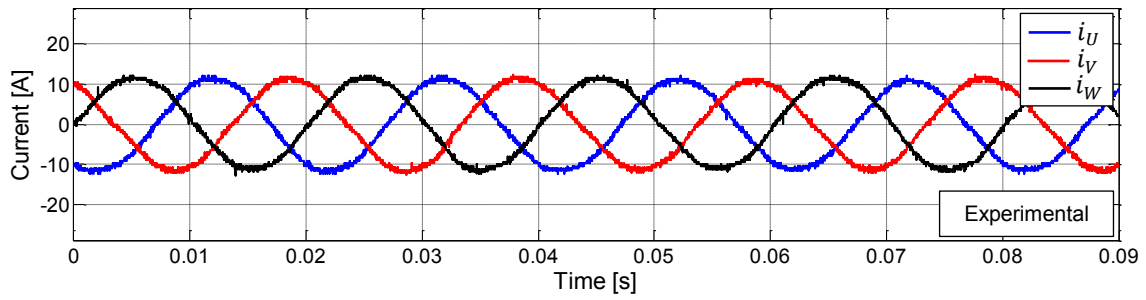


Figure 77 Inverter currents injected to the grid for mode 8

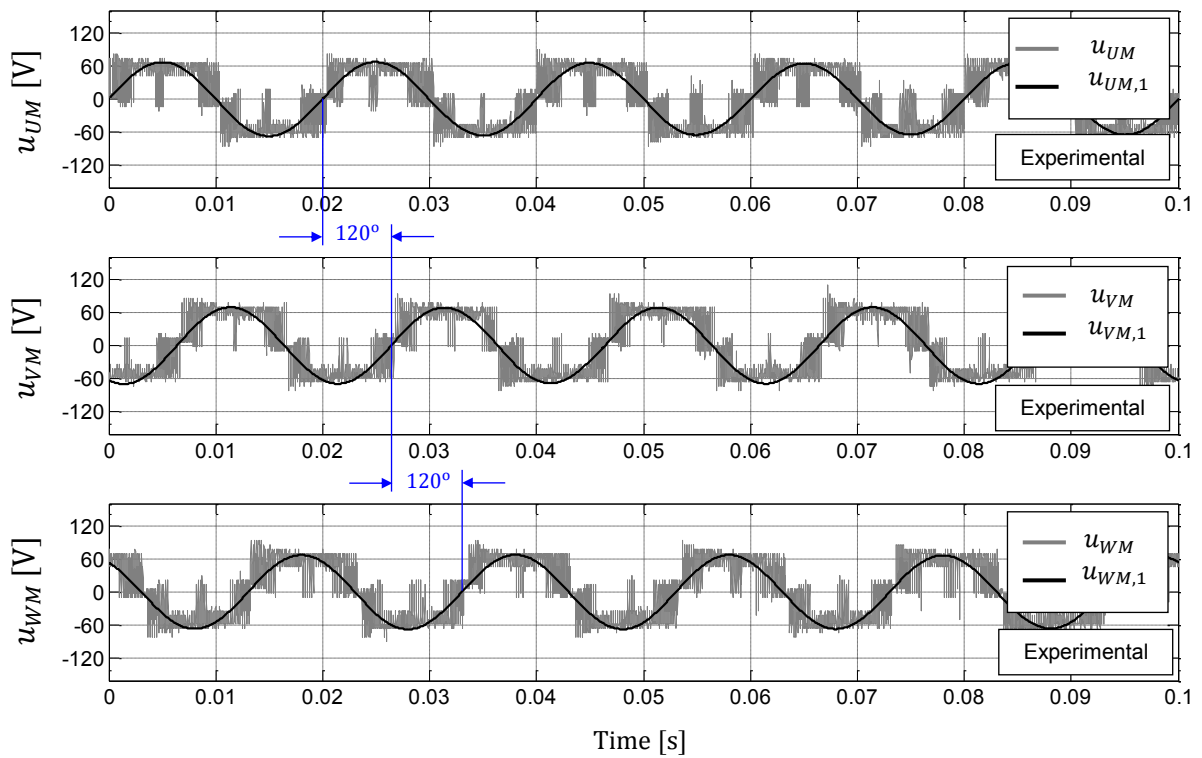


Figure 78 Inverter phase voltages and their fundamentals for mode 8

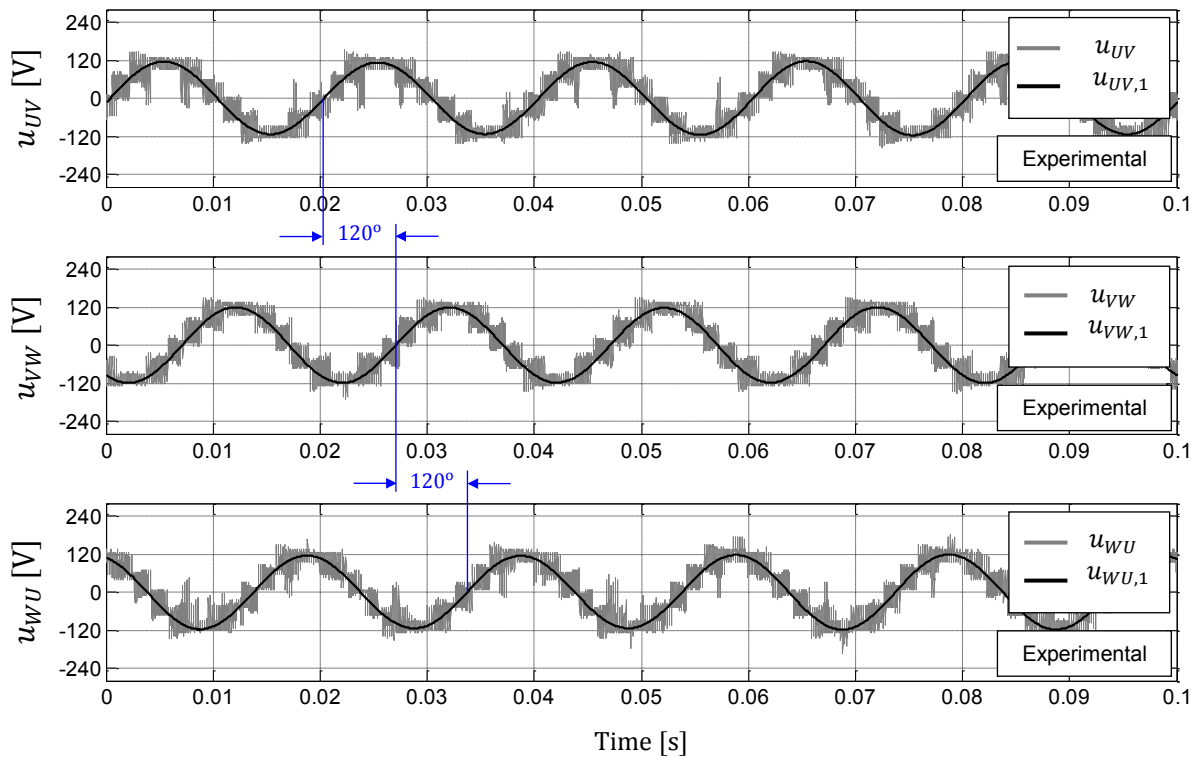


Figure 79 Inverter line to line voltages and their fundamentals for mode 8

4.4.7 Experimental results for rated PV-power and minimum WT-power

The behavior in the mode 7 of operation according to Table 3 is similar to the previous results (mode 8) with the difference that the unsymmetrical operation occurs due to the reduction in the power produced by the WT generation of the lower layer cells $U2, V2$ and $W2$ from $315W$ to $120W$. The reference voltages $u'_{ref U}, u'_{ref V}$ and $u'_{ref W}$ after the *per-phase compensation* and the *min-max* of the zero sequence u_{zero} are shown in Figure 80. Like in the mode 8 of operation presented above, the *min-max* of the zero sequence is kept unchanged deactivating the *per-phase compensation* because there is no difference in power produced in the phases. Figure 81 shows the modification in the reference voltages of phase U due to the *per-cell compensation* in order to perform the redistribution of the power delivered by the upper and lower layer cells like in the previous result (mode 8). In all phases the *ON/OFF* times of the cell are modified according to the produced power due to the modification in the amplitude of the

reference voltage for each cell of the inverter. Thus, the WT generators of the lower layer HB cells keep working at their maximum power point. As shown in Figure 81 the reference voltage $u''_{ref U2}$ for the cell $U2$ has dropped to 0,3 approximately, because the wind speed has been reduced to 38% of its rated value. The same reduction is done for cell $V2$ and $W2$, while the reference voltage $u''_{ref U1}$ of the cell $U1$ has been increased to 0,8 approximately in order to compensate the drop in the voltage of the lower layer cells. The same increment is done for cell $V1$ and $W1$.

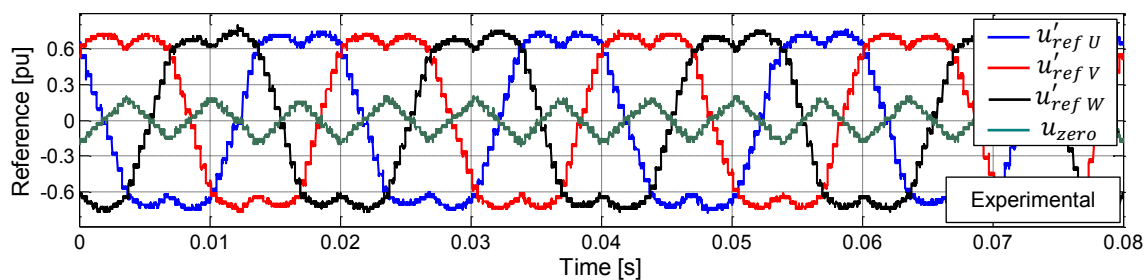


Figure 80 Reference voltages after *per-phase compensation* for mode 7

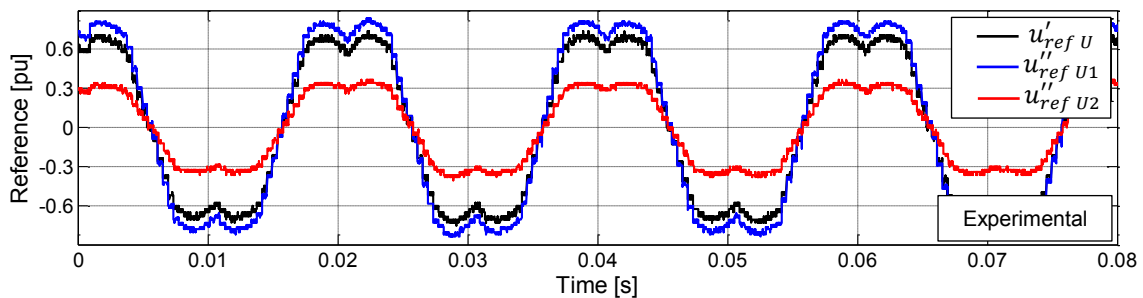


Figure 81 Reference voltage of phase U before and after *per-cell compensation* for mode 7

Figure 82 shows the inverter line currents injected to the grid. The currents are balanced and exhibit a RMS value of 9,5A while the total injected power is reduced to 1178W due to the reduction in the power production of the WT generators to their minimum values. Figure 83 shows the inverter phase voltages and Figure 84 shows the

inverter line to line voltages. The fundamental component voltages of the previous figures are balanced like in the results of the previous mode.

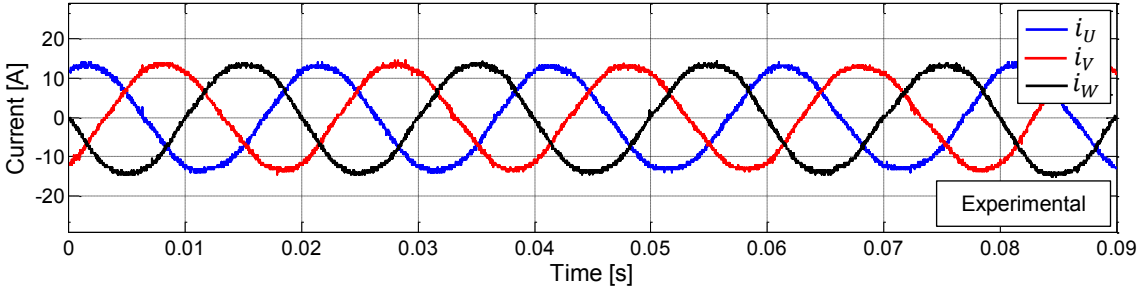


Figure 82 Inverter currents injected to the grid for mode 7

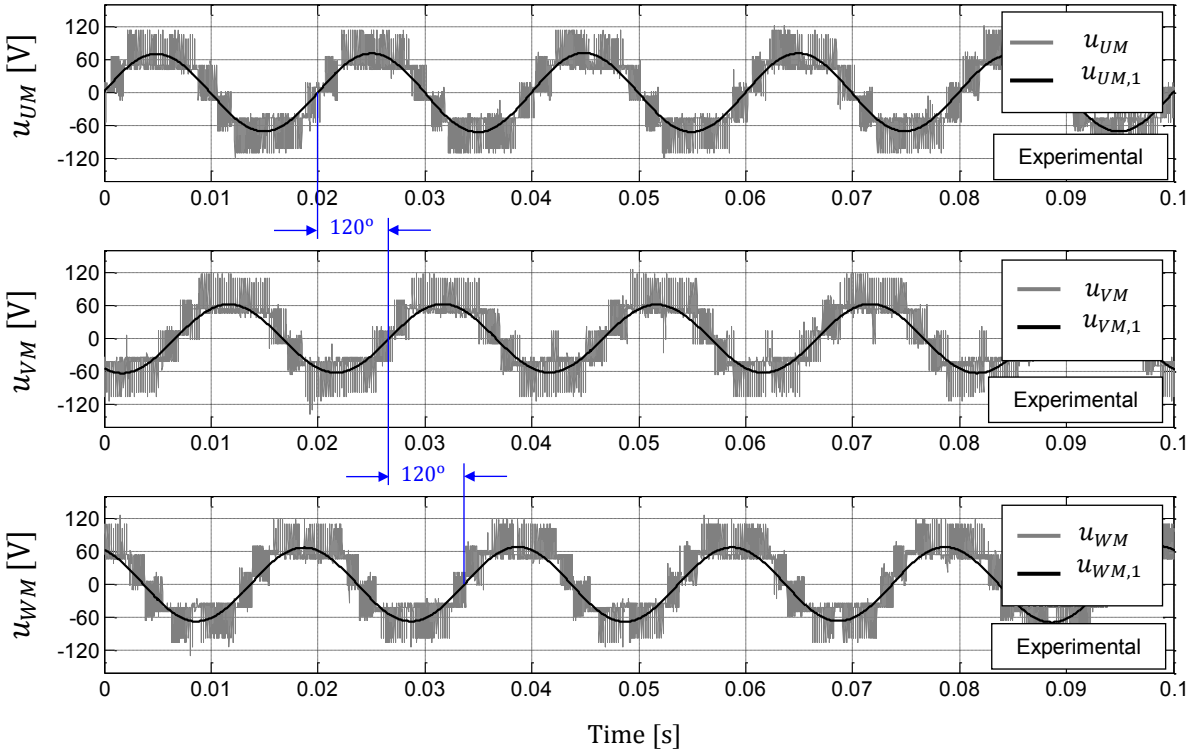


Figure 83 Inverter phase voltages and their fundamentals for mode 7

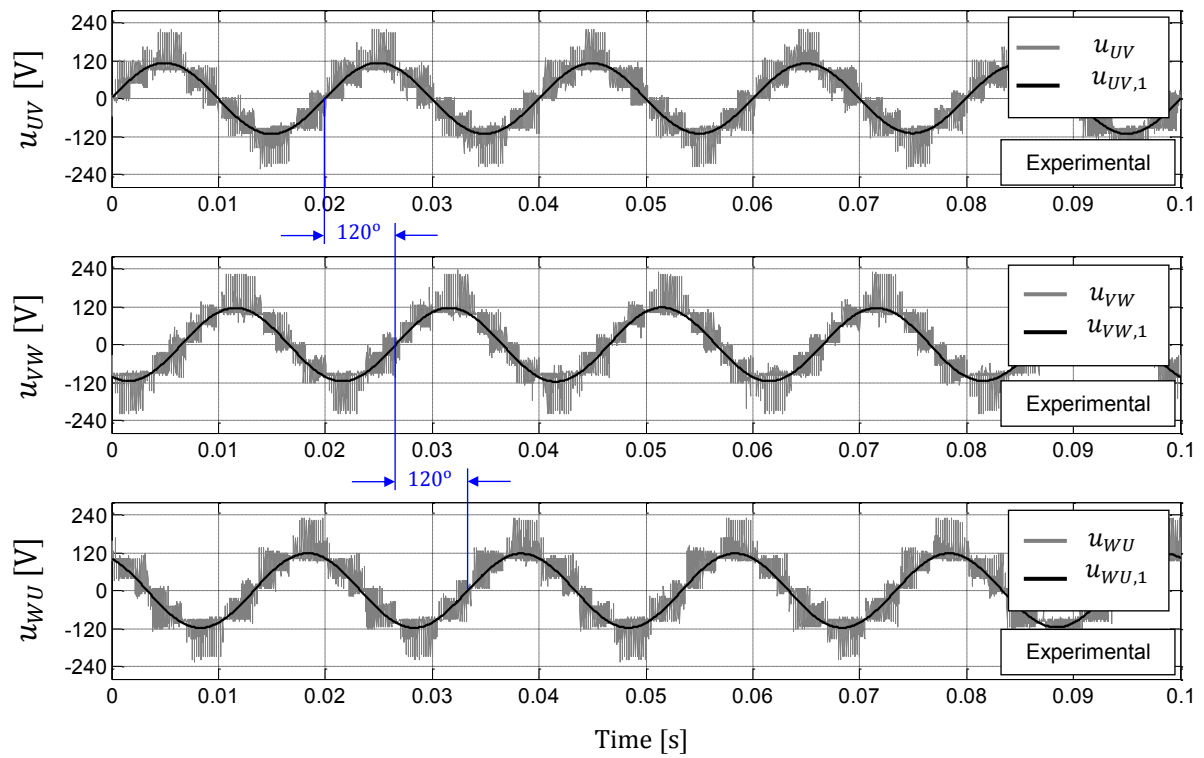


Figure 84 Inverter line to line voltages and their fundamentals for mode 7

5 Summary and Conclusions

The present work fulfills its main objective namely the study of the utilization of a multi-level cascaded H-bridge voltage source inverter as a suitable power electronics topology to perform the grid integration of hybrid energy sources. In particular, the connection of two different types of energy sources to the grid was examined, i.e. PV-panels as well as wind turbines with permanent magnet synchronous generators. In addition, the control and the operation of the whole hybrid system in the MPP-operation without using the additional DC-DC converters as in the conventional approaches was extensively analyzed by simulations and experiments.

The hybrid operation of PV cells and wind turbine system was initially comprehensively described for a single phase topology, and was then extended to the three phase one. The problem of the oversizing of the inverter was addressed and a proposal for facing this problem was presented as well.

The research work comprises the practical experiments by using a laboratory setup with a 5-level cascaded H-bridge voltage source inverter (5L-CHB-VSI), in which each H-bridge of the inverter was fed by either PV panels, which were emulated by using programmable DC supplier, or by wind turbines which were emulated using permanent magnet synchronous generators driven by an induction motor.

The control of the grid connection was performed by using a voltage oriented scheme in order to separately control the injection of active and reactive power to the grid. Furthermore, two types of feedforward compensation methods were used. The first one was performed by the injection of a zero-sequence signal to the reference signal of phase voltage in order to balance the power flow to the grid in case of unsymmetrical energy production among phases. The second was performed to control the amplitude of the reference voltage signal of each HB cell of the inverter individually in order to track the maximum power point of each connected energy source. The proposed control scheme including feedforward modulation index compensation was realized by using a single DSP.

The performance of the feedforward compensation methods used in the hybrid system was examined by simulation and experimentally for three different modes of operation, in which the availability of PV or WT power varies due to the different weather conditions.

The first mode was tested for the rated power production for all HB cells and then for unsymmetrical power generation among the different phases by reducing the power of one PV panel to 30% of the rated power and finally of the two PV generators in the same way.

The second mode was examined by reducing the generation of all PV panels to 30% of the rated power while the third mode was tested by reducing the generation of all WT generators to 38% of the rated power.

The simulation and the experimental results for the three operation modes show the flexible operation of the system with the individual MPPT operation for each H-bridge cell and without using DC-DC converters. The stable and balanced injection of the power to the grid is ensured even under unsymmetrical generation conditions. The cascaded H-bridge voltage source inverter is suitable topology for grid integration of the hybrid energy sources.

6 Appendix

6.1 Parameters of lab grid connection hybrid system

5L-CHB VSI	U_{DC}	200V
	C_{DC}	6 mF
	I_{rated}	20 A (rms)
	$f_{switching}$	5 kHz
Induction machine (VEM KPER 112M 6)	P_{rated}	2,2 kW
	U_{rated}	400 V
	I_{rated}	5,36 A (rms)
	n_{rated}	940 min ⁻¹
	p	3
	$\cos \varphi_{rated}$	0,8
PMSG (SEMENS 1FT5)	P_{rated}	5 kW
	U_{rated}	400 V
	n_{rated}	3000 min ⁻¹
	p	1
Grid connection filter	R_f	0,065 Ω
	L_f	7 mH
Programmable DC supply (EA-PS 8360-10 T)	P_{rated}	1 kW
	U_{rated}	0 – 360 V
	I_{rated}	0 – 10 A
ABB Inverter drive (ACS880-01-017A)	P_{rated}	7,5 kW
	U_{rated}	0 - 415 V
	I_{rated}	17 A
	Frequency	0 – 500 Hz

References

- [1] F. Z. Peng, W. Qian and D. Cao, "Recent advances in multilevel converter/inverter topologies and applications," Power Electronics Conference (IPEC), 2010 International, Sapporo, 2010, pp. 492-501.
- [2] Bernet, S.; "State of the Art and Developments of Medium Voltage Converters – An Overview," in Proceedings of the International Conference PELINCEC, Warsaw, Poland, Oct. 16-19, 2005.
- [3] S. Kouro, M. Malinowski, K. Gopakumar, J. Pou, L. G. Franquelo, BinWu, J. Rodriguez, M. Pérez, and J. I. Leon, "Recent Advances and Industrial Applications of Multilevel Converters ", IEEE Transactions on Industrial Electronics, VOL. 57, NO. 8, August 2010.
- [4] M. Malinowski, K. Gopakumar, J. Rodriguez and M. A. Pérez, " A Survey on Cascaded Multi-level Inverters ", IEEE Transactions on Industrial Electronics, VOL. 57, No. 7, July 2010.
- [5] L. G. Franquelo, J. Rodríguez, J. I. Leon, S. Kouro, R. Portillo and M.A.M. Prats, " The Age of Multilevel Converters Arrives ", IEEE Industrial Electronics Magazine June 2008.
- [6] J. Rodriguez, L. G. Franquelo, S. Kouro, J. I. Leo'n, R. C. Portillo, Ma A. M. Prats, and M. A. Pérez, " Multilevel Converters: An Enabling Technology for High-Power Applications ", Proceedings of the IEEE | VOL. 97, No. 11, November 2009.
- [7] P. Lezana, G. Ortiz, and J. Rodriguez, "Operation of regenerative cascade multicell converter under fault condition," in Control and Modeling for Power Electronics, 2008. COMPEL 2008. 11th Workshop on, aug. 2008, pp. 1 –6.
- [8] E. Villanueva, P. Correa, J. Rodriguez, and M. Pacas, "Control of a single-phase cascaded h-bridge multilevel inverter for grid-connected photovoltaic systems," Industrial Electronics, IEEE Transactions on, vol. 56, no. 11, pp. 4399–4406, Nov. 2009.
- [9] S. Kouro, B. Wu, A. Moya, E. Villanueva, P. Correa, and J. Rodriguez, "Control of a cascaded h-bridge multilevel converter for grid connection of photovoltaic systems," in Industrial Electronics, 2009. IECON '09. 35th Annual Conference of IEEE, nov. 2009, pp. 3976 –3982.
- [10] Wang ShuZheng; Zhao Jianfeng; Shi Chao, "Research on a three-phase cascaded inverter for grid-connected photovoltaic systems," Advanced Power System Automation and Protection (APAP), 2011 International Conference on , vol.1, no., pp.543,548, 16-20 Oct. 2011.
- [11] Townsend, C. D.; Summers, T.J.; Betz, R.E., "Control and modulation scheme for a Cascaded H-Bridge multi-level converter in large scale photovoltaic systems," Energy Conversion Congress and Exposition (ECCE), 2012 IEEE , vol., no., pp.3707,3714, 15-20 Sept. 2012.
- [12] Rivera, S.; Kouro, S.; Wu, B.; Leon, J.I.; Rodriguez, J.; Franquelo, L.G., "Cascaded H-bridge multilevel converter multistring topology for large scale photovoltaic systems," in Industrial Electronics (ISIE), 2011 IEEE International Symposium on , vol., no., pp.1837-1844, 27-30 June 2011
- [13] Morya, A.K.; Shukla, A., "Space vector modulated cascaded H-bridge multilevel converter for grid integration of large scale photovoltaic power plants," Power Engineering, Energy and Electrical Drives (POWERENG), 2013 Fourth International Conference on , vol., no., pp.181,186, 13-17 May 2013.
- [14] Rivera, S.; Bin Wu; Kouro, S.; Hong Wang; Donglai Zhang, "Cascaded H-bridge multilevel converter topology and three-phase balance control for large scale photovoltaic systems," Power Electronics for Distributed Generation Systems (PEDG), 2012 3rd IEEE International Symposium on , vol., no., pp.690,697, 25-28 June 2012.
- [15] Kouro, S.; Fuentes, C.; Perez, M.; Rodriguez, J., "Single DC-link cascaded H-bridge multilevel multistring photovoltaic energy conversion system with inherent balanced operation," IECON 2012 - 38th Annual Conference on IEEE Industrial Electronics Society , vol., no., pp.4998,5005, 25-28 Oct. 2012.

- [16] Wei Zhao; Hyuntae Choi; Konstantinou, G.; Ciobotaru, M.; Agelidis, V.G., "Cascaded H-bridge multilevel converter for large-scale PV grid-integration with isolated DC-DC stage," *Power Electronics for Distributed Generation Systems (PEDG)*, 2012 3rd IEEE International Symposium on , vol., no., pp.849,856, 25-28 June 2012.
- [17] Y. Yu, G. Konstantinou, B. Hredzak and V. G. Agelidis, "Optimal zero sequence injection in multilevel cascaded H-bridge converter under unbalanced photovoltaic power generation," *2014 International Power Electronics Conference (IPEC-Hiroshima 2014 - ECCE ASIA)*, Hiroshima, 2014, pp. 1458-1465.
- [18] Yifan Yu; Konstantinou, G.; Hredzak, B.; Agelidis, V.G., "Power Balance of Cascaded H-Bridge Multilevel Converters for Large-Scale Photovoltaic Integration," in *Power Electronics*, *IEEE Transactions on* , vol.31, no.1, pp.292-303, Jan. 2016
- [19] R. P. Aguilera; P. Acuna; Y. Yu; G. Konstantinou; C. D. Townsend; B. Wu; V. G. Agelidis, "Predictive Control of Cascaded H-Bridge Converters Under Unbalanced Power Generation," in *IEEE Transactions on Industrial Electronics* , vol.PP, no.99, 2016, pp.1-1
- [20] C. A. Rojas, S. Kouro, R. Ruiz, S. Rivera, B. Wu and X. Guo, "Multiobjective Predictive Control of a three-phase seven-level cascaded H-bridge converter for grid-connected photovoltaic systems," *2015 IEEE 24th International Symposium on Industrial Electronics (ISIE)*, Buzios, 2015, pp. 1121-1126.
- [21] O. A. Taha and M. Pacas, "Hardware implementation of balance control for three-phase grid connection 5-level Cascaded H-Bridge converter using DSP," *2014 IEEE 23rd International Symposium on Industrial Electronics (ISIE)*, Istanbul, 2014, pp. 1366-1371.
- [22] Liang Zhang; Xu Cai, "A Novel Multi-level Medium Voltage Converter Designed for Medium Voltage Wind Power Generation System," in *Power and Energy Engineering Conference (APPEEC)*, 2010 Asia-Pacific , vol., no., pp.1-4, 28-31 March 2010
- [23] Xibo Yuan; Jianyun Chai; Yongdong Li, "A Transformer-Less High-Power Converter for Large Permanent Magnet Wind Generator Systems," in *Sustainable Energy*, *IEEE Transactions on* , vol.3, no.3, pp.318-329, July 2012
- [24] Parker, M.A.; Ng, Chong; Ran, L., "Fault-Tolerant Control for a Modular Generator-Converter Scheme for Direct-Drive Wind Turbines," in *Industrial Electronics*, *IEEE Transactions on* , vol.58, no.1, pp.305-315, Jan. 2011
- [25] Parker, M.A.; Li Ran; Finney, S.J., "Distributed Control of a Fault-Tolerant Modular Multilevel Inverter for Direct-Drive Wind Turbine Grid Interfacing," in *Industrial Electronics*, *IEEE Transactions on* , vol.60, no.2, pp.509-522, Feb. 2013
- [26] Xibo Yuan, "Low voltage ride through control of a cascaded high power converter for direct-drive permanent magnet wind generators," in *IECON 2012 - 38th Annual Conference on IEEE Industrial Electronics Society* , vol., no., pp.3553-3559, 25-28 Oct. 2012
- [27] Ahmed, A.A.; Li Ran; Bumby, J., "Simulation and control of a hybrid PV-wind system," in *Power Electronics, Machines and Drives*, 2008. PEMD 2008. 4th IET Conference on , vol., no., pp.421-425, 2-4 April 2008
- [28] Sharma, R.; Sathans, "Survey on hybrid (Wind/Solar) renewable energy system and associated control issues," in *Power Electronics (IICPE)*, 2014 IEEE 6th India International Conference on , vol., no., pp.1-6, 8-10 Dec. 2014
- [29] Bouharchouche, A.; Berkouk, E.M.; Ghennam, T., "Control and energy management of a grid connected hybrid energy system PV-wind with battery energy storage for residential applications," in *Ecological Vehicles and Renewable Energies (EVER)*, 2013 8th International Conference and Exhibition on , vol., no., pp.1-11, 27-30 March 2013

- [30] Nair, N.R.; Ebenezer, M., "Operation and control of grid connected wind — PV hybrid system," in *Advances in Green Energy (ICAGE)*, 2014 International Conference on , vol., no., pp.197-203, 17-18 Dec. 2014
- [31] Rajan Singaravel, M.M.; Daniel, S.A., "MPPT With Single DC–DC Converter and Inverter for Grid-Connected Hybrid Wind-Driven PMSG–PV System," in *Industrial Electronics, IEEE Transactions on* , vol.62, no.8, pp.4849-4857, Aug. 2015
- [32] Gupta, P.; Tripathi, S.K., "Analysis of grid-tied hybrid wind PV generation system," in *Computational Intelligence on Power, Energy and Controls with their impact on Humanity (CIPECH)*, 2014 Innovative Applications of , vol., no., pp.447-451, 28-29 Nov. 2014
- [33] Wandhare, R.G.; Agarwal, V., "Novel Integration of a PV-Wind Energy System With Enhanced Efficiency," in *Power Electronics, IEEE Transactions on* , vol.30, no.7, pp.3638-3649, July 2015
- [34] M. H. Rashid, "Power Electronics Handbook: Devices, Circuits, and Application" Third edition, New York: Elsevier, 2011.
- [35] Bogdan M. Wilamowski, J.David Irwin, "Power Electronics and Motor Drives", New York: CRC Press, 2011.
- [36] D. S. Morales, "Maximum Power Point Tracking Algorithms for Photovoltaic Application", Aalto University: Ph.D. Dissertation, 2010.
- [37] Bin Wu, Yongqiang Lang, Navid Zargari, Samir Kouro, "Power conversion and control of wind energy Systems", Wiley-IEEE Press, August 2011.
- [38] A. Betz , "Wind-Energie und ihre Ausnutzung durch Windmühlen", Vandenhoeck und Ruprecht, Göttingen, 1926.
- [39] Kovacs, K.P., Raes, I. "Transiente Vorgänge in Wechselstrommaschinen," Verlag der Ungarischen Akademie der Wissenschaft, Bd. I, BdII, Budapest, 1959.
- [40] P. I. Correa Vasquez, Dissertation, "Fault Tolerant Operation of Series Connected H-Bridge Multilevel Inverters", University of Siegen, Germany 2006.
- [41] R. M. Caporal, Ph.D. Dissertation, "Encoderless predictive direct torque control of the synchronous reluctance machine at low and zero speed", University of Siegen, Germany 2007.
- [42] P. P. Palma, "Finite Set Model Predictive Control of the PMSM with Sine-Wave Filter", University of Siegen: Ph.D. Dissertation, 2015.
- [43] Marian P. Kazmierkowski, R. Krishnan, Frede Blaabjerg, "Control in Power Electronics: Selected Problems", Amsterdam: Academic Press, 2002.
- [44] Jae Hyeong Seo; Chang Ho Choi; Dong Seok Hyun; "A New Simplified Space Vector PWM Method for Three-Level Inverters", *Power Electronics, IEEE Transactions on* , vol.16, no.4, pp.545-550, Jul 2001.
- [45] Celanovic, N.; Boroyevich, D.; "A fast space-vector modulation algorithm for multilevel three-phase converters", *Industry Applications, IEEE Transactions on*, vol.37, no.2, pp.637-641, Mar/Apr 2001.
- [46] Sanmin Wei; Bin Wu; Fahai Li; Congwei Liu; "A general space vector PWM control algorithm for multilevel inverters", *Applied Power Electronics Conference and Exposition, 2003. APEC '03. Eighteenth Annual IEEE*, vol.1, no., pp. 562- 568 vol.1, 9-13 Feb. 2003.
- [47] McGrath, B.P.; Holmes, D.G.; Lipo, T.; "Optimized space vector switching sequences for multilevel inverters", *Power Electronics, IEEE Transactions on* , vol.18, no.6, pp. 1293- 1301, Nov. 2003.
- [48] Gupta, A.K.; Khambadkone, A.M.; , "A General Space Vector PWM Algorithm for Multilevel Inverters Including Operation in Over modulation Range", *Power Electronics, IEEE Transactions on* , vol.22, no.2, pp.517-526, March 2007.

- [49] Aneesh, M.A.S.; Gopinath, A.; Baiju, M.R.; "A Simple Space Vector PWM Generation Scheme for Any General n -Level Inverter", *Industrial Electronics, IEEE Transactions on* , vol.56, no.5, pp.1649-1656, May 2009.
- [50] T. M. Phan, Ph.D. Dissertation, "Protection of the Switches in a Three-Level Inverter by Using Modified Switching Schemes for the Redistribution of Losses", University of Siegen Germany 2016.
- [51] H. Rahbarimagham, E. Maali Amiri, B. Vahidi, G. Babamalek Gharehpetian, M. Abedi, "Superior decoupled control of active and reactive power for three-phase voltage source converters," *Turkish Journal of Electrical Engineering and Computer Sciences*, doi:10.3906/elk-1303-118.
- [52] Mariusz Malinowski, "Sensorless Control Strategies for Three - Phase PWM Rectifiers Dissertation," Warsaw University of Technology, Warsaw Poland, 2001
- [53] Nicastrì, A.; Nagliero, A., "Comparison and evaluation of the PLL techniques for the design of the grid-connected inverter systems," in *Industrial Electronics (ISIE), 2010 IEEE International Symposium on*, vol., no., pp.3865-3870, 4-7 July 2010
- [54] R. E. Best, "Phase-Locked Loops: Design, Simulation, and Applications", Sixth Edition, New York: McGraw-Hill Education, 2007.
- [55] Emura, T.; Lei Wang, "A high-resolution interpolator for incremental encoders based on the quadrature PLL method," in *Industrial Electronics, IEEE Transactions on* , vol.47, no.1, pp.84-90, Feb 2000
- [56] Ferreira, R.J.; Araujo, R.E.; Pecas Lopes, J.A., "A comparative analysis and implementation of various PLL techniques applied to single-phase grids," in *Energetics (IYCE), Proceedings of the 2011 3rd International Youth Conference on* , vol., no., pp.1-8, 7-9 July 2011
- [57] Karimi, H.; Karimi-Ghartemani, M.; Iravani, M.R., "Estimation of frequency and its rate of change for applications in power systems," in *Power Delivery, IEEE Transactions on* , vol.19, no.2, pp.472-480, April 2004
- [58] Jamarani, M.; Abrishamifar, A.; Pichan, M.; Fazeli, M., "Evaluation of different positive sequence detection structures applied to grid-connected systems," in *Power Electronics, Drive Systems and Technologies Conference (PEDSTC), 2014 5th* , vol., no., pp.126-130, 5-6 Feb. 2014
- [59] Gaolin Wang; Zhuomin Li; Guoqiang Zhang; Yong Yu; Dianguo Xu, "Quadrature PLL-Based High-Order Sliding-Mode Observer for IPMSM Sensorless Control With Online MTPA Control Strategy," in *Energy Conversion, IEEE Transactions on* , vol.28, no.1, pp.214-224, March 2013
- [60] Nagliero, A.; Mastromauro, R.A.; Liserre, M.; Dell'Aquila, A., "Synchronization techniques for grid connected wind turbines," in *Industrial Electronics, 2009. IECON '09. 35th Annual Conference of IEEE* , vol., no., pp.4606-4613, 3-5 Nov. 2009
- [61] Ali, A.N.A.; Saied, M.H.; Mostafa, M.Z.; Abdel-Moneim, T.M., "A survey of maximum PPT techniques of PV systems," in *Energytech, 2012 IEEE* , vol., no., pp.1-17, 29-31 May 2012
- [62] Durgadevi, A.; Arulselvi, S.; Natarajan, S.P., "Study and implementation of Maximum Power Point Tracking (MPPT) algorithm for Photovoltaic systems," in *Electrical Energy Systems (ICEES), 2011 1st International Conference on*, vol., no., pp.240-245, 3-5 Jan. 2011
- [63] Mei Shan Ngan; Chee Wei Tan, "A study of maximum power point tracking algorithms for stand-alone Photovoltaic Systems," in *Applied Power Electronics Colloquium (IAPEC), 2011 IEEE* , vol., no., pp.22-27, 18-19 April 2011
- [64] Femia, N.; Petrone, G.; Spagnuolo, G.; Vitelli, M., "Optimization of perturb and observe maximum power point tracking method," in *Power Electronics, IEEE Transactions on* , vol.20, no.4, pp.963-973, July 2005

- [65] Beriber, D.; Talha, A., "MPPT techniques for PV systems," in Power Engineering, Energy and Electrical Drives (POWERENG), 2013 Fourth International Conference on , vol., no., pp.1437-1442, 13-17 May 2013
- [66] D. P. Hohm and M. E. Ropp , "Comparative Study of Maximum Power Point Tracking Algorithms," Progress in Photovoltaics: Research and Applications, Res. Appl. 2003; 11:47–62 (DOI: 10.1002/pip.459)
- [67] El-Sebaai, A.M.; Hamad, M.S.; Helal, A.A., "A sensorless MPPT technique for a grid-connected PMSG wind turbine system," in Renewable Power Generation Conference (RPG 2013), 2nd IET , vol., no., pp.1-6, 9-11 Sept. 2013
- [68] Shirazi, M.; Viki, A.H.; Babayi, O., "A comparative study of maximum power extraction strategies in PMSG wind turbine system," in Electrical Power & Energy Conference (EPEC), 2009 IEEE , vol., no., pp.1-6, 22-23 Oct. 2009
- [69] Bhandare, A.M.; Bandekar, P.J.; Mane, S.S., "Wind energy maximum power extraction algorithms: A review," in Energy Efficient Technologies for Sustainability (ICEETS), 2013 International Conference on , vol., no., pp.495-500, 10-12 April 2013
- [70] Quincy Wang; Liuchen Chang, "An intelligent maximum power extraction algorithm for inverter-based variable speed wind turbine systems," in Power Electronics, IEEE Transactions on , vol.19, no.5, pp.1242-1249, Sept. 2004
- [71] Krishnat R. Dubal, Dattatray S. Chavan , "Hill climbs searching method for wind generator of maximum power point tracking system," International Journal of Advanced Engineering Research and Technology (IJAERT) Volume 2 Issue 7, October 2014, ISSN No.: 2348 – 8190.